COMPUTATIONAL STUDY OF POINT DEFECTS IN METAL-ORGANIC FRAMEWORKS

A Dissertation
Presented to
The Academic Faculty

by

Chu Han

In Partial Fulfillment
of the Requirements for the Degree
Doctor of Philosophy in the
School of Chemistry and Biochemistry

Georgia Institute of Technology
December 2018

COMPUTATIONAL STUDY OF POINT DEFECTS IN

METAL-ORGANIC FRAMEWORKS

Approved by:

Dr. David S. Sholl, Advisor

School of Chemical and Biomolecular Engineering

Georgia Institute of Technology

Dr. Angus P. Wilkinson

School of Chemistry and Biochemistry

Georgia Institute of Technology

Dr. Thomas M. Orlando

School of Chemistry and Biochemistry

Georgia Institute of Technology

Dr. Meilin Liu

School of Materials Science and Engineering

Georgia Institute of Technology

Dr. C. David Sherrill

School of Chemistry and Biochemistry

Georgia Institute of Technology

Approved: August 30th, 2018

To My Parents

ACKNOWLEDGEMENTS

First and foremost, I would express my sincere gratitude to my advisor Prof. David Sholl, who guides and supports me during my Ph.D. study. The first time I knew Prof. Sholl was through his book, *Density Functional Theory: A Practical Introduction*, which is a wonderful introduction book for such an advanced theory. I am fortunate to be one of his students. In addition to the knowledge of science, I have also learnt useful skills from him such as how to present my work, how to communicate with others, how to plan for my career path, and so on, which will benefit me throughout my life. Prof. Sholl is one of the most important teachers throughout my education.

I sincerely thank my committee members: Prof. Thomas Orlando, Prof. Angus Wilkinson, Prof. David Sherrill, and Prof. Meilin Liu, who have given me many helpful suggestions on my thesis work.

Thanks to the Department of Energy and everyone at the Energy Frontier Research Centers for funding my Ph.D. research. In particular, I would like to thank Prof. JR Schmidt, who gave me many helpful suggestions on our collaborated EFRC projects.

My work has benefited greatly from my collaborators, and some of the results presented in this thesis are derived from their work. All of the experimental results in Chapter 3 are from experiments by Dr. Simon Pang and Dr. William Mounfield. The calculations for Figure 3.3 and Figure A.4 were performed by Dr. Chenyang Zhang. The calculations for Figure 4.5, Table 4.1, and Table 4.3 were performed by Dr. Nina Tyminska and Dr. Chenyang Zhang. Dr. Ross Verploegh patiently taught me how to perform MD simulations using LAMMPS and helped to perform calculations for Figure C.2. I would

like to also thank Prof. Angelo Bongiorno, who introduced me the density functional theory and taught me how to perform DFT calculations.

Many thanks to all the members in the Sholl group. I especially want to extend my thanks to Dr. Hanjun Fang, Dr. Salah Boulfelfel, Rebecca Han, Dr. Joshua Howe, Anny Liu, and Jonathan Haffen-Haydak. I enjoyed discussing research with them and our conversations made my studies more efficient.

I deeply thank my friends in Georgia Tech for their help, support, and happy time we spent together: Yu Cao, Xiaoling Zang, Ying Sha, Zhishuai Geng, Shan Zhou, Di Chen, Si Zhou, and Xi Lu.

Finally, I am deeply grateful for my mom and dad, Ling Tao and Taixiang Han, who are supporting me all the time. Although I do not follow their suggestions sometimes, my parents always support me as long as I made my decisions. They say this is my life, I should learn from my own success as well as failures. This thesis is dedicated to them.

Chu Han, Atlanta, August 2018

TABLE OF CONTENTS

LIST OF TABLES

LIST OF FIGURES

SUMMARY

Metal-Organic Frameworks (MOFs) are a class of porous materials composed of metal clusters connecting by organic ligands and forming in one-, two-, or three-dimensional structures. The tunable pore sizes, ultrahigh surface areas and pore volumes, together with the versatile functionalization of ligands make MOFs ideal candidates for applications including gas storage and separations, catalysis, and drug delivery. However, many MOFs have been found to degrade upon exposure to humid conditions or humid acid-gases. High chemical stability is required for MOFs to be practical applications as their working environments may be humid or acidic. Thus, it is of great importance to understand the degradation mechanisms of MOFs under related conditions. In my thesis work, I adopt ZIFs, an important subclass of MOFs, as prototypical models to investigate the potential degradation reactions occurring by the attack of water and acid gases. I utilized density functional theory methods and developed atomistic models to explore the energetic properties of point defects resulted by these reactions.

Diffusion-based gas separations in MOFs has promising applications for chemical mixture separations. Extensive experimental and computational investigations have been conducted for the screening of MOFs for separating specific components with high selectivity. However, the impact of defective structures on molecular diffusion has not been widely considered. This motivated me to perform molecular dynamics simulations using transition state theory method to explore the change in hopping rates of adsorbates caused by defective structures in MOFs. In general, the point defects I have examined in ZIF-8 increase the local hopping rate for molecular diffusion, suggesting that low concentrations of these defects will not dominate long range molecular diffusion in ZIF-8.

CHAPTER 1
INTRODUCTION

1.1 Metal-Organic Frameworks and Their Applications

Metal-Organic Frameworks (MOFs) are nanoporous crystalline polymers composed of metal cluster centers connected by organic ligands, forming in one-, two-, or three-dimensional topologies. Reported for the first time in 1995[1] and synthesized in 1999,[2] MOFs nowadays hold great promise in a variety of technological applications. Compared with conventional porous materials such as activated carbon and zeolites, MOFs exhibit ultrahigh porosity, versatile structures achieved by an enormous number of metal cluster centers and organic ligands combinations, and large internal surface areas.[3] In particular, MOFs are promising substitutes for current energy-intensive chemical mixture separation processes such as distillation.[4]

Among all the possible applications of MOFs, their potential use for gas storage has received intense interests. Take the storage of hydrogen as an example, hydrogen has the potential advantages as a fuel, however the storage of hydrogen is a challenge currently as the necessity to store liquid hydrogen or pressurized hydrogen has the risk of explosion.[5] Therefore, searching for MOFs with high H_2 capacity or the strategies to increase H_2 capacity in existing MOFs is of great interest. There are two main strategies to improve gas capacity in MOFs: one is to enlarge MOF surface area and pore volume, as gas storage capacity mainly depends on these quantities. The methods to increase surface area or pore volume include but are not limited to using elongated ligands,[6-7] catenation,[8] and mixing different ligands in the same MOF structure.[6,9] The other strategy is to enhance the heat of

adsorption for target adsorbates in MOFs. This can be achieved by generating coordinately unsaturated "open" metal sites that appear in some MOFs after the removal of the coordinating solvent molecules by thermal activation,[10] or post-synthetically modifying organic ligands by adding functional groups such as $–NH_2$ that can strongly interact with H_2.[11]

Gas separation, another application of MOFs that has attracted attention from academia in the past decade, can include adsorptive separations and membrane separations.[12] Adsorptive separations are based on the differences in adsorption/desorption behavior of distinct components in a gas mixture, while membrane separations take advantage of the differences in the diffusion mechanisms of mixed adsorbates. The tunable structures and pore sizes and the structural flexibility of some MOFs make them ideal candidates for membranes. For example, a high selectivity for H_2 was observed in HKUST-1 membranes [13] and ZIF-8 thin films.[14] In addition to the potential applications on gas storage and separations, MOFs have also shown promising usage in other areas including supercapacitors,[15-16] catalysts,[17] and drug capsules.[18]

1.2 Zeolitic-Imidazolate Frameworks: A Subclass of Metal-Organic Frameworks

Zeolitic-Imidazolate Frameworks (ZIFs), composed of tetrahedrally coordinated zinc or cobalt cations and bridging imidazolate (Im) ligands, forming in topologically similar crystal structures with zeolites due to the similarity of the Metal-Im-Metal bond angle to the Si-O-Si angle in conventional silicon-based zeolites, are an important subclass of MOFs. In 2006, Yaghi *et al.* pioneered the synthesis of twelve ZIF crystals, ZIF-1 to -12.[19] These ZIFs exhibited unusual thermal and chemical stability, for example, ZIF-8 and

-11 retained their powder-XRD (PXRD) patterns when heated and held at a temperature of 500 and 300 ^{o}C, respectively, and also retained their PXRD patterns after 7 days of exposure to boiling organic solvent, water, and basic solution. This stability has been matched by only a few MOFs with relatively dense structures.[19] Extensive studies about ZIFs have emerged in the past decade, resulting in development in synthesis techniques and their applications.[20] The synthesis of ZIFs was initially through solvothermal methods with organic solvents as the reaction medium,[19,21-23] but soon after hydrothermal synthesis was used to replace the expensive and flammable organic solvents.[24-26] Some ZIFs have also been successfully produced through a solvent-free method.[27-28] The synthesized ZIF crystals also evolved from powder in the early research stage to films/membranes now with the development of synthesis strategies.[20] Currently, ZIFs are widely investigated for their applications for gas separations and they exhibit promising performance in, for example, H_2/N_2,[29-32] H_2/CO_2,[29,31-32] H_2/CH_4,[29-32] H_2/Ar,[30-31] H_2/O_2,[30-31] and H_2/C_3H_8[32-33] separations.

In my thesis, I focused on ZIF-8 and used this ZIF as a prototypical model for the investigation of MOF stability and diffusion properties of adsorbates. ZIF-8, which is one of the most widely studied ZIFs both experimentally and computationally, is composed of Zn^{2+} cations and hydrophobic 2-methylimidazolate ligands, forming in the *sod* topology, with a pore limiting diameter of 3.4 Å.[19] Recently, the flexibility of ZIF-8 has been found to be important for molecular diffusion in this material as well as its performance of the diffusion-based gas separations.[34]

1.3 Chemical Stability of Metal-Organic Frameworks

Stability is a crucial factor that limits the practical use of MOFs. Although exhibiting promising industrial applications, MOFs still have drawbacks, one of which is their relatively lower chemical stability compared to other porous materials such as zeolites. Burtch et al. cataloged the water stability of MOFs, and their report pointed out that many well-known MOFs exhibiting promising applications were unstable in water.[35] Our and other's work also found ZIF-8, a hydrophobic ZIF, can degrade upon exposure to acid gases.[36-38] To make use of MOFs in practical applications, it is important for us to understand their degradation mechanisms, based on which we can improve their stability. This is one of the main motivations of this thesis. In this thesis, I utilized computational methods to investigate the degradation mechanisms of MOFs under acidic conditions.

As degradation is inevitable in MOFs and defects are ubiquitous in materials, at the same time of investigating how to minimize degradation, another direction of my study is to know how to make use of the defects. Defects have been found to play a positive role in several MOFs such as UiO-66, in which linker vacancies result in positive effects on gas adsorption.[39] In this thesis, I investigated the self-diffusion of several types of adsorbates in defective MOF structures, which were constructed based on the defects generated by our proposed degradation reactions. The comparison of the hopping rates of adsorbates in pristine MOFs with that in defective ones may provide insights into the influence of these defects on molecular diffusivity, which is an important quantity for evaluating the performance of MOFs in gas separations.

The chemical stability and degradation of MOFs opens the following questions:

(1) What reactions cause the degradation in MOFs? What are the product of the reactions, *i.e.*, defects?

(2) What factors influence the extent of degradation?

(3) How do these defects impact functions of MOF materials?

My thesis will be organized based on the above questions.

1.4 Thesis Summary

The objective of my work is to use computational methods to understand the degradation mechanisms of MOFs and investigate how the degraded structures, *i.e.*, defects, affect the adsorbate diffusion in these materials. The computational methods I used are mainly based on density functional theory and molecular dynamics simulations, which will be briefly introduced in Chapter 2. Chapter 3 focuses on the hypothetical point defects in ZIFs based on analogies to zeolites. The point defects are the starting point for the investigation of the degradation process of MOFs. A comprehensive computational study, which examines the stability of bulk structures and external surfaces of prototypical ZIFs as well as their polymorphs in humid acidic environments, is introduced in Chapter 4. Chapter 5 reports a molecular dynamics study about diffusion of hydrocarbons, acid gases, and water in defective ZIF-8 to discuss the potential impact of our proposed point defects on adsorbate diffusion. Finally, I will summarize my thesis work and propose possible future directions and development of my work. My thesis work on MOFs contributes to the MOF research area by providing an atomistic level understanding of the degradation mechanism for these materials, which will be helpful in the future development and improvement for these materials.

1.5 References

(1) Yaghi, O. M.; Li, G. M.; Li, H. L., Selective Binding and Removal of Guests in a Microporous Metal-Organic Framework. *Nature* **1995,** *378* (6558), 703-706.

(2) Li, H.; Eddaoudi, M.; O'Keeffe, M.; Yaghi, O. M., Design and synthesis of an exceptionally stable and highly porous metal-organic framework. *Nature* **1999,** *402* (6759), 276-279.

(3) Zhou, H. C.; Long, J. R.; Yaghi, O. M., Introduction to Metal-Organic Frameworks. *Chem. Rev.* **2012,** *112* (2), 673-674.

(4) Sholl, D. S.; Lively, R. P., Seven chemical separations to change the world. *Nature* **2016,** *532* (7600), 435-437.

(5) Suh, M. P.; Park, H. J.; Prasad, T. K.; Lim, D. W., Hydrogen Storage in Metal-Organic Frameworks. *Chem. Rev.* **2012,** *112* (2), 782-835.

(6) Furukawa, H.; Ko, N.; Go, Y. B.; Aratani, N.; Choi, S. B.; Choi, E.; Yazaydin, A. O.; Snurr, R. Q.; O'Keeffe, M.; Kim, J.; Yaghi, O. M., Ultrahigh Porosity in Metal-Organic Frameworks. *Science* **2010,** *329* (5990), 424-428.

(7) Yuan, D. Q.; Zhao, D.; Sun, D. F.; Zhou, H. C., An Isoreticular Series of Metal-Organic Frameworks with Dendritic Hexacarboxylate Ligands and Exceptionally High Gas-Uptake Capacity. *Angew. Chem., Int. Ed.* **2010,** *49* (31), 5357-5361.

(8) Ma, S. Q.; Eckert, J.; Forster, P. M.; Yoon, J. W.; Hwang, Y. K.; Chang, J. S.; Collier, C. D.; Parise, J. B.; Zhou, H. C., Further Investigation of the Effect of Framework Catenation on Hydrogen Uptake in Metal-Organic Frameworks. *J. Am. Chem. Soc.* **2008,** *130* (47), 15896-15902.

(9) Koh, K.; Wong-Foy, A. G.; Matzger, A. J., Coordination Copolymerization Mediated by $Zn_4O(CO_2R)_6$ Metal Clusters: a Balancing Act between Statistics and Geometry. *J. Am. Chem. Soc.* **2010,** *132* (42), 15005-15010.

(10) Chen, B. L.; Ockwig, N. W.; Millward, A. R.; Contreras, D. S.; Yaghi, O. M., High H_2 adsorption in a microporous metal-organic framework with open metal sites. *Angew. Chem., Int. Ed.* **2005,** *44* (30), 4745-4749.

(11) Wang, Z. Q.; Tanabe, K. K.; Cohen, S. M., Tuning Hydrogen Sorption Properties of Metal-Organic Frameworks by Postsynthetic Covalent Modification. *Chem. Eur. J.* **2010,** *16* (1), 212-217.

(12) Li, J. R.; Sculley, J.; Zhou, H. C., Metal-Organic Frameworks for Separations. *Chem. Rev.* **2012,** *112* (2), 869-932.

(13) Guo, H. L.; Zhu, G. S.; Hewitt, I. J.; Qiu, S. L., "Twin Copper Source" Growth of Metal-Organic Framework Membrane: $Cu_3(BTC)_2$ with High Permeability and Selectivity for Recycling H-2. *J. Am. Chem. Soc.* **2009,** *131* (5), 1646-1647.

(14) McCarthy, M. C.; Varela-Guerrero, V.; Barnett, G. V.; Jeong, H. K., Synthesis of Zeolitic Imidazolate Framework Films and Membranes with Controlled Microstructures. *Langmuir* **2010,** *26* (18), 14636-14641.

(15) Sheberla, D.; Bachman, J. C.; Elias, J. S.; Sun, C. J.; Shao-Horn, Y.; Dinca, M., Conductive MOF electrodes for stable supercapacitors with high areal capacitance. *Nat. Mater.* **2017,** *16* (2), 220-224.

(16) Diaz, R.; Orcajo, M. G.; Botas, J. A.; Calleja, G.; Palma, J., Co8-MOF-5 as electrode for supercapacitors. *Mater. Lett.* **2012,** *68*, 126-128.

(17) Harding, J. L.; Metz, J. M.; Reynolds, M. M., A Tunable, Stable, and Bioactive MOF Catalyst for Generating a Localized Therapeutic from Endogenous Sources. *Adv. Funct. Mater.* **2014,** *24* (47), 7503-7509.

(18) Orellana-Tavra, C.; Baxter, E. F.; Tian, T.; Bennett, T. D.; Slater, N. K. H.; Cheetham, A. K.; Fairen-Jimenez, D., Amorphous metal-organic frameworks for drug delivery. *Chem. Commun.* **2015,** *51* (73), 13878-13881.

(19) Park, K. S.; Ni, Z.; Cote, A. P.; Choi, J. Y.; Huang, R. D.; Uribe-Romo, F. J.; Chae, H. K.; O'Keeffe, M.; Yaghi, O. M., Exceptional chemical and thermal stability of zeolitic imidazolate frameworks. *Proc. Natl. Acad. Sci. U. S. A.* **2006,** *103* (27), 10186-10191.

(20) Chen, B. L.; Yang, Z. X.; Zhu, Y. Q.; Xia, Y. D., Zeolitic imidazolate framework materials: recent progress in synthesis and applications. *J. Mater. Chem. A* **2014,** *2* (40), 16811-16831.

(21) Banerjee, R.; Phan, A.; Wang, B.; Knobler, C.; Furukawa, H.; O'Keeffe, M.; Yaghi, O. M., High-throughput synthesis of zeolitic imidazolate frameworks and application to CO_2 capture. *Science* **2008,** *319* (5865), 939-943.

(22) Banerjee, R.; Furukawa, H.; Britt, D.; Knobler, C.; O'Keeffe, M.; Yaghi, O. M., Control of Pore Size and Functionality in Isoreticular Zeolitic Imidazolate Frameworks and their Carbon Dioxide Selective Capture Properties. *J. Am. Chem. Soc.* **2009,** *131* (11), 3875-3877.

(23) Huang, X. C.; Lin, Y. Y.; Zhang, J. P.; Chen, X. M., Ligand-directed strategy for zeolite-type metal-organic frameworks: Zinc(II) imidazolates with unusual zeolitic topologies. *Angew. Chem., Int. Ed.* **2006,** *45* (10), 1557-1559.

(24) Pan, Y. C.; Liu, Y. Y.; Zeng, G. F.; Zhao, L.; Lai, Z. P., Rapid synthesis of zeolitic imidazolate framework-8 (ZIF-8) nanocrystals in an aqueous system. *Chem. Commun.* **2011,** *47* (7), 2071-2073.

(25) Kida, K.; Okita, M.; Fujita, K.; Tanaka, S.; Miyake, Y., Formation of high crystalline ZIF-8 in an aqueous solution. *Crystengcomm* **2013,** *15* (9), 1794-1801.

(26) Chen, B. L.; Bai, F. H.; Zhu, Y. Q.; Xia, Y. D., A cost-effective method for the synthesis of zeolitic imidazolate framework-8 materials from stoichiometric precursors via aqueous ammonia modulation at room temperature. *Microporous Mesoporous Mater.* **2014,** *193*, 7-14.

(27) Lin, J. B.; Lin, R. B.; Cheng, X. N.; Zhang, J. P.; Chen, X. M., Solvent/additive-free synthesis of porous/zeolitic metal azolate frameworks from metal oxide/hydroxide. *Chem. Commun.* **2011,** *47* (32), 9185-9187.

(28) Lanchas, M.; Vallejo-Sanchez, D.; Beobide, G.; Castillo, O.; Aguayo, A. T.; Luque, A.; Roman, P., A direct reaction approach for the synthesis of zeolitic imidazolate frameworks: template and temperature mediated control on network topology and crystal size. *Chem. Commun.* **2012,** *48* (79), 9930-9932.

(29) Li, Y. S.; Liang, F. Y.; Bux, H. G.; Yang, W. S.; Caro, J., Zeolitic imidazolate framework ZIF-7 based molecular sieve membrane for hydrogen separation. *J. Membr. Sci.* **2010,** *354* (1-2), 48-54.

(30) Ge, L.; Zhou, W.; Du, A. J.; Zhu, Z. H., Porous Polyethersulfone-Supported Zeolitic Imidazolate Framework Membranes for Hydrogen Separation. *J. Phys. Chem. C* **2012,** *116* (24), 13264-13270.

(31) Ge, L.; Du, A. J.; Hou, M.; Rudolph, V.; Zhu, Z. H., Enhanced hydrogen separation by vertically-aligned carbon nanotube membranes with zeolite imidazolate frameworks as a selective layer. *RSC Adv.* **2012,** *2* (31), 11793-11800.

(32) Huang, A. S.; Chen, Y. F.; Wang, N. Y.; Hu, Z. Q.; Jiang, J. W.; Caro, J., A highly permeable and selective zeolitic imidazolate framework ZIF-95 membrane for H_2/CO_2 separation. *Chem. Commun.* **2012,** *48* (89), 10981-10983.

(33) Bux, H.; Feldhoff, A.; Cravillon, J.; Wiebcke, M.; Li, Y. S.; Caro, J., Oriented Zeolitic Imidazolate Framework-8 Membrane with Sharp H_2/C_3H_8 Molecular Sieve Separation. *Chem. Mater.* **2011,** *23* (8), 2262-2269.

(34) Fairen-Jimenez, D.; Moggach, S. A.; Wharmby, M. T.; Wright, P. A.; Parsons, S.; Duren, T., Opening the Gate: Framework Flexibility in ZIF-8 Explored by Experiments and Simulations. *J. Am. Chem. Soc.* **2011,** *133* (23), 8900-8902.

(35) Burtch, N. C.; Jasuja, H.; Walton, K. S., Water Stability and Adsorption in Metal-Organic Frameworks. *Chem. Rev.* **2014,** *114* (20), 10575-10612.

(36) Pang, S. H.; Han, C.; Sholl, D. S.; Jones, C. W.; Lively, R. P., Facet-Specific Stability of ZIF-8 in the Presence of Acid Gases Dissolved in Aqueous Solutions. *Chem. Mater.* **2016,** *28* (19), 6960-6967.

(37) Bhattacharyya, S.; Pang, S. H.; Dutzer, M. R.; Lively, R. P.; Walton, K. S.; Sholl, D. S.; Nair, S., Interactions of SO_2-Containing Acid Gases with ZIF-8: Structural Changes and Mechanistic Investigations. *J. Phys. Chem. C* **2016,** *120* (48), 27221-27229.

(38) Han, C.; Zhang, C. Y.; Tyminska, N.; Schmidt, J. R.; Sholl, D. S., Insights into the Stability of Zeolitic Imidazolate Frameworks in Humid Acidic Environments from First-Principles Calculations. *J. Phys. Chem. C* **2018,** *122* (8), 4339-4348.

(39) Wu, H.; Chua, Y. S.; Krungleviciute, V.; Tyagi, M.; Chen, P.; Yildirim, T.; Zhou, W., Unusual and Highly Tunable Missing-Linker Defects in Zirconium Metal-Organic Framework UiO-66 and Their Important Effects on Gas Adsorption. *J. Am. Chem. Soc.* **2013,** *135* (28), 10525-10532.

CHAPTER 2
METHODOLOGY

2.1 Introduction

The computations of my thesis work are based on two computational methods, which are density functional theory (DFT) and molecular dynamics (MD) simulations. DFT is a computational quantum mechanical modelling method to study the electronic structure of many-body systems.[1] In my calculations, DFT was adopted to investigate the structures and chemical properties of MOF materials. MD is a classical mechanical simulation method to investigate the interatomic interactions, where the movements and forces of atoms can be described by Newton's equation of motion.[2] MD simulations were employed in my study to calculate the diffusion properties of adsorbates in MOF materials. A brief introduction about the basic concepts of DFT and MD simulations is given in the following sections.

2.2 Density Functional Theory

2.2.1 Schrödinger Equation for Many-Body Problems

Density functional theory (DFT), first introduced in 1964 by Hohenberg and Kohn,[3] is now one of the most widely used quantum mechanics methods to solve the electronic quantum mechanical many-body problems. DFT uses electron density, rather than the wavefunction, as a fundamental variable.

The Schrödinger equation for a system containing M nuclei and N electrons can be written as

$$\left[-\frac{\hbar^2}{2}\sum_{I=1}^{M}\frac{1}{M_I}\nabla_I^2+\sum_{I=1}^{M}\sum_{J<I}U(\boldsymbol{R_I},\boldsymbol{R_J})-\frac{\hbar^2}{2m_e}\sum_{i=1}^{N}\nabla_i^2+\sum_{I=1}^{M}\sum_{i=1}^{N}V(\boldsymbol{R_I},\boldsymbol{r_i})\right.$$

$$\left.+\sum_{i=1}^{N}\sum_{j<i}W(\boldsymbol{r_i},\boldsymbol{r_j})\right]\Psi(\boldsymbol{R_1},\dots,\boldsymbol{R_M};\boldsymbol{r_1},\dots,\boldsymbol{r_N})$$

$$=E_{tot}\Psi(\boldsymbol{R_1},\dots,\boldsymbol{R_M};\boldsymbol{r_1},\dots,\boldsymbol{r_N}), \tag{2.1}$$

where all the terms in the brackets on the left-hand side compose the Hamiltonian of the system, where $-\frac{\hbar^2}{2}\sum_{I=1}^{M}\frac{1}{M_I}\nabla_I^2$ and $-\frac{\hbar^2}{2m_e}\sum_{i=1}^{N}\nabla_i^2$ are the kinetic energies of nuclei and electrons, respectively, $U(\boldsymbol{R_I},\boldsymbol{R_J})$, $V(\boldsymbol{R_I},\boldsymbol{r_i})$, and $W(\boldsymbol{r_i},\boldsymbol{r_j})$ are electrostatic potentials between nucleus and nucleus, nucleus and electron, and electron and electron, respectively. $\Psi(\boldsymbol{R_1},\dots,\boldsymbol{R_M};\boldsymbol{r_1},\dots,\boldsymbol{r_N})$ is the eigenfunction of the Hamiltonian, or a wavefunction, which is a function of coordinates of all nuclei ($\boldsymbol{R_i}$) and electrons ($\boldsymbol{r_i}$). E_{tot}, the eigenvalue, is the total energy of the system. Solving such an equation is very difficult as the wavefunction has as many as 3(N+M) variables.

To simplify the problem, we can separate the wavefunction in Equation 2.1 $\Psi(\boldsymbol{R_1},\dots,\boldsymbol{R_M};\boldsymbol{r_1},\dots,\boldsymbol{r_N})$ into two components, one for nuclei and the other for electrons based on the Born-Oppenheimer approximation, which assumes electrons, which are much less heavy than nuclei, respond instantaneously to any change in the nuclear positions. At a fixed nuclear configuration, the electronic Schrödinger equation is

$$\left[-\frac{\hbar^2}{2m_e}\sum_{i=1}^{N}\nabla_i^2+\sum_{i=1}^{N}V_{ext}(\boldsymbol{r_i})+\sum_{i=1}^{N}\sum_{j<i}W(\boldsymbol{r_i},\boldsymbol{r_j})\right]\psi(\boldsymbol{r_1},\dots,\boldsymbol{r_N})$$

$$=E\psi(\boldsymbol{r_1},\dots,\boldsymbol{r_N}), \tag{2.2}$$

where V_{ext} is the potential from the external field due to positively charged nuclei, $\psi(\boldsymbol{r_1},\dots,\boldsymbol{r_N})$ is the electronic wavefunction, and E is the total energy of electrons.

2.2.2 Solving the Schrödinger Equation

DFT is established on two Hohenberg-Kohn theorems.[3] The first theorem states that the ground state energy from Schrödinger equation is a unique functional of the electron density. Thus, by knowing the electron density for the ground state we can derive the ground-state energy. This theorem simplifies the problem of finding the ground-state energy by solving an equation with 3N variables to the same problem with only 3 variables. The electron density $n(\boldsymbol{r})$ can be expressed as an integral of normalized electron wavefunction over space,[4]

$$n(\boldsymbol{r})=N\int d^3r_2\dots\int d^3r_N\,\psi^*(\boldsymbol{r_1},\dots,\boldsymbol{r_N})\psi(\boldsymbol{r_1},\dots,\boldsymbol{r_N}). \tag{2.3}$$

Equation 2.3 can be solved, in principle, for the corresponding wavefunction, which is a functional of spatially dependent electron density,

$$\psi=\psi[n(\boldsymbol{r})]. \tag{2.4}$$

Similarly, the total electronic energy E is also a functional of electron density as

$$E[n(\boldsymbol{r})]=\left\langle\psi[n(\boldsymbol{r})]\middle|\hat{T}+\hat{V}+\hat{U}\middle|\psi[n(\boldsymbol{r})]\right\rangle, \tag{2.5}$$

where $\hat{T} + \hat{V} + \hat{U}$ is the Hamiltonian with $\hat{T}$ the kinetic energy, $\hat{V}$ the external potential, and $\hat{U}$ the electron-electron interaction. $\hat{T}$, $\hat{V}$, and $\hat{U}$ correspond to the three terms in the bracket of Equation 2.2 in order and each of them is also a functional of electron density. Of the three energies, $\hat{T}$ and $\hat{U}$ are called universal functionals as they are valid for any number of particles and any external potential, while $\hat{V}$ is a non-universal functional as it depends on the system.

The second Hohenberg-Kohn theorem states that the electron density that minimizes the energy of the overall functional is the true electron density corresponding to the full solution of the Schrödinger equation. In other words, the ground-state energy can be found by minimizing $E[n(\boldsymbol{r})]$ based on the minimal property of the ground state provided that the form of $E[n(\boldsymbol{r})]$ is known. This theorem is a guidance for searching for appropriate approximation forms of the functional.

One of the widely used approach that applies Hohenberg-Kohn theorems to practical computations was introduced by Kohn and Sham in 1965.[5] They established the so-called Kohn-Sham equation,

$$\left[-\frac{\hbar^2}{2m_e}\nabla^2 + V_{ext}(\boldsymbol{r}) + V_H(\boldsymbol{r}) + V_{XC}(\boldsymbol{r})\right]\phi_i(\boldsymbol{r}) = \varepsilon_i\phi_i(\boldsymbol{r}), \tag{2.6}$$

where $\phi_i(\boldsymbol{r})$ is the single-electron orbital, which is closely related to the electron density,

$$n(\boldsymbol{r}) = 2\sum_{i=1}\phi_i^*(\boldsymbol{r})\phi_i(\boldsymbol{r}). \tag{2.7}$$

Here, the factor of 2 on the right-hand side is because of Pauli exclusion principles that electrons of opposite spins can occupy the same atomic orbital. $V_{ext}(\boldsymbol{r})$ is the external

potential, which also appears in Equation 2.2, $V_H(\boldsymbol{r})$ is Hartree potential describing the Coulomb repulsion between the electrons, which has the form of

$$V_H(\boldsymbol{r}) = e^2 \int \frac{n(\boldsymbol{r}')}{|\boldsymbol{r} - \boldsymbol{r}'|} d^3r', \tag{2.8}$$

and $V_{XC}(\boldsymbol{r})$ is the exchange-correlation potential, which includes all the quantum mechanical effects that are not included in the left three terms.

$$V_{XC}(\boldsymbol{r}) = \frac{\delta E_{XC}[n(\boldsymbol{r})]}{\delta n(\boldsymbol{r})}. \tag{2.9}$$

Note that Hartree potential includes the interaction between an electron and itself, which is unphysical and requires a correction to Equation 2.8. This correction is lumped into equation 2.9. The Kohn-Sham equation converts the problem of solving a multiple-electron Schrödinger equation to a single-particle Schrödinger equation.

2.2.3 Local Density Approximation and Generalized Gradient Approximation Exchange-Correlation Functionals

The main challenge in utilizing DFT is that the accurate form of the exchange-correlation (XC) functional (Equation 2.9) is unknown except for the uniform electron gas, which has the electron density as a constant that is independent of spatial variables. Kohn and Sham stated that if $n(\boldsymbol{r})$ is sufficiently slowly varying, the exchange-correlation energy can be expressed as

$$E_{XC}[n] = \int n(\boldsymbol{r}) \epsilon_{XC}(n(\boldsymbol{r})) d\boldsymbol{r}, \tag{2.10}$$

where $\epsilon_{XC}(n)$ is the exchange and correlation energy per electron of a uniform electron gas of density n.[5] This approximation uses the local electron density to define the exchange-correlation functional, so it is called the local density approximation (LDA).

It is not surprising that LDA fails for the systems that have strong electron-electron interactions.[6] To improve the approximation for such systems, many exchange-correlation functionals have been proposed, of which the generalized gradient approximation (GGA) is the most widely used. GGA incorporates the effects of inhomogeneity in electron density by applying gradient corrections, so that

$$E_{XC}[n] = \int n(\boldsymbol{r})\epsilon_{XC}(\boldsymbol{r})F[(n(\boldsymbol{r}), \nabla n(\boldsymbol{r})]d\boldsymbol{r}, \tag{2.11}$$

where $F[(n(\boldsymbol{r}), \nabla n(\boldsymbol{r})]$ is an enhancement factor, depending on both local density and local gradient of density. The most widely used GGA functionals in practical DFT calculations are PW91 by Perdew and Wang[7] and PBE by Perdew, Burke, and Ernzerhof.[8]

2.2.4 Dispersion Corrections

Many commonly used exchange-correlation functionals such as PBE and B3LYP fail to describe the long-range dispersion interaction correctly.[9] It is important to include the dispersion corrections for systems, of which the total energy is largely contributed by noncovalent interactions such as hydrogen bonds, van der Waals forces, and π-π interactions.[10] A commonly used semi-classical correction is called the DFT-D (DFT + dispersion), which is based on an atom pairwise additive treatment of dispersion energy. The general form of dispersion energy is

$$E_{disp}^{DFT-D} = -\sum_{AB}\sum_{n=6,8,10\ldots} s_n \frac{C_n^{AB}}{R_{AB}^n} f_{damp}(R_{AB}), \quad (2.12)$$

where the sum is over all atom pairs in the systems with R_{AB} denoting the internuclear distance of atom pair AB, C_n^{AB} is the averaged *n*th-order dispersion coefficient (orders n = 6, 8 10…), and s_n is a global scaling factor to adjust the repulsive behavior.[9] f_{damp} is a damping function to avoid near-singularities for small R_{AB}.[9] In my thesis work, I used the DFT-D2 and -D3 methods to calculate the dispersion energy of MOF systems. The DFT-D2 method includes one multipole-term that depends to the sixth order on the distance R_{AB} between atoms A and B, while the DFT-D3 method depends on two multipole-terms, sixth order and eighth order with dispersion coefficients.[11]

2.3 Molecular Dynamics Simulations

2.3.1 The Idea of Molecular Dynamics Simulations

Molecular Dynamics (MD) simulation is a technique for studying the physical movements of atoms and molecules.[2] The motion of particles obeys the law of classical mechanics, so their trajectories can be determined by solving the Newton's equation of motion for a system of interacting particles, where the interaction is described by force fields. The idea of MD simulation follows similar approach as experiments. To perform a real experiment, the first step is to prepare a sample of the material that we wish to study, which in a MD simulation is the initialization of a system. For instance, for a system containing N particles, to start a simulation, we assign initial positions and velocities to all particles in the system. After the preparation of a sample in a real experiment, we then use some instruments to measure the property of interest during a certain time interval, and

usually the longer time interval the more accurate the measurement becomes. Analogously, in a MD simulation, we solve Newton's equations of motion for this system to calculate the force on each particle and accordingly update the information such as velocity, temperature, and energy until the average properties of the system no longer change with time.

The force calculation is the most time-consuming part for most MD simulations because we need to calculate the force acting on every particle, which involves $O(N^2)$ evaluations with only considering pairwise additive interactions for a N-particle system, where the contributions to the force on a particle is due to all its neighbors (Figure 2.1). The potential energy of the system can be estimated by using interatomic potentials, for example, the Lennard-Jones (LJ) potential, which is a simple model that approximates the dispersive interaction between a pair of neutral atoms or molecules,

$$U_{LJ}(r) = 4\epsilon\left[\left(\frac{\sigma}{r}\right)^{12} - \left(\frac{\sigma}{r}\right)^{6}\right]. \tag{2.13}$$

The first derivative of the potential is the force in a specific direction. Taking the x-component as an example, the corresponding force for the LJ potential is

$$f_x(r) = -\frac{\partial u(r)}{\partial x} = \frac{48\epsilon x}{r^2}\left[\left(\frac{\sigma}{r}\right)^{12} - 0.5\left(\frac{\sigma}{r}\right)^{6}\right]. \tag{2.14}$$

With the forces known, we can then use them to integrate Newton's equations of motion. There are many algorithms for this purpose, of which a simple but also usually the best one is called the Verlet algorithm, where the positions of a particle in successive time steps are related by the following equation,

$$r(t+\Delta t) \approx 2r(t) - r(t-\Delta t) + \frac{f(t)}{m}\Delta t^2. \quad (2.15)$$

Note that in Equation 2.15, the variables involved are merely force and positions in previous time steps without velocities, which can be derived using the position information and time steps.

This section has made a brief tour for a typical procedure in a time step of a MD simulation. The systems studied by MD simulations are in the regime that the specific trajectory depends sensitively to the initial conditions. It is important to use MD simulations to accumulate averaged predictions rather than highly specific details from individual trajectories.

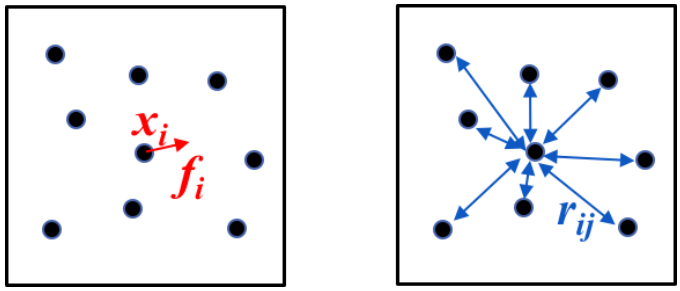

Figure 2.1 Illustration of a N-particle system and the physical variables position (x_i), force (f_i), and pairwise distance (r_{ij}) computed in a typical molecular dynamics simulation.

2.3.2 Molecular Dynamics Simulations for Diffusion

Self-diffusion coefficient is a property of great interest in the study of porous materials and MD simulation is an efficient method to calculate this property.[2] Self-diffusivity describes the random motion of a molecule in the absence of any gradients that

case a mass flux, in other words, it is a motion under equilibrium condition**.** A commonly used technique to obtain self-diffusion coefficient by MD simulations is to monitor molecule positions in a time interval, then calculate the slope of the mean square displacement (MSD)[12] at long times,

$$D_\alpha^S = \frac{1}{2dN_\alpha} \lim_{t\to\infty} \frac{d}{dt} \left\langle \sum_{i=1}^{N_\alpha} (r_i^\alpha(t) - r_i^\alpha(0))^2 \right\rangle, \tag{2.16}$$

where D_α^S is the self-diffusion coefficient of component α, N_α is the number of molecules of component α, and *d* is the spatial dimension of the system, which can be 1, 2 or 3. The position of each molecule, $r_i^\alpha(t)$, is recorded every time step during MD simulations. Equation 2.16 is also called the Einstein's relationship.[13]

2.3.3 Transition State Theory Method: Umbrella Sampling

Conventional MSD method works efficiently for the situations where molecules diffuse relatively fast, typically with a self-diffusion coefficient greater than 10^{-8} cm^2/s.[14] For MOF materials, in which the adsorbates diffuse through pores, extensive computational studies have been reported using MSD method to investigate self-diffusion of adsorbates. Almost all of these studies have MOFs with greater pore size than the adsorbate's size. However, if the adsorbate's size is as large as or larger than the pore size, can we still use MSD methods to obtain self-diffusion coefficient? The answer is yes and no. We can still perform a regular MD simulation, but the MSD plot as a function of time will be almost flat as Figure 2.2b shows, rather than a straight line with a slope. Because the adsorbate could not overcome a high barrier to hop from one state to another, as a result, it is wandering inside a local area, as Figure 2.2a shows. Thus, the MSD for the molecule in

Figure 2.2a is within the range of a cage size. The diffusion coefficient derived by this MSD curve is far from accurate. Thus, we need to turn to other ways to obtain self-diffusion coefficient, such as transition state theory (TST).[15] Instead of computing positions, TST method computes hopping rate between two states.

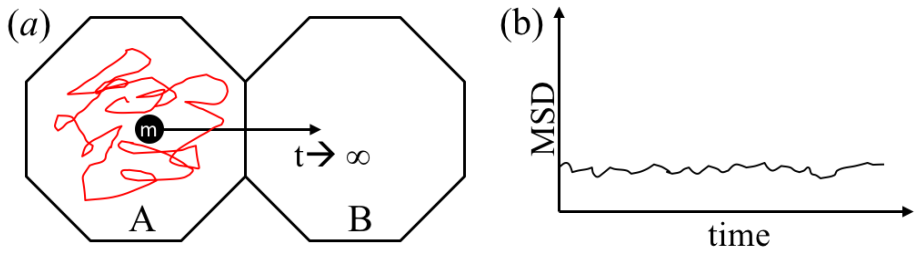

Figure 2.2 Illustration of the challenge of MSD method in slowly-diffusing situations. (a) A molecule moving through cages in porous materials, where the red arbitrary curves represent its moving trajectory and the black arrow pointing from cages A to B denotes the one of the hopping directions of the molecule during diffusion. (b) the mean-square displacement as a function of time for the molecule shown in (a) during a typical MD simulation time.

TST computes a rate constant for hopping between states A and B by computing the equilibrium particle flux through the dividing surface. Figure 2.3a shows a cross section of a channel in a porous material, the net diffusion of adsorbates is along the horizontal axis. In this scheme, because the energy barrier is usually high, the diffusion can be described as hopping from cage to cage through a pore connecting the two cages. The position tagged in red is at the dividing surface q*, which is at the position of a pore connecting two cages. The both sides of this dividing surface are two well-defined states A and B, which are two distinct cages with q_A and q_B denoting the positions of local

minimum-energy states within each cage. The position of transition state (TS) is at q*, which together with the energy barrier are what we want to determine using TST methods.

The hopping rate $k_{A\to B}$ for an adsorbate from states A to B can be expressed as

$$k_{A\to B} = \kappa \sqrt{\frac{k_B T}{2\pi m}} \frac{e^{-\beta F(q^*)}}{\int_{state\ A} e^{-\beta F(q)} dq}, \tag{2.17}$$

where k_B, T, m, and κ are Boltzmann constant, temperature, mass of adsorbate, and dynamical correction factor, respectively. $\beta = {}^{1}/_{k_B T}$. The most straightforward TST methods assume that all the particle from state A reaching TS will all falls into state B, ignoring recrossings. This assumption may not affect the particles with relatively low energy barriers, but can change the rate constant of those with high energy barriers by several orders of magnitude. This problem can be solved by computing the dynamical correction factor, which is in the range of 0 and 1.[14]

The TST method used in this thesis, umbrella sampling,[16] is a biased MD method that provide free energy profile along a reaction coordinate by using a bias potential to constrain sampling over a reaction coordinate. Take the case in Figure 2.3a as an example, since the free energy barrier is high, which reduces the probability of sampling close to the location of TS using direct MD simulation, as the probability is proportional to $exp[-\beta F(r)]$. To solve this problem, a bias potential is added to the adsorbate to increase the probability of sampling close to TS. The simplest form of the bias potential is harmonic oscillator with the equilibrium state at a specific position along the reaction coordinate. In the practical simulations using umbrella sampling, as Figure 2.3b shows, a series of "umbrellas" are arranged along the reaction coordinate, with each one constraining the sampling within the

space enclosed by the umbrella. The artificial bias potential can be subtracted from the resulted free energy by using methods such as Weighted Histogram Analysis Method.[2]

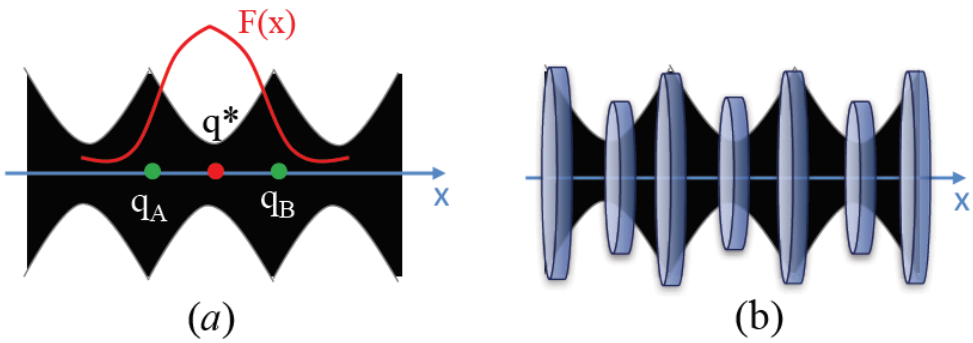

Figure 2.3 (a) Illustration of energy states of an adsorbate along a one-dimensional reaction coordinate. The black part is the space where adsorbate can move, the two green points are the positions of local minimum-energy states (q_A and q_B) along x direction, and the red point corresponds to the position of the transition state (q*). The red curve is the free energy profile for the adsorbate along x direction. (b) Illustration of umbrella sampling applied to the system shown in (a) for calculating the free energy profile, where the thin cylinders perpendicular to x-axis represent the umbrellas, where the adsorbates are constrained because of the bias potential.

2.4 References

(1) Sholl, D.; Steckel, J. A., *Density Functional Theory: A Practical Introduction*. Wiley: 2009.

(2) Frenkel, D.; Smit, B., *Understanding Molecular Simulation : From Algorithms to Applications*. 2nd ed.; Academic Press: San Diego, 2002.

(3) Hohenberg, P.; Kohn, W., Inhomogeneous Electron Gas. *Phys. Rev. B* **1964,** *136* (3B), B864.

(4) Capelle, K., A bird's-eye view of density-functional theory. *Braz. J. Phys.* **2006,** *36* (4a), 1318-1343.

(5) Kohn, W.; Sham, L. J., Self-Consistent Equations Including Exchange and Correlation Effects. *Phys. Rev.* **1965,** *140* (4A), 1133.

(6) Kohn, W., Nobel Lecture: Electronic structure of matter-wave functions and density functionals. *Rev. Mod. Phys.* **1999,** *71* (5), 1253-1266.

(7) Perdew, J. P.; Wang, Y., Accurate and Simple Analytic Representation of the Electron-Gas Correlation-Energy. *Phys. Rev. B* **1992,** *45* (23), 13244-13249.

(8) Perdew, J. P.; Burke, K.; Ernzerhof, M., Generalized gradient approximation made simple. *Phys. Rev. Lett.* **1996,** *77* (18), 3865-3868.

(9) Grimme, S., Density functional theory with London dispersion corrections. *WIREs Comput. Mol. Sci.* **2011,** *1* (2), 211-228.

(10) Thanthiriwatte, K. S.; Hohenstein, E. G.; Burns, L. A.; Sherrill, C. D., Assessment of the Performance of DFT and DFT-D Methods for Describing Distance Dependence of Hydrogen-Bonded Interactions. *J Chem. Theory Comput.* **2011,** *7* (1), 88-96.

(11) Goerigk, L., Chapter 6 - A Comprehensive Overview of the DFT-D3 London-Dispersion Correction. In *Non-Covalent Interactions in Quantum Chemistry and Physics*, Otero de la Roza, A.; DiLabio, G. A., Eds. Elsevier: 2017; pp 195-219.

(12) Vanmegen, W.; Underwood, S. M., Tracer Diffusion in Concentrated Colloidal Dispersions .III. Mean Squared Displacements and Self-Diffusion Coefficients. *J. Chem. Phys.* **1989,** *91* (1), 552-559.

(13) Einstein, A., *Investigations on the Theory of Brownian Movement*. Courier Dover Publications: 1956.

(14) Verploegh, R. J.; Nair, S.; Sholl, D. S., Temperature and Loading-Dependent Diffusion of Light Hydrocarbons in ZIF-8 as Predicted Through Fully Flexible Molecular Simulations. *J. Am. Chem. Soc.* **2015,** *137* (50), 15760-15771.

(15) Truhlar, D. G.; Garrett, B. C.; Klippenstein, S. J., Current status of transition-state theory. *J. Phys. Chem.* **1996,** *100* (31), 12771-12800.

(16) Kastner, J., Umbrella sampling. *WIREs Comput. Mol. Sci.* **2011,** *1* (6), 932-942.

CHAPTER 3

COMPUTATIONAL CHARACTERIZATION OF DEFECTS IN METAL-ORGANIC FRAMEWORKS: SPONTANEOUS AND WATER-INDUCED POINT DEFECTS IN ZIF-8*

3.1 Introduction

Metal-organic frameworks (MOFs) are nanoporous crystalline materials composed of metal cations coordinated by bridging organic linkers.[1] Within the large family of MOFs, zeolitic-imidazolate frameworks (ZIFs), composed of tetrahedrally coordinated zinc or cobalt cations and bridging imidazolate (Im) ligands, have received special attention due to their unusual stability, structural and chemical diversity and their promising applications including sensing,[2] storage and separation of gases,[3-11] drug delivery,[12-13] and catalysis.[14] The bulk structure of ZIFs and other MOFs are typically well understood on the basis of X-ray diffraction (XRD) experiments, and large collections of crystal structures are now available.[15] In the specific case of ZIFs, the similarity of the Zn-Im-Zn bond angle to the

*Portions of this chapter have been published previously in articles "Computational Characterization of Defects in Metal–Organic Frameworks: Spontaneous and Water-Induced Point Defects in ZIF-8" by Chenyang Zhang, Chu Han, David Sholl, and J.R. Schmidt in the *Journal of Physical Chemistry Letters*, 2016, volume 7, issue 3, pages 459—464, "Facet-Specific Stability of ZIF-8 in the Presence of Acid Gases Dissolved in Aqueous Solutions" by Simon Pang, Chu Han, David Sholl, Christopher Jones, and Ryan Lively in *Chemistry of Materials*, 2016, volume 28, issue 19, pages 6960—6967, and "Synergistic Effects of Water and SO_2 on Degradation of MIL-125 in the Presence of Acid Gases" by William Mounfield, Chu Han, Simon Pang, Uma Tumuluri, Yang Jiao, Souryadeep Bhattacharyya, Michael Dutzer, Sankar Nair, Zili Wu, Ryan Lively, David Sholl, and Krista Walton in the *Journal of Physical Chemistry C*, 2016, volume 120, issue 48, pages 27230—27240.

Si-O-Si angle in conventional silicon-based zeolites gives rise to topologically similar crystal structures. Yet in contrast with zeolites,[16-20] whose defect structures are well known and well characterized, comparatively little is known with regard to the structure and stability of elementary point defect structures (e.g., metal/ligand vacancy, dangling linkers) within ZIFs and other MOF crystals,[21] and direct experimental evidence of such defects (especially in stable, low-coordination-number MOFs such as ZIFs) is sparse. Nonetheless, such defects likely play an important role in influencing the physical properties,[22] reactivity,[23-29] and long-term stability[21,30-31] of MOFs.

Motivated by similarities with traditional zeolites, we computationally examine the thermodynamic stability and kinetic accessibility of various point defects in ZIFs. We assess the thermodynamic stability of each defect by calculating the energy change of a putative defect formation reaction, under both synthetic (solution-phase) and postsynthetic (gas-phase) conditions. By analogy to defects known to exist in zeolites, we examine both metal/linker vacancies as well as potential "dangling" linker groups (Figure 3.1).[21,32-34] We also study the kinetic feasibility of defect formation and discuss the implications of our results in terms of the reactivity and long-term stability of MOFs under working conditions that may involve exposure to water vapor or acid gases.[35]

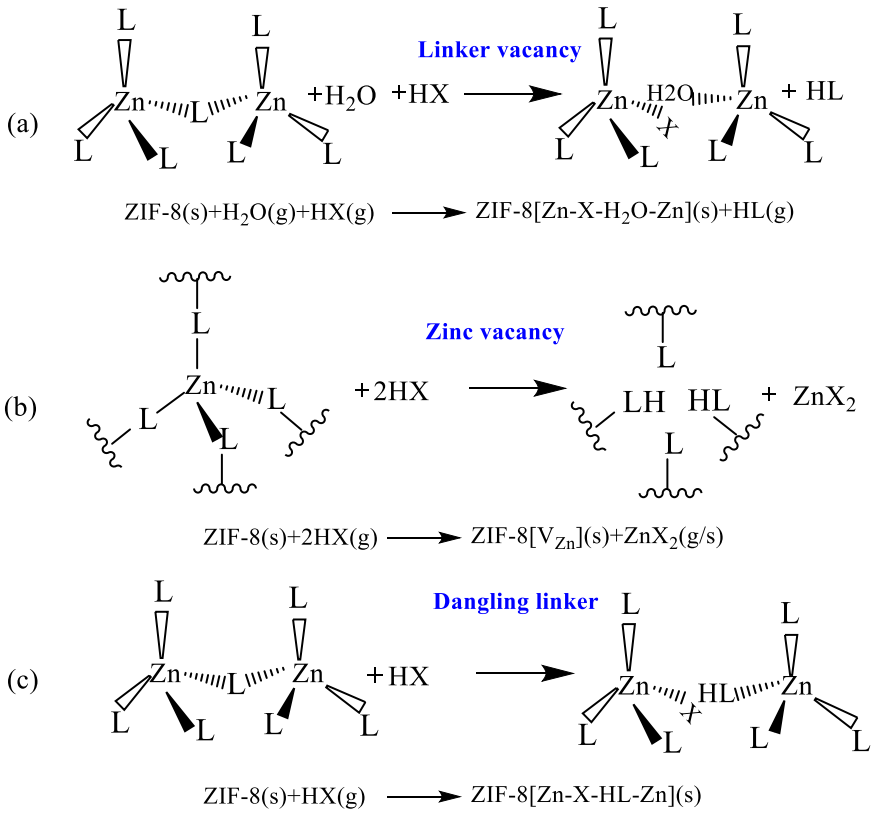

Figure 3.1 Schematic illustration of various potential ZIF point defects and associated formation reactions: (a) Linker vacancy, (b) Zinc vacancy and (c) Dangling linker. X = OH^-, NO_3^-, or $COOH^-$. Zn-X-H_2O-Zn, V_{Zn}, Zn-X-HL-Zn denotes a linker vacancy, zinc vacancy, and dangling linker, respectively.

We utilize ZIF-8 as prototypical model ZIF. ZIF-8 is composed of zinc(II) cations coordinated by 2-methylimidzaolate ligands and forms a porous crystalline solid with sodalite topology.[36] Although our calculations focus on ZIF-8, we expect our qualitative conclusions to be transferable to other ZIFs, which differ only in the functionalization of the organic linker. For each putative defect formation reaction, we use density functional theory (DFT) calculations to estimate the associated energy change relative to the bulk, defect-free structure, under either synthetic or post-synthetic conditions. These scenarios are distinguished by the presence or absence of solvent, typically (in the case of ZIFs)

DMF,[36] methanol,[37] or water.[38] We include such solvation effects using a combination of experimentally measured or computationally estimated aqueous solvation enthalpies. Within these defect formation reactions, we include the possibility of reactions involving water (either ambient or residual solvent), NO_3^- (a typical counterion during synthesis), or formate (a modulator often used in ZIF synthesis).[39-40] Because our goal is to examine the plausibility of various defects rather than to estimate absolute defect concentrations, we neglect entropic effects, the inclusion of which is both challenging due to the anharmonicity of low frequency phonons as well as the uncertainty in solution-phase translation/rotational entropy and unlikely to qualitatively alter our conclusions (Table A.5).

Based on the point defects proposed in bulk ZIF-8, we perform computational investigation on the degradation mechanisms for ZIF-8 external surfaces and MIL-125, which exhibit degradation after exposure to acid gases. Degradation of MOFs presumably begins with the formation of point defects. Our simulations show that the observed degraded structures are likely similar to the point defects proposed in bulk ZIF-8. The experimental observations utilizing techniques including scanning electron microscopy, X-ray photoelectron spectra, and FTIR spectra support our hypothesis. This chapter details the computational methods and atomistic models for the investigation of point defects in ZIF-8. The models are then applied to characterize similar defects in other MOF systems, which have been observed in experiments.

3.2 Formation of Point Defects in ZIFs

Based on the similarity of geometry between ZIFs and zeolites, we proposed three types of point defects for ZIF-8, whose models are based on the observed point defects in silicon-based zeolites.[16-20] As Figure 3.1 shows, they are linker vacancy, metal vacancy, and dangling linker. Similar to an oxygen vacancy in zeolites, a linker vacancy can be formed by removing a neutral, protonated imidazole linker (to the gas-phase or bulk solution) via reaction with a water and an additional proton donating group (Figure 3.1a). Within the context of this simple description, the resulting two unsaturated metal sites are then filled by an associating water and the conjugate base of the proton donating group. We also consider the possibility of forming a metal cation vacancy, analogous with well-known tetrahedral vacancies in zeolites (Figure 3.1b).[21,33] Within our model, two of the resulting unsaturated linkers are protonated by two proton-donating groups, with the zinc reacting with the resulting conjugate base. The increased conformational flexibility and linker group size of ZIFs relative to zeolites offers the possibility for an additional defect type: a "dangling" linker group, where the "bridging" imidazolate linker is bound to one, rather than two, adjacent zinc cations. This defect can also be considered an intermediate in the pathway to a linker vacancy. Within our model, the dangling linker is generated via reaction of the ZIF with a single proton donating group (Figure 3.1c).

The thermodynamic stability of a defect is evaluated by its formation energy, which is defined as the difference between the total energy of products and that of reactants,

$$\Delta E = E_{defect} - E_{perfect} - \sum E_{molecule}, \tag{3.1}$$

where E_{defect}, $E_{perfect}$, and $E_{molecule}$ are energies of a defective ZIF-8 unit cell, a defect-free ZIF-8 unit cell, and a reacting molecule (H_2O or HX), respectively. A positive formation energy denotes that the formation of a defect is an endothermic reaction.

The kinetic stability of a defect is evaluated by its activation energy for the formation reaction, ΔE^a. ΔE^a is defined as the difference between the energies of the transition state and the initial state of a system.

3.3 Computational Methods

A periodic model of ZIF-8 was constructed from the XRD crystal structure obtained from the Cambridge Structural Database (CSD).[36] The cubic unit cell includes 276 atoms with a lattice constant of 16.991 Å. Periodic calculations utilized the Vienna *Ab initio* Simulation Package (VASP) in conjunction with a 600 eV energy cutoff and a projector-augmented wave (PAW) treatment of core electrons.[41-46] All structural optimizations utilized the PBE functional with the lattice constant fixed to that of the defect-free ZIF, and atoms were relaxed to a tolerance of 10^{-2} eV/Å. The use of the fixed, defect-free, lattice constant is motivated by the desire to study defect formation thermodynamics at the expected (low) concentration, where the ZIF lattice constant will be unaltered by dilute defects; due to periodic boundary conditions, relaxation of the lattice for defective structures would be representative of unphysically high defect concentrations. All energy differences were subsequently evaluated using both dispersion-corrected PBE-D3 (Table 3.1) and also the hybrid B3LYP-D3 functional (Table A.1); the energetics are qualitatively unchanged at the B3LYP-D3 level. The PBE geometries are used in all cases for

consistency and efficiency, resulting in energy differences of <1 kcal/mol with respect to full optimizations (Tables A.2 and A.3). Energy differences involving isolated molecules were evaluated by placing the molecule within a box with the same dimensions as the unit cell to generate a consistent periodic system (Figure A.2). Zero-point corrections were calculated and applied based on a normal-mode analysis at the PBE level.

Reaction pathway investigations were performed via the nudged elastic band (NEB) method on the full, periodic, ZIF-8 unit cell using eight images for each of the two reaction steps and then refined via climbing-image NEB.[47-48] The resulting images are approximately evenly distributed along the minimum energy pathway connecting reactants and products according to the NEB scheme.

Solution-phase energy differences were calculated by adding a solvation corrections to all reactants and products in each defect formation reaction (Figure A.4). Aqueous solvation energies for simple species (H_2O, HNO_3, HCOOH, $Zn(NO_3)_2$, $Zn(OH)_2$) were estimated using experimentally measured enthalpies of dissolution/condensation (Table A.4). For gaseous reagents, ideal gas behavior was assumed for conversions for enthalpies to energies. Aqueous solvation energies for the remaining species were estimated computationally using finite "cluster" models in conjunction with the SMD[49] polarizable continuum solvation model. These solvation energies were added to the (periodic) gas-phase reaction energetics to yield estimates for the corresponding solution-phase reactions. See Appendix A for complete details.

3.4 Results and Discussion

3.4.1 Thermodynamic Stability of Possible Defects in ZIF-8

Calculated zero-point corrected gas-phase (ΔE^{gas}) and solution-phase (ΔE^{soln}) defect formation energies are shown in Table 3.1. The local optimized structures of resulting defects are shown in Figure 3.2. Gas-phase defect formation energies of a linker vacancy (Figure 3.1a, reactions (i)-(iii) of Table 3.1) range between -0.5 and 14.5 kcal/mol, depending on the nature of the proton donating group. Note that these energies are calculated with respect to non-interacting reactants and products; as such, a significant energetic contribution comes from desorption of the resulting gas-phase imidazole from the ZIF. Since it is likely that the imidazole would remain adsorbed within the ZIF, we also calculate energies relative to the interacting products (e.g. adsorbed imidazole), yielding smaller formation energies between -8.0 and -3.6 kcal/mol (numbers in parentheses in Table 3.1 and Figure A.3). Including solvation effects for the reactants and products, we estimate the corresponding aqueous solution-phase linker vacancy formation energies to be slightly more favorable, between -3.8 and 10.6 kcal/mol (-11.3 to -7.5 for adsorbed imidazole). Crucially, irrespective of the details of the proposed formation, many of the resulting formation energies are approximately thermoneutral or even exothermic, suggesting the thermodynamic plausibility of linker vacancy point defects under ambient conditions. Of course, formation of such a linker vacancy requires cleavage of two strong metal-ligand dative bonds and thus likely presents significant kinetic barriers (vide infra).

Table 3.1 Formation energies of the possible point defects in ZIF-8. All energetics are calculated at the PBE-D3 level with values given in kcal/mol. ΔE^{gas}, $\Delta\Delta E^{solv}$, and ΔE^{soln} denote the gas-phase defect formation reaction energy (Figure 3.1), solvation correction, and resulting solution-phase formation energy. Numbers in square brackets correspond to gas-phase ion-paired $Zn(OH)_2$/$Zn(NO_3)_2$ products, which are shown alongside results assuming crystalline salt products. In the case of linker vacancies, energies in parentheses are taken with respect to interacting product complex; all other energies are with respect to non-interacting reactants and products.

(kcal/mol)		**Defect**	ΔE^{gas}	$\Delta\Delta E^{solv}$	ΔE^{soln}
Linker vacancy	(i)	Zn-OH…H_2O-Zn	14.5 (-3.6)	-3.9	10.6 (-7.5)
	(ii)	Zn-NO_3… H_2O-Zn	3.8 (-6.2)	-2.8	1.0 (-9.0)
	(iii)	Zn-COOH…H_2O-Zn	-0.5 (-8.0)	-3.3	-3.8 (-11.3)
Zn vacancy	(iv)	V_{Zn}[$Zn(OH)_2$]	-5.9 [46.0]	26.9	21.0
	(v)	V_{Zn}[$Zn(NO_3)_2$]	-38.2 [21.8]	13.2	-25.0
Dangling linker	(vi)	Zn-OH…HmIM-Zn	11.9	8.8	20.7
	(vii)	Zn-NO_3…HmIM-Zn	6.2	6.8	13.0
	(viii)	Zn-COOH…HmIM-Zn	2.9	0.5	3.4

In the gas-phase, the most mechanistically feasible zinc-containing product in the reactions forming a metal cation vacancy (Figure 3.1b, reactions (iv)-(v) of Table 3.1 and Figure A.2) is an ion-paired salt complex. The resulting defect formation energies range between about 20 and 50 kcal/mol due to the relative instability of the ion-pair (numbers given in brackets in Table 3.1). Alternatively, the defect energy can be calculated relative to solid (crystalline) salt products, yielding much lower energies between -5.9 and -38.2 kcal/mol, although the formation of such a crystalline salt product within a gas-phase reaction seems mechanistically unlikely. The solution-phase metal vacancy formation energies were calculated assuming a (potentially partially) dissolved salt product, with energies of -25.0 kcal/mol (for X = NO_3^-) and 21.0 kcal/mol (X = OH^-), with the former driven both by stronger proton donating power and by solvation of the resulting (soluble)

$Zn(NO_3)_2$ salt. Once again, based purely on the thermodynamics of the defect formation reactions (neglecting entropic factors), metal vacancy formation within ZIF-8 is thermodynamically plausible.

Whether in the gas- or solution-phase, the resulting defect formation energies for a dangling linker (Figure 3.1c, reactions (vi)-(viii) of Table 3.1 and Figure A.2) are typically higher, between 2.9 and11.9 (gas-phase) and 3.4—20.7 (solution-phase) kcal/mol. Analysis of our DFT energies suggests that the increase in dangling linker formation energy relative to linker vacancies is driven by the strain/deformation of the ZIF lattice, which must accommodate the bulky dangling imidazolate linker within the confined ZIF pore. This deformation energy might be reduced for ZIFs containing a larger pore diameter. The higher formation energy of dangling linkers versus linker vacancies suggests a decreased concentration of the former relative to the latter, and considering the dangling linker as an intermediate towards linker vacancy formation, also provides one possible explanation for the observed thermal and chemical kinetic stability of ZIFs.[4,6,36,50]

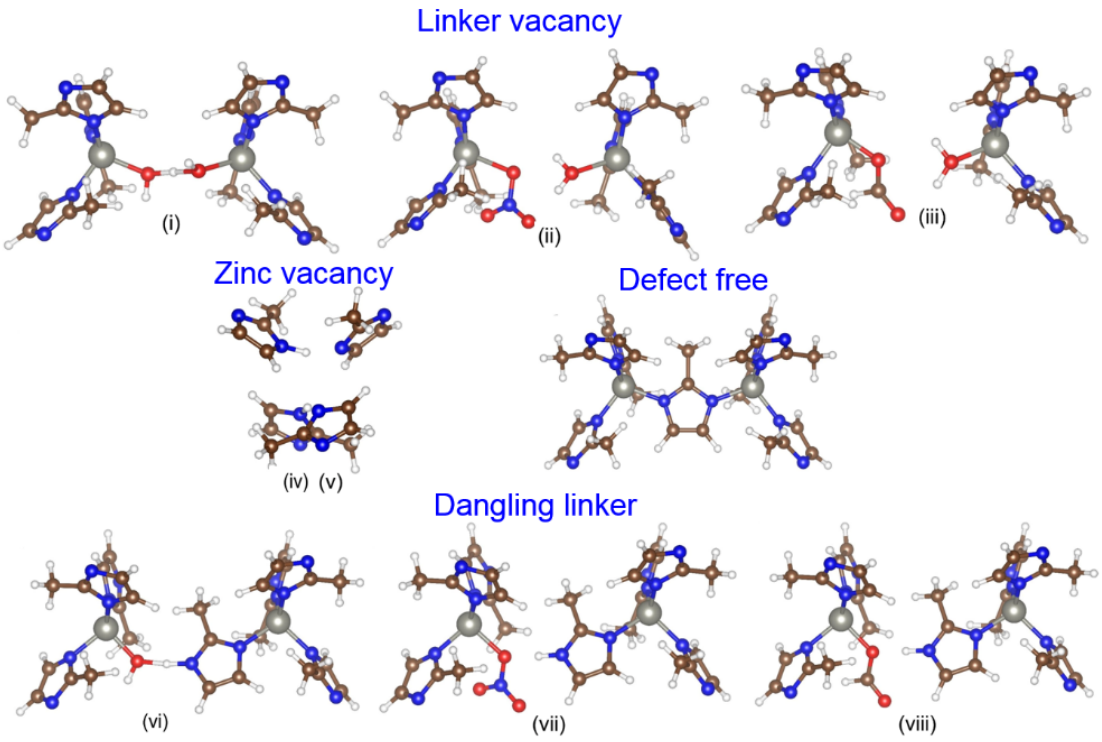

Figure 3.2 Local structures of the defects in ZIF-8. (Numbering corresponds to the defect formation reactions in Table 3.1) Linker vacancies (i – iii), zinc vacancies (iv – v), and dangling linkers (vi – viii). The local structure of defect-free ZIF-8 is shown for comparison. H, C, N, O, and Zn are shown in white, brown, blue, red, and gray, respectively. Reactions iv/v yield identical point defect structure.

Our results also suggest a possible explanation for well-known post-synthetic linker[37,51-53] and metal[37] exchange processes in ZIFs. In such post-synthetic exchange processes, a ZIF is submerged into a concentrated solution of an alternative linker group or metal, where slow in situ replacement of the linker/metal via a single-crystal to single-crystal transformation is observed. In the case of ZIF-8 linker exchange, one example of such a process requires elevated temperatures (100°C) and extended reaction times (~6 days), resulting in ~85% replacement of the methyl-imidazolate by an unfunctionalized imidazolate and yielding a structure that cannot be accessed via direct synthesis.[52] We hypothesize that such single-crystal transformations could be driven by the transient

formation of point defects, including metal/linker vacancies, that are then quenched by replacement with an alternative linker/metal.[52] Recent experimental evidence suggests that these defects need not be merely transient. Cheng *et al.*[54] measured the XRD pattern of ZIF-8 exposed to liquid water and found evidence for several new XRD peaks that increased in intensity with exposure while the original diffraction peaks decreased. They also find IR evidence for water that cannot be desorbed even at 100°C. They interpret this data in terms of water-terminated defect sites and find that these defects permanently increase the H_2 uptake of the material.

3.4.2 Kinetic Stability of Water-Induced Point Defects in ZIF-8

Insight regarding the kinetics of defect formation can be gained by examining the activation energy and minimum energy pathway associated with defect formation. This reaction pathway is shown for linker vacancy formation (reaction (i) of Table 3.1) in Figure 3.3. Starting with a defect-free ZIF, linker vacancy formation proceeds via reaction with water over a barrier of ~22 kcal/mol to form a metastable dangling linker intermediate. Reaction with a second water proceeds with a higher effective barrier of ~29 kcal/mol, leading to a relatively low-energy linker vacancy defect. Both barriers are estimated under gas-phase conditions and may be modified slightly by inclusion of solvent effects. The overall energetics presented here differ slightly from the data in Table 3.1, since the latter energetics are taken with respect to non-interacting reactants/products. The calculated reaction barriers are sizable, reflecting the observed thermal and kinetic stability of ZIFs in aqueous solution. Nonetheless, crude transition state theory calculations ($k(T) = \frac{k_B T}{h} e^{-\Delta^{\ddagger} E/RT}$, neglecting all entropic effects) would predict the barrier to dangling linker formation to be surmountable at room temperature on a timescale of ~1 hour, consistent

with recent observations of water-terminated defect sites (presumably dangling linkers) in ZIF-8 under ambient conditions.[54] The higher effective barrier to linker vacancy formation would be accessible only at higher temperatures, with transition-state theory predicting timescales of ~5 h at 100°C. In both cases, inclusion of solvation effects may slightly reduce the calculated barrier, while use of hybrid functionals may somewhat increase the barrier. Nonetheless, an effective barrier of this magnitude is qualitatively consistent with the experimental conditions required for linker exchange.

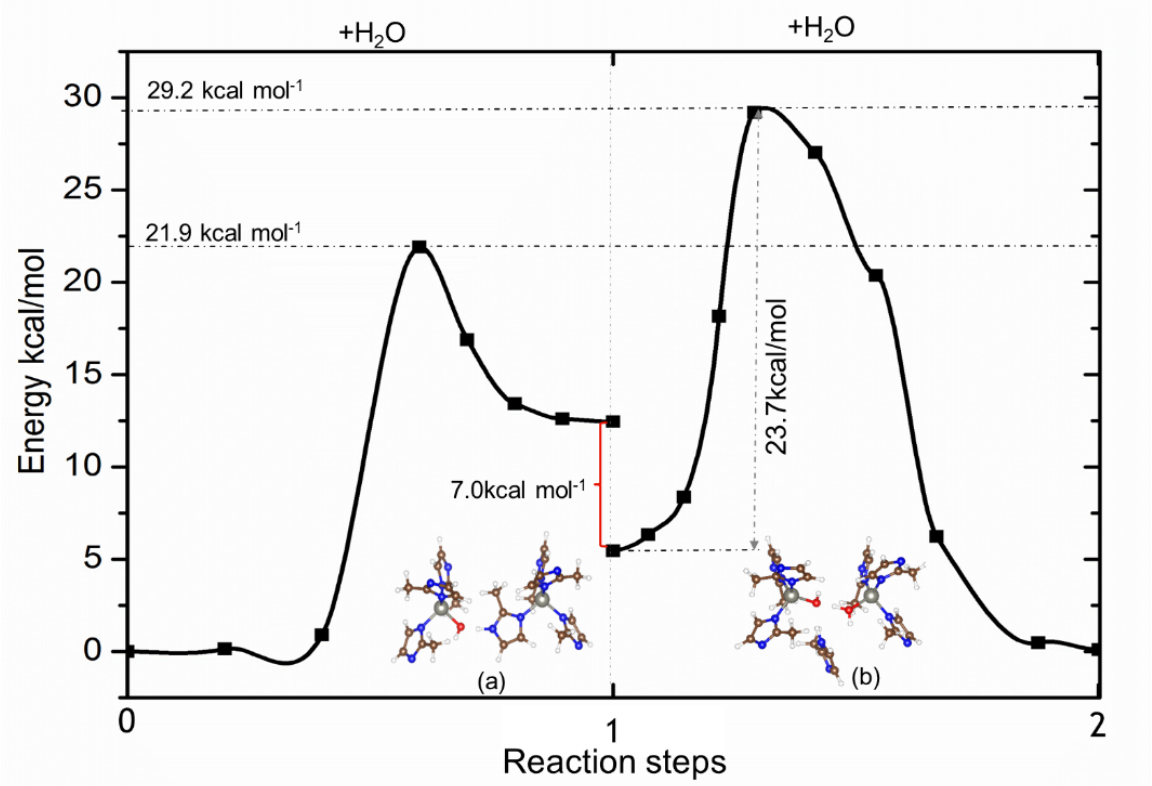

Figure 3.3 Minimum energy reaction pathways for the linker vacancy formation via reaction with water (reaction (i) of Table 3.1). The reaction proceeds via two steps, first forming a dangling linker (1), and subsequently a linker vacancy (2). The energetic discontinuity between the two steps arises from the heat of adsorption of the 2nd water molecule.

3.5 Point Defects at ZIF-8 External Surfaces

The external surface of a porous crystal is the first point of interaction between the crystal and an external fluid, and this interaction becomes more important as the particles are taken from the micro- to nano-scale. This initial interaction can be particularly problematic when the crystals are exposed to environments that potentially degrade the material. Despite its chemical stability, ZIF-8 is known to degrade under acidic conditions, and therefore acidic solutions are typically used to dissolve ZIFs to examine their composition. In fact, this degradation under acidic conditions has been used to etch particular ZIF-8 shapes that were previously synthetically unavailable.[55] In some separation and adsorption applications, ZIF-8 has the potential to come into contact with acid gases such as SO_2 in the feed streams of interest.[56-57] Since the external surface is the first to interact with the material, the external surfaces are likely to degrade first.[21] Thus, understanding the overall stability of the crystal begins with understanding the stability and degradation behavior of the external surface. Here we use the point defect models to study the degradation of ZIF-8 external surfaces, which have different structures from bulk ZIF-8, upon exposure to aqueous SO_2.

3.5.1 ZIF-8 Surface Models

ZIF-8 {100} and {110} surfaces are generated by cleaving Zn-N bonds crossing the same planes in [100] and [110] directions, respectively. As a result, the surfaces can be Zn-terminated or N-terminated. Four candidate {100} surfaces and six candidate {110} surfaces were generated (Figure A.5). The {100} surface uses a tetragonal cell with a base defined by a_0[001] and a_0[010] and an inter-layer spacing (distance in crystal direction

between two adjacent Zn atoms) of $a_0/4$. The {110} surface uses a tetragonal cell with a base defined by $a_0[100]$ and $a_0[01\bar{1}]$ and an inter-layer spacing of $a_0/4\sqrt{2}$ or $a_0/2\sqrt{2}$. In both cases, a_0 is the equilibrium lattice constant of ZIF-8.

An asymmetric model is adopted because of the large size of ZIF-8 slabs, of which one example for a {100} surface slab model is shown in Figure 3.4. The surface energy is examined to simulate the most stable surface facets. The surface energy, E_S, of the slab is defined as

$$E_s = \frac{1}{A}(E_{slab}(n) - n \cdot E_{bulk}), \tag{3.2}$$

where A is the area of surface, $E_{slab}(n)$ is the energy of a slab containing n $Zn(mIM)_2$ units, and E_{bulk} is the energy of one $Zn(mIM)_2$ unit in the bulk material. A lower surface energy denotes a more thermodynamically favorable surface termination. To check for energy convergence as a function of slab size, the surface energy of a set of asymmetric slabs with size ranging from 2 to 4 Zn-layers have been calculated and the energy appears to converge for a slab with 3 layers, one of which is fixed. Thus, a 4-layer slab in which the 2 bottom layers of atoms are fixed at their bulk positions and the 2 top layers of atoms are allowed to relax is chosen to mimic the surface (Figure 3.4). Dipole moment corrections are applied to all slab calculations to eliminate the dipole interaction between periodic images. Slabs are separated from their periodic images by a vacuum region of at least 20 Å. All {100} and {110} surface slab models in this work contain the same number of atoms and species distribution as in a single ZIF-8 unit cell.

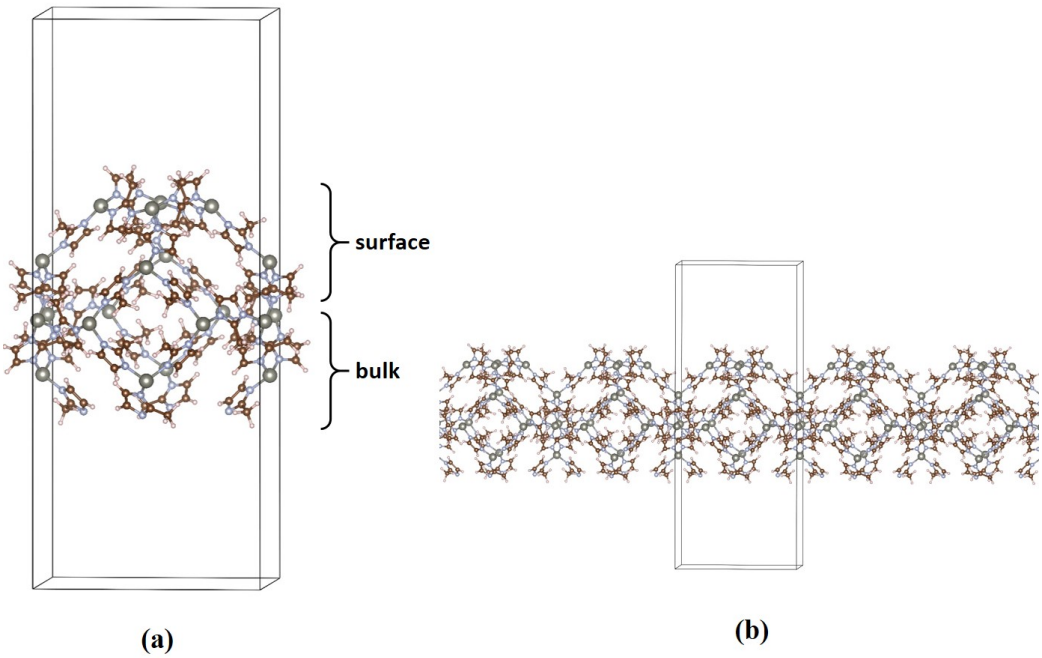

Figure 3.4 Example of (a) a simulation box for the slab calculations and (b) the embedding within the periodic boundary conditions. The bottom 2 layers were fixed in the bulk-optimized positions and the top 2 layers were allowed to relax to simulate the surface.

Here we use the Zn-terminated surfaces with the lowest surface energy as our pure surface models. To stabilize the unsaturated Zn sites on the external layer of the surfaces, we coordinate water molecules to these Zn atoms to ensure all Zn atoms in a slab are 4-coordinated (Figures A.6 and A.7) because unsaturated Zn atoms have stronger attraction to molecules such as H_2O and H_2SO_3 than methylimidazole. Based on the total energy of the hydrated slabs, we find that the coordinated water molecules do not change the relative stability of all the surface terminations.

DFT calculations were performed by VASP[42-45] with the PAW method,[41] the PBE exchange-correlation functional,[58] and semi-empirical dispersion corrections via the DFT-D2 method.[59] The computational ZIF-8 bulk unit cell was a cubic cell from experimental crystallographic data.[36] All calculations were performed using a plane-wave energy cutoff

of 600 eV, sampling k-space at the Γ-point with total energy and ionic force convergence criteria for energy minimization of 10^{-5} eV and 0.03 eV/Å, respectively. These calculations gave a DFT-optimized lattice constant of 16.973 Å, in good agreement with experiment (16.991 Å).[36]

3.5.2 Reactions with Water/Sulfurous Acid on ZIF-8 External Surfaces

Zn atoms of ZIF-8 surfaces are undercoordinated by imidazolate ligands, thus, they are potentially form bonds with water or sulfurous acid, a possible product of reactions between water and SO_2. The coordinated water or sulfurous acid may further react with ZIF-8 surface structures, creating dangling linkers. As Figure 3.5 shows, a H_2O (H_2SO_3) molecule is initially chemisorbed on an unsaturated Zn atom; after the reaction, a proton of the reacting molecule transfers to an imidazolate linker that is bound to the same Zn atom. As a result, the linkage between the metal and ligand is broken. Though Zn is likely removed from the surface as well, the XPS results (Appendix A) suggest that imidazole is preferentially removed and so only the imidazole removal reactions are investigated here. These proposed reactions are in agreement with those calculated for point defects in the bulk structure of ZIF-8.

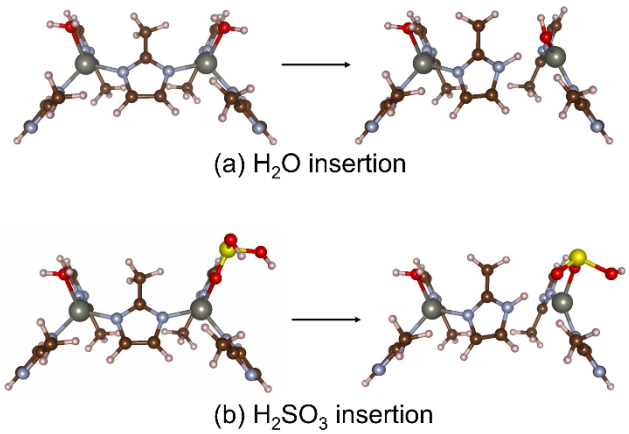

Figure 3.5 Proposed molecular insertion reactions involving (a) H_2O or (b) H_2SO_3 on a hydrated ZIF-8 surface. The insertion reaction involves the same species on both the {110} and {100} surfaces and so the rest of the surface has been omitted for clarity. Colors: gray = Zn, blue = N, red = O, white = H, brown = C, yellow = S.

3.5.3 Comparison of Computational and Experimental Results

It has been demonstrated that ZIF-8 synthesis conditions can be varied to expose different facets.[40,60] Our collaborators' experiments[61] showed that when synthesized solvothermally in methanol using sodium formate as a modulating ligand, ZIF-8 had the particle shape of rhombic dodecahedra, which were composed of 12 {110} facets with sharp corners and edges. ZIF-8 cubes, which were composed of 6 {100} facets, however, could be synthesized hydrothermally using CTAB as a surface-specific capping ligand.

By comparing the surface energy of all possible surface terminations (Table A.6), we have found that all the four possible {100} surface terminations are approximately equally stable, and two of the six possible {110} surface terminations are much more stable than the other terminations. The lowest energy {110} surface was found to have a surface energy of 0.43 J/m^2, which was lower than the typical {100} surface energy of 0.72 J/m^2,

in agreement with experimental observations that the {110} surface is thermodynamically preferred compared to {100}.

Acid stability was examined experimentally by exposing ZIF-8 particles to aqueous solutions of SO_2 at varying concentrations. Concentrations were chosen to simulate various vapor phase concentrations of SO_2 in equilibrium with the aqueous solution, according to Henry's law ($k°_H$ = 1.25 mol/(L·bar)). By terminating growth before reaching thermodynamic equilibrium, truncated rhombic dodecahedra that expose both {110} and {100} facets can be grown, as shown in Figure 3.6. After exposure to aqueous SO_2, the {110} facets appeared to degrade and reveal striations that could be identified as small terraces of {100} facet, whereas the {100} facet appeared to be relatively unaffected by the degradation conditions. Aqueous SO_2 exposure experiments were also conducted on ZIF-8 rhombic dodecahedra and cubes, which exposed only {110} and {100} facets, respectively, for comparison of the chemical stability of these two surfaces (Figure A.8). For both sets of particles shown in Figure A.8, degradation was evident at the low-coordination corners and edges. For the rhombic dodecahedra, degradation was similar to that observed for the large particles, with significant etching on the small {211} and {111} facets present at the corners and edges. The terraces also appeared roughened compared to the as-synthesized particles, particularly at long exposure times. In contrast, the cubes appeared to undergo an initial roughening on the edges, but then did not exhibit further degradation with increased time. This initial degradation is likely due to the fact that the cubes are more accurately described as "truncated cubes," which expose a small amount of {110} facet at low-coordination sites on the edges.

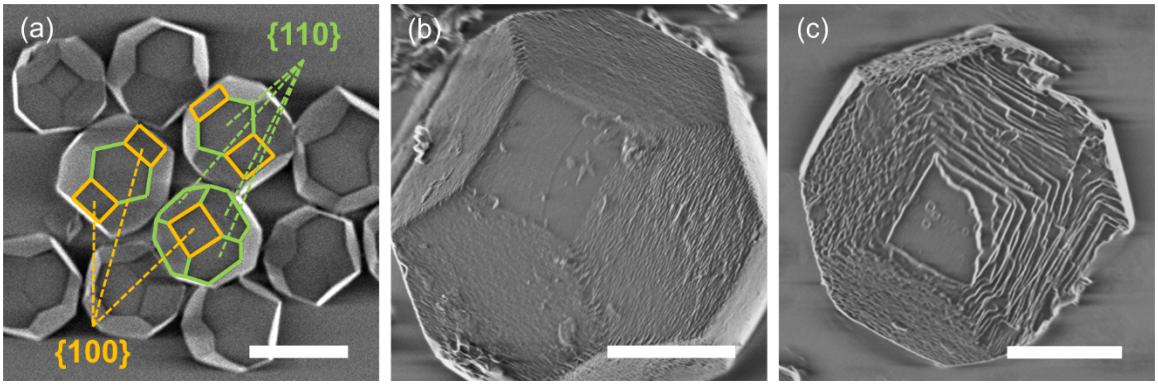

Figure 3.6 SEM images of ZIF-8 truncated rhombic dodecahedra (a) before and after exposure to 1.8 mmol/L SO_2 at 25 °C for (b) 2 days and (c) 4 days show degradation on the {110} facets, revealing terraces of {100} facet. Scale bars: (a) 5 μm, (b, c) 2 μm.

Reaction energies were calculated for the insertion of water or H_2SO_3 into a Zn-N bond on the hydrated {110} or {100} surfaces (Figure 3.5). The reaction energy was calculated as the difference between the total energy of the molecule-inserted structure and that of the molecule-surface complex structure. Insertion of water alone is thermodynamically unfavorable on both surfaces, with reaction energies of 3.8 and 10 kcal/mol on the {110} and {100} surfaces, respectively. This is in agreement with the experimental observations that deionized water does not degrade the surface to an appreciable extent.[61] When a H_2SO_3 molecule is inserted into the Zn-N bond, reactions on both surfaces become thermodynamically favorable with reaction energies of -10.5 and -5.7 kcal/mol on the {110} and {100} surfaces, respectively. These reaction energies suggest that both surfaces can be degraded by H_2SO_3, qualitatively in agreement with XPS and FTIR studies, which showed that after exposure to aqueous SO_2, the O 1s spectra in XPS showed an increase in the oxygen content in the surface region, suggesting that the oxygen content in the surface is more similar to a $Zn(OH)_2$-like species (Figure A.9); FTIR

spectra showed a significant increase in intensity around 3400-3500 cm^{-1}, associated with O-H stretching, and an increase in the band at 900 cm^{-1} associated with S-O stretching (Figure A.10). More details about the XPS and FTIR results are in Appendix A. Additionally, reactions with both water and H_2SO_3 are more favorable on the {110} surface, in agreement with experimental observations that {110} is more easily degraded than {100}. Without calculation of the activation barriers for each of these processes, it is difficult to conclusively state the relative extent of degradation that would be expected on each surface at room temperature. However, based on the reaction energy trend, it is expected that the barrier would be lower for the {110} surface. More investigations on ZIF-8 external surfaces reacting with acid gases will be discussed in Chapter 4.

3.6 Point Defects Formed During Degradation of MIL-125 in Acidic Conditions

MIL-125 is a highly porous titanium-based MOF,[62] which is composed of cyclic octamers $Ti_8O_8(OH)_4$ connected to 12 other cyclic octamers through 1,4-benzene dicarboxylates (BDC), as Figure 3.7a shows. The structure of amine-functionalized MIL-125, MIL-125-NH_2, is shown in Figure 3.7b. MIL-125 and MIL-125-NH_2 have displayed promising H_2S adsorption and stability in H_2S environments.[63] MIL-125 has been found to degrade upon exposure to humid acid gases.[64] However, the addition of the amine functionality has shown to greatly improve the stability of MIL-125 in the presence of water vapor[65-67] and will allow for the investigation into the effect of ligand functionalization on acid gas stability and degradation mechanism. In this section, MIL-

125 and MIL-125-NH_2 are studied in dry, humid, and aqueous SO_2 environments to gain insight into degradation mechanisms during acid gas exposure.

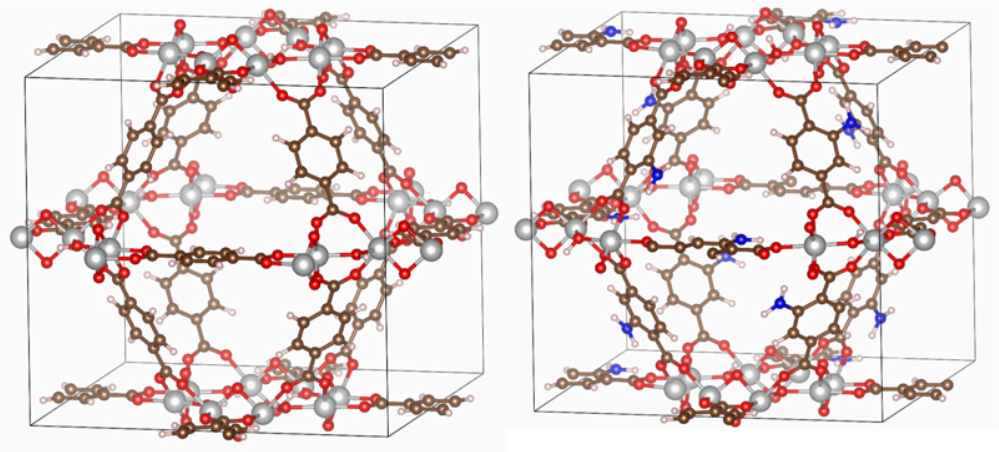

(a) (b)

Figure 3.7 Unit cells of (a) MIL-125 and (b) MIL-125-NH_2. Ti, O, C, H, and N are represented by grey, red, brown, white, and blue balls, respectively.

3.6.1 Experimental Observations

Pure component SO_2 and water adsorption isotherms were collected for both MIL-125 and MIL-125-NH_2, with pre- and post-adsorption characterization to assess the stability of the materials in the presence of theses individual adsorbates. N_2 physisorption after SO_2 adsorption revealed minimal change in surface area for MIL-125 and a 10% decrease for MIL-125-NH_2, suggesting both MOFs are stable in the presence of SO_2 and minimal degradation occurs due to the presence of the dry acid gas. Furthermore, similar to the observation after SO_2 adsorption, no change in the PXRD pattern was observed for either material after water exposure.

The textural properties of the materials were studied after exposure to SO_2 in aqueous or humid environments. Figure 3.8a shows the BET surface area for MIL-125 and MIL-125-NH_2 after exposure to SO_2 in either aqueous (AQ) or humid (H) environments. MIL-125 displayed little change in surface area in an aqueous environment until after 20 ppm-h of exposure, where a complete loss of surface area (>95%) was observed. For all subsequent times after this point, a complete loss of surface area was also observed. The surface area loss is correlated directly with a disappearance of the PXRD pattern after 20 ppm-h of exposure, with the pattern retained before this time, as shown in Figure 3.8b. However, MIL-125-NH_2 displays complete stability throughout aqueous exposure, with little change in surface area or PXRD pattern after exposure. The SEM images (Figures A.11 and A.12) showed that after humid SO_2 exposure, cavities were observed in MIL-125 particles after 1.25 ppm-h of exposure, while no visual change in MIL-125-NH_2 particles.

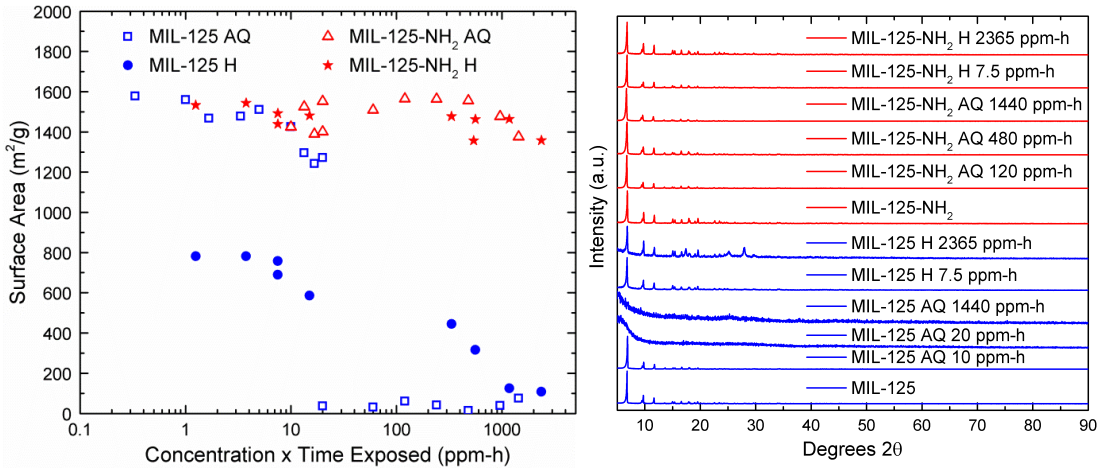

(a) (b)

Figure 3.8 (a) BET surface areas for MIL-125 and MIL-125-NH_2 samples plotted against concentration × time exposed in ppm-h for aqueous (AQ) or humid (H) SO_2 exposure. (b) PXRD patterns for selected MIL-125 and MIL-125-NH_2 samples after timed exposure to aqueous (AQ) or humid (H) SO_2 environment. All patterns are normalized to the most intense peak.

3.6.2 Hypothetical Reaction Mechanisms

Similar to the degradation process in ZIF-8, which presumably starts with the break of Zn-N bonds to form dangling linkers, here we propose three reactions to form dangling BDC linkers in MIL-125(-NH_2) by breaking Ti-O bonds by water and/or acid gases. Since MIL-125 was stable in dry SO_2, but significantly degraded in humid or aqueous SO_2, it is reasonable to propose that MIL-125 was degraded by the products of water and SO_2, of which H_2SO_3 is a species that potentially exists in aqueous phase.[68] To break the linkage between a BDC linker and a titanium octamer, two Ti-O bonds on the same carboxylate of a BDC linker are broken by water and/or H_2SO_3. As Figure 3.9 shows, three reactions are proposed based on different reactant molecules. In all the reactions, the two Ti-O bonds are broken with one of the oxygen atoms protonated, forming a carboxyl group; the conjugate base of the proton-donating molecule bonds to a Ti atom and a charge-neutral molecule (water here) bonds to another Ti atom. When a H_2SO_3 molecule attack a BDC linker, it may form a bridged bisulfite with each of its two oxygen anions forming a bond with a Ti atom. The same reactions were also applied to MIL-125-NH_2 as the local structures between BDC-NH_2 linkers and titanium octamers are identical to that in MIL-125. The relative acidic stability of the two MOFs can be interpreted by comparing the formation energy of the same defects.

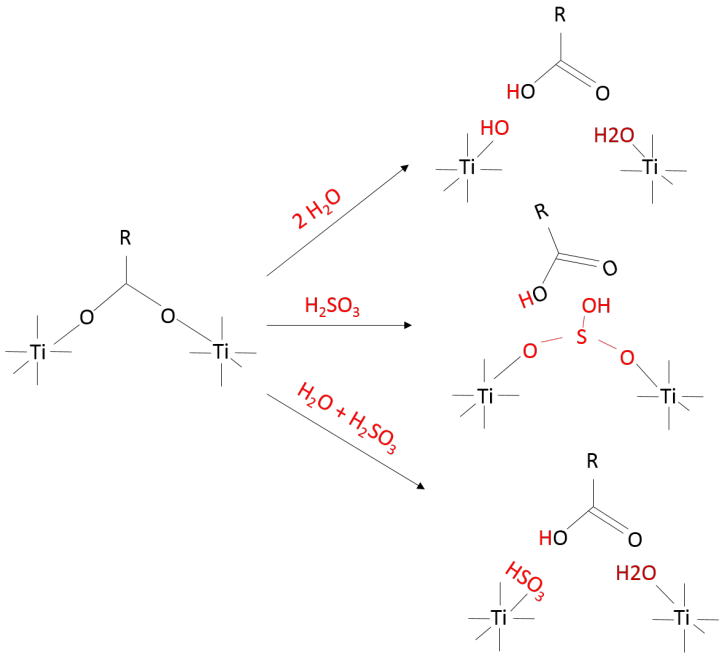

Figure 3.9 Three proposed degradation reactions involving the dissociation of water, sulfurous acid, and sulfurous acid and water with their products shown by the top, middle, and bottom structures on the right-hand side, respectively.

3.6.3 Comparison of Computational and Experimental Results

A periodic model of MIL-125 was constructed from the X-ray diffraction (XRD) crystal structure[62] as the initial crystal geometry and optimized by DFT calculations. The DFT calculations were performed using VASP[42-45] with PAW method[41] and a plane-wave energy cutoff of 600 eV. All calculations were performed using the PBE exchange-correlation functional[69] and semi-empirical dispersion correlations by the DFT-D2 method,[59] sampling k-space at the Γ-point with total energy and ionic force convergence criteria for energy minimization of 10^{-4} eV and 0.03 eV/Å, respectively.

The DFT-optimized MIL-125 lattice constants (a=b=18.984 Å and c=18.092 Å) were in good agreement with experimental values (a=b=18.654 Å and c=18.144 Å).[62] The lattice constants were then fixed during the structural optimizations for MIL-125 with one

or two water or H_2SO_3 molecules per unit cell. The geometry of MIL-125-NH_2 was obtained by adding a NH_2 group to each BDC ligand and optimizing by the same method as that applied to MIL-125.

The two mechanisms involving water (Figure 3.10a), and sulfurous acid and water (Figure 3.10c) are the most favorable, with formation energies of -27.9 and -29.5 kcal/mol, respectively. For the same reaction mechanism, MIL-125-NH_2 displays higher formation energies of -12.5 and -11.5 kcal/mol, respectively, supporting the experimental observation that the addition of the amine functional group has resulted in a higher degree of stability. The reaction involving solely SO_2 was found to be unfavorable in both MOF structures, an observation that supports the stability of the frameworks in a dry SO_2 environment.

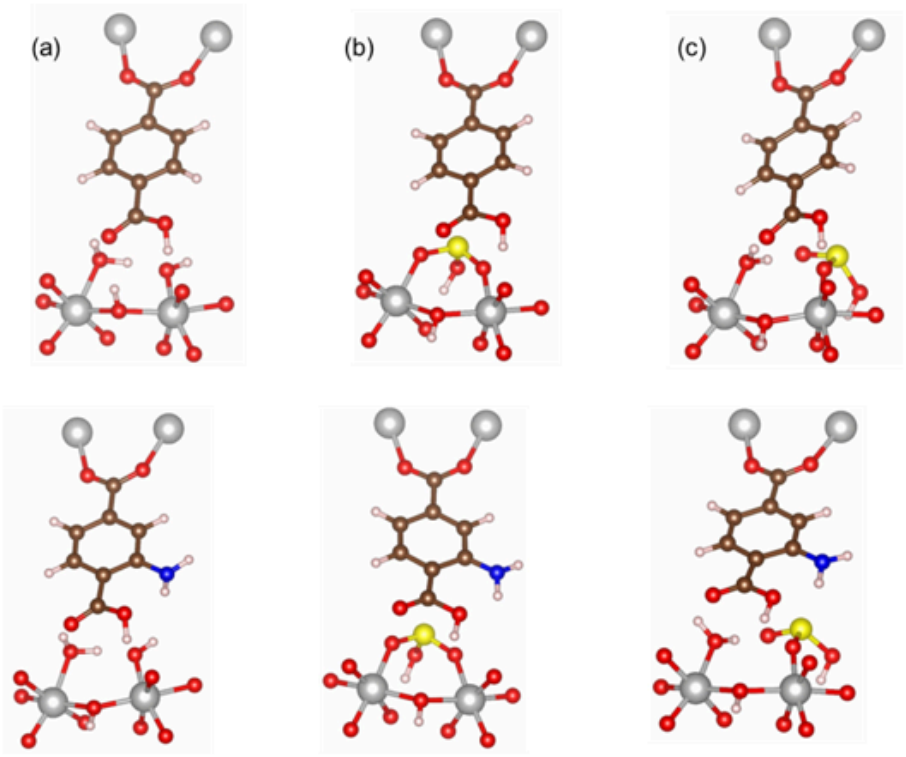

Figure 3.10 DFT optimized geometries of dangling BDC ligands, which are formed by breaking 2 Ti-O bonds with (a) 2 water molecules, (b) a H_2SO_3 molecule, or (c) a water and a H_2SO_3 molecule, in MIL-125 (top) and MIL-125-NH_2 (bottom). Ti, O, C, H, and N are represented by grey, red, brown, white, and blue spheres, respectively.

The calculated formation energies of defects in MIL-125-NH_2 provide only partial insight into the complex nature of degradation. Therefore, reaction energy barriers were calculated to give a more complete understanding of the favorability of potential reactions and stability of the frameworks in acid gas conditions. Reaction energy barriers for the reaction involving solely water in MIL-125 and MIL-125-NH_2 are 1.05 eV and 1.26 eV, respectively, as depicted in Figure 3.11. Note that the energy difference between initial and final images on the pathway (-0.26 eV and 0.03 eV for MIL-125 and MIL-125-NH_2, respectively) is higher than the formation energy (-1.21 eV and -0.54 eV for MIL-125 and MIL-125-NH_2, respectively) because the reactant molecules are initially adsorbed by the framework in the calculations of pathways, while the formation energies are calculated using non-interacting molecules and frameworks. The adsorption energy of a water molecule in the MIL-125 framework is in the range of 0.4 to 0.8 eV varying between the adsorption sites, thus two adsorbed water molecules in the framework result in a lower initial energy (lowered by ~ 1 eV). It is reasonable to expect that the activation energy barrier is related to the formation energy, and a higher formation energy is directly correlated to a higher energy barrier. Therefore, we predict that the barrier for the mechanism involving solely water is higher than the other favorable mechanisms without calculating the energy barriers as the reactions involving solely water have higher formation energies. This hypothesis is supported by the experimental observation that the combination of SO_2 and water is needed to effect a change in the structure. Furthermore, the energy barrier for MIL-125-NH_2 is higher than the barrier for the identical reaction occurring in MIL-125, giving insight into one potential source of the stability of the functionalized framework. Another possible reason for the higher stability for MIL-125-

NH_2 over MIL-125 is that the adsorption of SO_2 by amine reduces the number of acidic species available for degradation, which has been evidenced by the S 2p spectra of MIL-125-NH_2 after exposure to humid SO_2 that is indicative of bound sulfur. However, this type of sulfur spectra was not detected in XPS for MIL-125.[64]

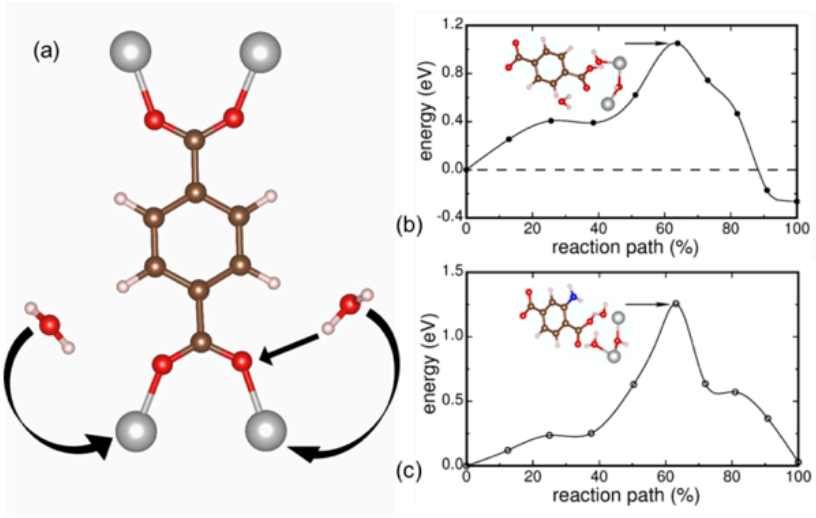

Figure 3.11 (a) Reaction pathway (in the directions of arrows) of two water molecules simultaneously breaking two Ti-O bonds in MIL-125 frameworks, in which one water molecule dissociates into a proton, which is bound to the oxygen atom of a BDC ligand, and a hydroxyl group, which is bound to a Ti atom, and the other water molecule moves towards another Ti atom and finally coordinates with it; (b) Energy barrier (1.05 eV) for (a) in MIL-125; (c) Energy barrier (1.26 eV) for (a) in MIL-125-NH_2. The transition state structures are shown in the insets in (b) and (c).

It is important to note that reactions involving the formation of sulfuric acid and sulfuric-sulfurous acid complexes occur readily in the humid experiments and that the formation of sulfurous acid in the gas phase is thermodynamically unfavorable under the exposure conditions.[70-71] A hypothesized route for the formation of sulfurous acid in the humid experiments is the dissolution in and reaction of SO_2 with a water film formed in the pores of MIL-125. The formation of this water film is supported by the high

hydrophilicity of the framework[66-67] and complete saturation at the conditions of these experiments. Other routes have been explored for a hydrophobic material, ZIF-8, in a separate study.[68] The reaction of sulfuric acid with the framework likely represents a more favorable degradation pathway than that with sulfurous acid. Therefore, the above results for sulfurous acid support the favorability of framework degradation by sulfuric acid in the humid experiments, as well as give insight into potential degradation occurring through the formation of sulfurous acid in a water film within the material.

To further study the degraded structures we proposed, we simulated their IR spectra using cluster models. The cluster models for the calculations of vibrational frequencies were constructed by cutting the appropriate fragments from the periodic structures. To examine our proposed degraded structures with sulfur species, we used charge neutral clusters $Ti_8O_8(OH)_4(COOH)_{12}$ to represent perfect MIL-125, $Ti_8O_8(OH)_4(COOH)_{11}(HSO_3)$ defective MIL-125 with a bridged bisulfite ion, and $Ti_8O_8(OH)_4(COOH)_{11}(H_2O)(HSO_3)$ defective MIL-125 with a coordinated water molecule and a bisulfite ion, respectively (Figure 3.12). In cluster models, we did not include BDC ligands, which exist in perfect and all the proposed defective MIL-125 structures, because they would not result in the difference in the calculated vibrational modes over all kinds of MIL-125 structures. The geometries of the clusters were optimized with the protons of the terminated COOH groups fixed, and then the optimized structures were used to calculate the vibrational frequencies. To examine the new IR peaks brought by the sulfur species, for the defective MIL-125 clusters shown in Figure 3.12, we relax the atoms of local fragments, which have two neighbor Ti atoms, the O atoms bound to the two Ti atoms, the bridging OH group between the two Ti atoms, the HSO_3 group, and the water molecule for the analysis of vibrational

modes. For comparison, we relax the similar atoms in the perfect MIL-125 cluster structure, in which a COOH group between the two Ti atoms was also allowed to relax. All the calculations were performed by Gaussian09 package with B3LYP functional and 6-31G(d,p) basis set.[72] The calculated vibrational modes were scaled by a factor of 0.9611 to be better compared with experimental IR spectra.[73]

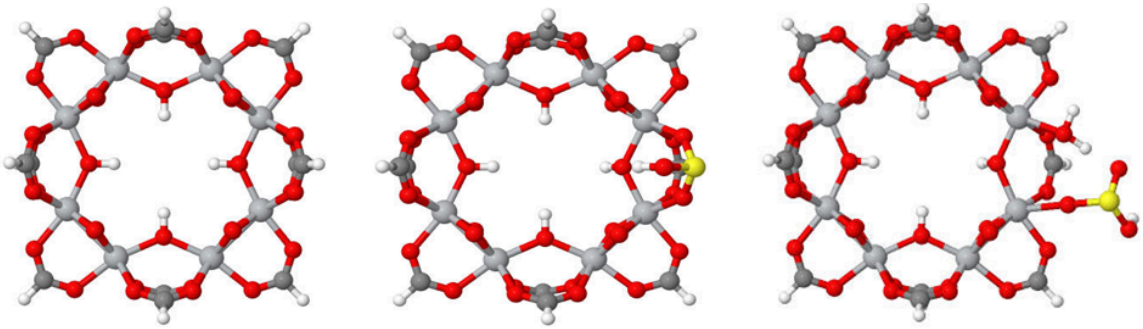

Figure 3.12 Cluster models of perfect (left) and defective MIL-125 with sulfite ions (middle and right) for vibrational frequency calculations.

In situ IR experiments with 260 ppm SO_2 and trace amounts of water were performed to further investigate these reaction mechanisms and correlate with simulated IR spectra of proposed adsorbed species shown in Figure 3.10. The IR spectra during SO_2 adsorption at room temperature as a function of time for MIL-125 and MIL-125-NH_2 and simulated spectra for H_2SO_3 and H_2SO_3+H_2O adsorbed species are shown in Figure 3.13. The formation of bridged bisulfites over MIL-125 (Figure 3.10b), indicated by the characteristic peaks of asymmetric S-O stretching at 988 cm^{-1},[74] likely occurs at the metal oxide cluster between two titanium atoms. In addition, the formation of monodentate bisulfite over MIL-125 at the metal oxide cluster with a compensating water molecule, the species hypothesized stretching at 904, 953, and 1037 cm^{-1} and symmetric S-O in Figure 3.10c, is indicated by the characteristic peaks at 1071 and 1143 cm^{-1} of S=O stretching and

(S-)O-H bending, respectively.[74] These observed species are quite similar to those observed in the simulated spectra for the species associated with the reactions from Figure 3.10b,c, as shown in Figure 3.13c and tabulated in Table A.7.

The simulated spectra show characteristic peaks for asymmetric S-O stretching at 894, 956, and 1010 cm^{-1}, symmetric S-O stretching at 975 cm^{-1}, S=O stretching at 1054 cm^{-1}, (S-)O-H bending at 1102 and 1139 cm^{-1}, and O-H stretching of the bisulfite species at 3472 cm^{-1}. The presence of these species over MIL-125 supports the favorability of these reactions, as indicated by the simulation results discussed in the previous section. Furthermore, as in our collaborator's previous study,[75] a peak at 1708 cm^{-1}, indicative of the carbonyl group on the carboxylic acid ligand, increased simultaneously with an increase in the hydroxyl stretching region (3700-3200 cm^{-1}) over the time of exposure, as ligands were displaced by reaction of the bisulfite ion and free water was adsorbed within the framework. An increase in adsorbed surface water generated from the reaction of SO_2 with surface hydroxyls or adsorption of free water in the system is observed by an increase in the peak at 1628 cm^{-1}, assigned to H-O-H bending.[75-76] The several peaks in the hydroxyl stretching region that increased during adsorption may also be attributed to adsorbed surface water, O-H stretching of the bisulfite ion, hydroxyl groups formed from the dissociation of water, or compensating water adsorbed after reaction of the bisulfite ion with the opposing titanium atom.

The amine-functionalized material displays similar sulfur-based species during SO_2 adsorption, with peaks characteristic of asymmetric S-O stretching at 902, 953, and 1030 cm^{-1}. However, the peak characteristic of symmetric S-O stretching was absent from the spectra, likely hidden by the level of noise of the measurement. Monodentate bisulfite

species similar to those formed over MIL-125 were also observed with characteristic peaks at 1138 and 1087 cm^{-1} of (S-)O-H bending and S=O stretching, respectively. The presence of these species aligns with two of the proposed reaction schemes, and a slight peak in the carbonyl stretch region was observed at 1700 cm^{-1}. No other signs of degradation were observed for MIL-125-NH_2 in the aqueous and humid SO_2 environments through other characterization techniques, and it is likely that any degradation occurring was associated with the displacement of surface ligands, with little to no degradation occurring within the bulk structure.

Two peaks are observed at 3288 and 3445 cm^{-1} in the MIL-125-NH_2 spectra that are absent from the unfunctionalized MIL-125 spectra. These peaks result from a perturbation of the symmetric and asymmetric N-H stretch due to interaction with adsorbed sulfur species similar to the effect observed for MIL-125-NH_2 after H_2S exposure.[63] The perturbation of these peaks suggests the amine functional group offers an additional binding site preventing access and reaction of sulfur species with the framework and likely aids in stabilizing the material in humid SO_2 conditions.

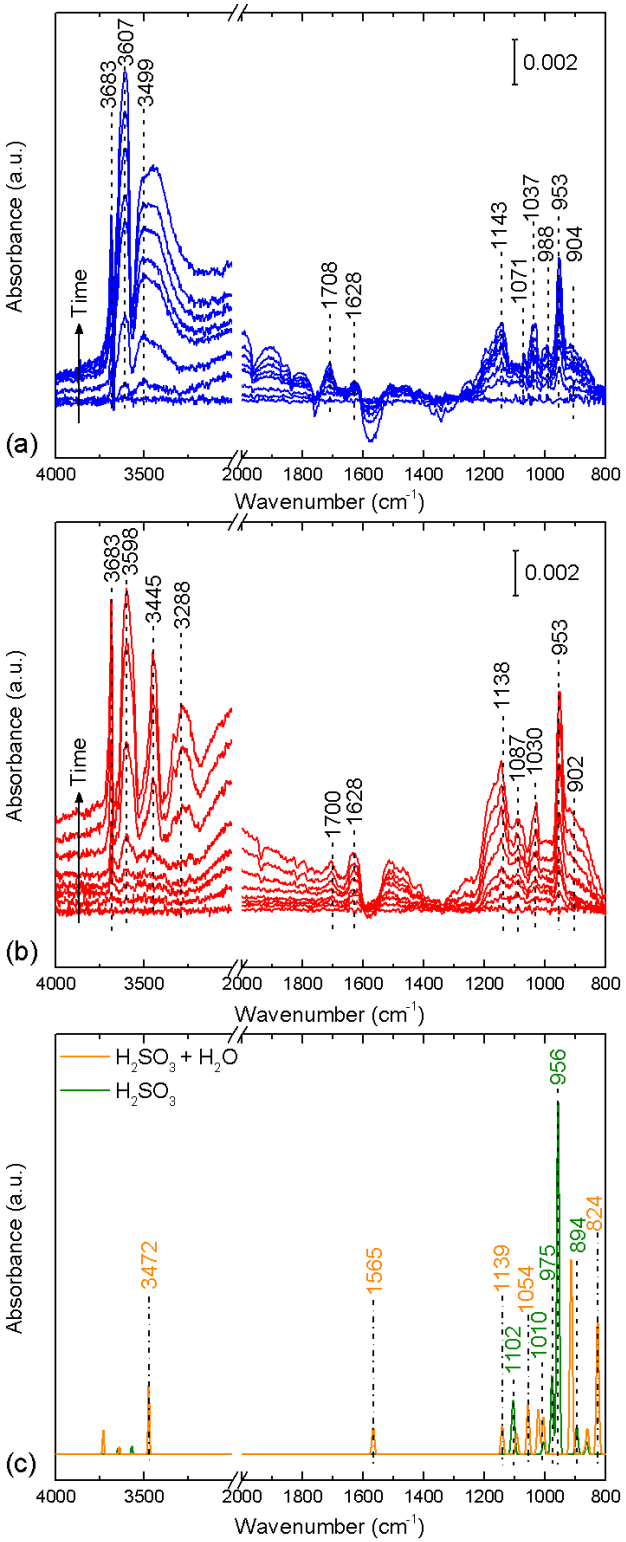

Figure 3.13 IR spectra during 30 min of 260 ppm SO_2 adsorption on (a) MIL-125 and (b) MIL-125-NH_2 at 25 ˚C. (c) Simulated IR spectra for H_2SO_3 + H_2O and H_2SO_3 species adsorbed within MIL-125.

3.7 Summary

In this chapter, we have proposed potential point defects in ZIF-8 based on the known defects existing in zeolites and examined their thermodynamic and kinetic favorability. Although ZIF-8 is chosen as a prototypical model to study point defects, as ZIFs have similar local geometries such as tetrahedrally coordinated metal cations, we expect that our results apply to other ZIFs as well. These results challenge the simplistic interpretation of ZIFs as perfect defect-free crystals. While we did not attempt to estimate absolute equilibrium defect concentrations (due to neglect of entropic effects, which are difficult to quantify, particularly in solution), it is clear that elementary linker and metal vacancy defects are relatively low in energy and that their presence should not be thermodynamically unexpected. However, our results also indicate that kinetic factors are likely to inhibit the introduction of large defect concentrations, at least at room temperature. Yet even very small spontaneous equilibrium defect concentrations may have a potentially outsized impact on the catalytic properties or long-term stability of ZIFs and other MOFs, particularly under "reactive" working conditions where the defect site may be exposed to reactants/solvents, trace contaminants, or acid gases. As such, these results also highlight the importance of considering the presence and impact of such defects when assessing the viability of ZIFs and other "stable" MOFs for targeted applications and should spur experimental studies to characterize MOF defects and their impacts.

Extending from ZIF point defect models, we have also investigated the stability of other MOF systems such as ZIF-8 external surfaces and MIL-125 by evaluating the energetic properties of relevant point defects formed during the degradation of these materials. Our computational results were coupled with experimental observations to gain

insight into the variances in MOF stability and their degradation mechanisms in difference exposure environments.

3.8 References

(1) Zhou, H. C.; Long, J. R.; Yaghi, O. M., Introduction to Metal-Organic Frameworks. *Chem. Rev.* **2012,** *112* (2), 673-674.

(2) Ma, W. J.; Jiang, Q.; Yu, P.; Yang, L. F.; Mao, L. Q., Zeolitic Imidazolate Framework-Based Electrochemical Biosensor for in Vivo Electrochemical Measurements. *Anal. Chem.* **2013,** *85* (15), 7550-7557.

(3) Bae, Y. S.; Lee, C. Y.; Kim, K. C.; Farha, O. K.; Nickias, P.; Hupp, J. T.; Nguyen, S. T.; Snurr, R. Q., High Propene/Propane Selectivity in Isostructural Metal-Organic Frameworks with High Densities of Open Metal Sites. *Angew. Chem., Int. Ed.* **2012,** *51* (8), 1857-1860.

(4) Banerjee, R.; Phan, A.; Wang, B.; Knobler, C.; Furukawa, H.; O'Keeffe, M.; Yaghi, O. M., High-throughput synthesis of zeolitic imidazolate frameworks and application to CO_2 capture. *Science* **2008,** *319* (5865), 939-943.

(5) Zhang, L. L.; Wu, G.; Jiang, J. W., Adsorption and Diffusion of CO_2 and CH_4 in Zeolitic Imidazolate Framework-8: Effect of Structural Flexibility. *J. Phys. Chem. C* **2014,** *118* (17), 8788-8794.

(6) Wang, B.; Cote, A. P.; Furukawa, H.; O'Keeffe, M.; Yaghi, O. M., Colossal cages in zeolitic imidazolate frameworks as selective carbon dioxide reservoirs. *Nature* **2008,** *453* (7192), 207-211.

(7) Wu, H.; Zhou, W.; Yildirim, T., Hydrogen storage in a prototypical zeolitic imidazolate framework-8. *J. Am. Chem. Soc.* **2007,** *129* (17), 5314-5315.

(8) Eum, K.; Jayachandrababu, K. C.; Rashidi, F.; Zhang, K.; Leisen, J.; Graham, S.; Lively, R. P.; Chance, R. R.; Sholl, D. S.; Jones, C. W.; Nair, S., Highly Tunable Molecular Sieving and Adsorption Properties of Mixed-Linker Zeolitic Imidazolate Frameworks. *J. Am. Chem. Soc.* **2015,** *137* (12), 4191-4197.

(9) Basnayake, S. A.; Su, J.; Zou, X. D.; Balkus, K. J., Carbonate-Based Zeolitic Imidazolate Framework for Highly Selective CO_2 Capture. *Inorg. Chem.* **2015,** *54* (4), 1816-1821.

(10) Pimentel, B. R.; Parulkar, A.; Zhou, E. K.; Brunelli, N. A.; Lively, R. P., Zeolitic Imidazolate Frameworks: Next-Generation Materials for Energy-Efficient Gas Separations. *ChemSusChem* **2014,** *7* (12), 3202-3240.

(11) Yao, J. F.; Wang, H. T., Zeolitic imidazolate framework composite membranes and thin films: synthesis and applications. *Chem. Soc. Rev.* **2014,** *43* (13), 4470-4493.

(12) Zhuang, J.; Kuo, C. H.; Chou, L. Y.; Liu, D. Y.; Weerapana, E.; Tsung, C. K., Optimized Metal-Organic-Framework Nanospheres for Drug Delivery: Evaluation of Small-Molecule Encapsulation. *ACS Nano* **2014,** *8* (3), 2812-2819.

(13) Cai, W.; Chu, C. C.; Liu, G.; Wang, Y. X. J., Metal-Organic Framework-Based Nanomedicine Platforms for Drug Delivery and Molecular Imaging. *Small* **2015,** *11* (37), 4806-4822.

(14) Fujita, M.; Kwon, Y. J.; Washizu, S.; Ogura, K., Preparation, Clathration Ability, and Catalysis of a 2-Dimensional Square Network Material Composed of Cadmium(Ii) and 4,4'-Bipyridine. *J. Am. Chem. Soc.* **1994,** *116* (3), 1151-1152.

(15) Chung, Y. G.; Camp, J.; Haranczyk, M.; Sikora, B. J.; Bury, W.; Krungleviciute, V.; Yildirim, T.; Farha, O. K.; Sholl, D. S.; Snurr, R. Q., Computation-Ready, Experimental Metal-Organic Frameworks: A Tool To Enable High-Throughput Screening of Nanoporous Crystals. *Chem. Mater.* **2014,** *26* (21), 6185-6192.

(16) Sokol, A. A.; Catlow, C. R. A.; Garces, J. M.; Kuperman, A., Local states in microporous silica and aluminum silicate materials. 1. Modeling structure, formation, and transformation of common hydrogen containing defects. *J. Phys. Chem. B* **2002,** *106* (24), 6163-6177.

(17) Malola, S.; Svelle, S.; Bleken, F. L.; Swang, O., Detailed Reaction Paths for Zeolite Dealumination and Desilication From Density Functional Calculations. *Angew. Chem., Int. Ed.* **2012,** *51* (3), 652-655.

(18) Fjermestad, T.; Svelle, S.; Swang, O., Mechanism of Si Island Formation in SAPO-34 (vol 119, pg 2086, 2015). *J. Phys. Chem. C* **2015,** *119* (35), 20782-20782.

(19) Fjermestad, T.; Svelle, S.; Swang, O., Desilication of SAPO-34: Reaction Mechanisms from Periodic DFT Calculations. *J. Phys. Chem. C* **2015,** *119* (4), 2073-2085.

(20) Pascale, F.; Ugliengo, P.; Civalleri, B.; Orlando, R.; D'Arco, P.; Dovesi, R., Hydrogarnet defect in chabazite and sodalite zeolites: A periodic Hartree-Fock and B3-LYP study. *J. Chem. Phys.* **2002,** *117* (11), 5337-5346.

(21) Sholl, D. S.; Lively, R. P., Defects in Metal-Organic Frameworks: Challenge or Opportunity? *J. Phys. Chem. Lett.* **2015,** *6* (17), 3437-3444.

(22) Han, C.; Verploegh, R. J.; Sholl, D. S., Assessing the impact of point defects on molecular diffusion in ZIF-8 using molecular simulations. *J. Phys. Chem. Lett.* **2018,** *9*, 4037–4044.

(23) Fang, Z. L.; Bueken, B.; De Vos, D. E.; Fischer, R. A., Defect-Engineered Metal-Organic Frameworks. *Angew. Chem., Int. Ed.* **2015,** *54* (25), 7234-7254.

(24) Furukawa, H.; Muller, U.; Yaghi, O. M., "Heterogeneity within Order" in Metal-Organic Frameworks. *Angew. Chem., Int. Ed.* **2015,** *54* (11), 3417-3430.

(25) Taylor, J. M.; Dekura, S.; Ikeda, R.; Kitagawa, H., Defect Control To Enhance Proton Conductivity in a Metal-Organic Framework. *Chem. Mater.* **2015,** *27* (7), 2286-2289.

(26) Wu, H.; Chua, Y. S.; Krungleviciute, V.; Tyagi, M.; Chen, P.; Yildirim, T.; Zhou, W., Unusual and Highly Tunable Missing-Linker Defects in Zirconium Metal-Organic Framework UiO-66 and Their Important Effects on Gas Adsorption. *J. Am. Chem. Soc.* **2013,** *135* (28), 10525-10532.

(27) Cliffe, M. J.; Hill, J. A.; Murray, C. A.; Coudert, F. X.; Goodwin, A. L., Defect-dependent colossal negative thermal expansion in UiO-66(Hf) metal-organic framework. *Phys. Chem. Chem. Phys.* **2015,** *17* (17), 11586-11592.

(28) Chizallet, C.; Bats, N., External Surface of Zeolite Imidazolate Frameworks Viewed Ab Initio: Multifunctionality at the Organic-Inorganic Interface. *J. Phys. Chem. Lett.* **2010,** *1* (1), 349-353.

(29) Chizallet, C.; Lazare, S.; Bazer-Bachi, D.; Bonnier, F.; Lecocq, V.; Soyer, E.; Quoineaud, A. A.; Bats, N., Catalysis of Transesterification by a Nonfunctionalized Metal-Organic Framework: Acido-Basicity at the External Surface of ZIF-8 Probed by FTIR and ab Initio Calculations. *J. Am. Chem. Soc.* **2010,** *132* (35), 12365-12377.

(30) Canivet, J.; Fateeva, A.; Guo, Y. M.; Coasne, B.; Farrusseng, D., Water adsorption in MOFs: fundamentals and applications. *Chem. Soc. Rev.* **2014,** *43* (16), 5594-5617.

(31) Burtch, N. C.; Jasuja, H.; Walton, K. S., Water Stability and Adsorption in Metal-Organic Frameworks. *Chem. Rev.* **2014,** *114* (20), 10575-10612.

(32) Liang, J.; Su, J.; Wang, Y. X.; Chen, Y. P.; Zou, X. D.; Liao, F. H.; Lin, J. H.; Sun, J. L., A 3D 12-Ring Zeolite with Ordered 4-Ring Vacancies Occupied by $(H2O)_2$ Dimers. *Chem. Eur. J.* **2014,** *20* (49), 16097-16101.

(33) Bai, Z. H.; Fujii, M.; Imakita, K.; Hayashi, S., Strong white photoluminescence from annealed zeolites. *J Lumin* **2014,** *145*, 288-291.

(34) Baerlocher, C.; Xie, D.; McCusker, L. B.; Hwang, S. J.; Chan, I. Y.; Ong, K.; Burton, A. W.; Zones, S. I., Ordered silicon vacancies in the framework structure of the zeolite catalyst SSZ-74. *Nat. Mater.* **2008,** *7* (8), 631-635.

(35) Yu, K.; Kiesling, K.; Schmidt, J. R., Trace Flue Gas Contaminants Poison Coordinatively Unsaturated Metal-Organic Frameworks: Implications for CO_2 Adsorption and Separation. *J. Phys. Chem. C* **2012,** *116* (38), 20480-20488.

(36) Park, K. S.; Ni, Z.; Cote, A. P.; Choi, J. Y.; Huang, R. D.; Uribe-Romo, F. J.; Chae, H. K.; O'Keeffe, M.; Yaghi, O. M., Exceptional chemical and thermal stability of zeolitic imidazolate frameworks. *Proc. Natl. Acad. Sci. U. S. A.* **2006,** *103* (27), 10186-10191.

(37) Fei, H. H.; Cahill, J. F.; Prather, K. A.; Cohen, S. M., Tandem Postsynthetic Metal Ion and Ligand Exchange in Zeolitic Imidazolate Frameworks. *Inorg. Chem.* **2013,** *52* (7), 4011-4016.

(38) Jian, M. P.; Liu, B.; Liu, R. P.; Qu, J. H.; Wang, H. T.; Zhang, X. W., Water-based synthesis of zeolitic imidazolate framework-8 with high morphology level at room temperature. *RSC Adv.* **2015,** *5* (60), 48433-48441.

(39) Shah, M.; Kwon, H. T.; Tran, V.; Sachdeva, S.; Jeong, H. K., One step in situ synthesis of supported zeolitic imidazolate framework ZIF-8 membranes: Role of sodium formate. *Microporous Mesoporous Mater.* **2013,** *165*, 63-69.

(40) Cravillon, J.; Nayuk, R.; Springer, S.; Feldhoff, A.; Huber, K.; Wiebcke, M., Controlling Zeolitic Imidazolate Framework Nano- and Microcrystal Formation: Insight into Crystal Growth by Time-Resolved In Situ Static Light Scattering. *Chem. Mater.* **2011,** *23* (8), 2130-2141.

(41) Blöchl, P. E., Projector Augmented-Wave Method. *Phys. Rev. B* **1994,** *50* (24), 17953-17979.

(42) Kresse, G.; Furthmuller, J., Efficiency of *ab-initio* total energy calculations for metals and semiconductors using a plane-wave basis set. *Comput. Mater. Sci.* **1996,** *6* (1), 15-50.

(43) Kresse, G.; Furthmuller, J., Efficient iterative schemes for *ab initio* total-energy calculations using a plane-wave basis set. *Phys. Rev. B* **1996,** *54* (16), 11169-11186.

(44) Kresse, G.; Hafner, J., *Ab Initio* Molecular Dynamics for Liquid Metals. *Phys. Rev. B* **1993,** *47* (1), 558-561.

(45) Kresse, G.; Hafner, J., *Ab Initio* Molecular-Dynamics Simulation of the Liquid-Metal Amorphous-Semiconductor Transition in Germanium. *Phys. Rev. B* **1994,** *49* (20), 14251-14269.

(46) Kresse, G.; Joubert, D., From ultrasoft pseudopotentials to the projector augmented-wave method. *Phys. Rev. B* **1999,** *59* (3), 1758-1775.

(47) Henkelman, G.; Jonsson, H., Improved tangent estimate in the nudged elastic band method for finding minimum energy paths and saddle points. *J. Chem. Phys.* **2000,** *113* (22), 9978-9985.

(48) Henkelman, G.; Uberuaga, B. P.; Jonsson, H., A climbing image nudged elastic band method for finding saddle points and minimum energy paths. *J. Chem. Phys.* **2000,** *113* (22), 9901-9904.

(49) Marenich, A. V.; Cramer, C. J.; Truhlar, D. G., Universal Solvation Model Based on Solute Electron Density and on a Continuum Model of the Solvent Defined by the Bulk Dielectric Constant and Atomic Surface Tensions. *J. Phys. Chem. B* **2009,** *113* (18), 6378-6396.

(50) Phan, A.; Doonan, C. J.; Uribe-Romo, F. J.; Knobler, C. B.; O'Keeffe, M.; Yaghi, O. M., Synthesis, Structure, and Carbon Dioxide Capture Properties of Zeolitic Imidazolate Frameworks. *Acc. Chem. Res.* **2010,** *43* (1), 58-67.

(51) Deria, P.; Mondloch, J. E.; Karagiaridi, O.; Bury, W.; Hupp, J. T.; Farha, O. K., Beyond post-synthesis modification: evolution of metal-organic frameworks via building block replacement. *Chem. Soc. Rev.* **2014,** *43* (16), 5896-5912.

(52) Karagiaridi, O.; Lalonde, M. B.; Bury, W.; Sarjeant, A. A.; Farha, O. K.; Hupp, J. T., Opening ZIF-8: A Catalytically Active Zeolitic Imidazolate Framework of Sodalite Topology with Unsubstituted Linkers. *J. Am. Chem. Soc.* **2012,** *134* (45), 18790-18796.

(53) Wang, Z. Q.; Cohen, S. M., Postsynthetic modification of metal-organic frameworks. *Chem. Soc. Rev.* **2009,** *38* (5), 1315-1329.

(54) Cheng, P. F.; Hu, Y. H., H_2O-Functionalized Zeolitic Zn(2-methylimidazole)2 Framework (ZIF-8) for H_2 Storage. *J. Phys. Chem. C* **2014,** *118* (38), 21866-21872.

(55) Avci, C.; Arinez-Soriano, J.; Carne-Sanchez, A.; Guillerm, V.; Carbonell, C.; Imaz, I.; Maspoch, D., Post-Synthetic Anisotropic Wet-Chemical Etching of Colloidal Sodalite ZIF Crystals. *Angew. Chem., Int. Ed.* **2015,** *54* (48), 14417-14421.

(56) Lively, R. P.; Dose, M. E.; Xu, L. R.; Vaughn, J. T.; Johnson, J. R.; Thompson, J. A.; Zhang, K.; Lydon, M. E.; Lee, J. S.; Liu, L.; Hu, Z. S.; Karvan, O.; Realff, M. J.; Koros, W. J., A high-flux polyimide hollow fiber membrane to minimize footprint and energy penalty for CO_2 recovery from flue gas. *J. Membr. Sci.* **2012,** *423*, 302-313.

(57) Sun, W. Z.; Lin, L. C.; Peng, X.; Smit, B., Computational screening of porous metal-organic frameworks and zeolites for the removal of SO_2 and NO_x from flue gases. *AIChE J.* **2014,** *60* (6), 2314-2323.

(58) Perdew, J. P.; Burke, K.; Ernzerhof, M., Generalized gradient approximation made simple [Phys. Rev. Lett. 77, 3865 (1996)]. *Phys. Rev. Lett.* **1997,** *78* (7), 1396-1396.

(59) Grimme, S., Semiempirical GGA-type density functional constructed with a long-range dispersion correction. *J. Comput. Chem.* **2006,** *27* (15), 1787-1799.

(60) Lim, I. H.; Schrader, W.; Schuth, F., Insights into the Molecular Assembly of Zeolitic Imidazolate Frameworks by ESI-MS. *Chem. Mater.* **2015,** *27* (8), 3088-3095.

(61) Pang, S. H.; Han, C.; Sholl, D. S.; Jones, C. W.; Lively, R. P., Facet-Specific Stability of ZIF-8 in the Presence of Acid Gases Dissolved in Aqueous Solutions. *Chem. Mater.* **2016,** *28* (19), 6960-6967.

(62) Dan-Hardi, M.; Serre, C.; Frot, T.; Rozes, L.; Maurin, G.; Sanchez, C.; Ferey, G., A New Photoactive Crystalline Highly Porous Titanium(IV) Dicarboxylate. *J. Am. Chem. Soc.* **2009,** *131* (31), 10857-10859.

(63) Vaesen, S.; Guillerm, V.; Yang, Q. Y.; Wiersum, A. D.; Marszalek, B.; Gil, B.; Vimont, A.; Daturi, M.; Devic, T.; Llewellyn, P. L.; Serre, C.; Maurin, G.; De Weireld, G., A robust amino-functionalized titanium(IV) based MOF for improved separation of acid gases. *Chem. Commun.* **2013,** *49* (86), 10082-10084.

(64) Mounfield, W. P.; Han, C.; Pang, S. H.; Tumuluri, U.; Jiao, Y.; Bhattacharyya, S.; Dutzer, M. R.; Nair, S.; Wu, Z.; Lively, R. P.; Sholl, D. S.; Walton, K. S., Synergistic Effects of Water and SO_2 on Degradation of MIL-125 in the Presence of Acid Gases. *J. Phys. Chem. C* **2016,** *120* (48), 27230-27240.

(65) Jeremias, F.; Lozan, V.; Henninger, S. K.; Janiak, C., Programming MOFs for water sorption: amino-functionalized MIL-125 and UiO-66 for heat transformation and heat storage applications. *Dalton Trans.* **2013,** *42* (45), 15967-15973.

(66) Kim, S. N.; Kim, J.; Kim, H. Y.; Cho, H. Y.; Ahn, W. S., Adsorption/catalytic properties of MIL-125 and NH_2-MIL-125. *Catal. Today* **2013,** *204*, 85-93.

(67) Canivet, J.; Bonnefoy, J.; Daniel, C.; Legrand, A.; Coasne, B.; Farrusseng, D., Structure-property relationships of water adsorption in metal-organic frameworks. *New J. Chem.* **2014,** *38* (7), 3102-3111.

(68) Bhattacharyya, S.; Pang, S. H.; Dutzer, M. R.; Lively, R. P.; Walton, K. S.; Sholl, D. S.; Nair, S., Interactions of SO_2-Containing Acid Gases with ZIF-8: Structural Changes and Mechanistic Investigations. *J. Phys. Chem. C* **2016,** *120* (48), 27221-27229.

(69) Perdew, J. P.; Burke, K.; Ernzerhof, M., Generalized gradient approximation made simple. *Phys. Rev. Lett.* **1996,** *77* (18), 3865-3868.

(70) Liu, J. J.; Fang, S.; Liu, W.; Wang, M. Y.; Tao, F. M.; Liu, J. Y., Mechanism of the Gaseous Hydrolysis Reaction of SO_2: Effects of NH_3 versus H_2O. *J. Phys. Chem. A* **2015,** *119* (1), 102-111.

(71) Liu, J. J.; Fang, S.; Wang, Z. X.; Yi, W. C.; Tao, F. M.; Liu, J. Y., Hydrolysis of Sulfur Dioxide in Small Clusters of Sulfuric Acid: Mechanistic and Kinetic Study. *Environ. Sci. Technol.* **2015,** *49* (22), 13112-13120.

(72) Frisch, M. J. T., G. W.; Schlegel, H. B.; Scuseria, G. E.; Robb, M. A.; Cheeseman, J. R.; Montgomery, J. A., Jr.; Vreven, T.; Kudin, K. N.; Burant, J. C.; Millam, J. M.; Iyengar, S. S.; Tomasi, J.; Barone, V.; Mennucci, B.; Cossi, M.; Scalmani, G.; Rega, N.; Petersson, G. A.; Nakatsuji, H.; Hada, M.; Ehara, M.; Toyota, K.; Fukuda, R.; Hasegawa, J.; Ishida, M.; Nakajima, T.; Honda, Y.; Kitao, O.; Nakai, H.; Klene, M.; Li, X.; Knox, J. E.; Hratchian, H. P.; Cross, J. B.; Bakken, V.; Adamo, C.; Jaramillo, J.; Gomperts, R.; Stratmann, R. E.; Yazyev, O.; Austin, A. J.; Cammi, R.; Pomelli, C.; Ochterski, J. W.; Ayala, P. Y.; Morokuma, K.; Voth, G. A.; Salvador, P.; Dannenberg, J. J.; Zakrzewski, V. G.; Dapprich, S.; Daniels, A. D.; Strain, M. C.; Farkas, O.; Malick, D. K.; Rabuck, A. D.; Raghavachari, K.; Foresman, J. B.; Ortiz, J. V.; Cui, Q.; Baboul, A. G.; Clifford, S.; Cioslowski, J.; Stefanov, B. B.; Liu, G.; Liashenko, A.; Piskorz, P.; Komaromi, I.; Martin, R. L.; Fox, D. J.; Keith, T.; Al-Laham, M. A.; Peng, C. Y.; Nanayakkara, A.; Challacombe, M.; Gill, P. M. W.; Johnson, B.; Chen, W.; Wong, M. W.; Gonzalez, C.; Pople, J. A. , *Gaussian Revision E.01*. Gaussian, Inc.: Wallingford, CT, 2004.

(73) Irikura, K. K.; Johnson, R. D.; Kacker, R. N., Uncertainties in scaling factors for *ab initio* vibrational frequencies. *J. Phys. Chem. A* **2005,** *109* (37), 8430-8437.

(74) Nanayakkara, C. E.; Pettibone, J.; Grassian, V. H., Sulfur dioxide adsorption and photooxidation on isotopically-labeled titanium dioxide nanoparticle surfaces: roles of surface hydroxyl groups and adsorbed water in the formation and stability of adsorbed sulfite and sulfate. *Phys. Chem. Chem. Phys.* **2012,** *14* (19), 6957-6966.

(75) Mounfield, W. P.; Tumuluri, U.; Jiao, Y.; Li, M. J.; Dai, S.; Wu, Z. L.; Walton, K. S., Role of defects and metal coordination on adsorption of acid gases in MOFs and metal

oxides: An in situ IR spectroscopic study. *Microporous Mesoporous Mater.* **2016,** *227*, 65-75.

(76) Xu, W. Q.; He, H.; Yu, Y. B., Deactivation of a Ce/TiO_2 Catalyst by SO_2 in the Selective Catalytic Reduction of NO by NH_3. *J. Phys. Chem. C* **2009,** *113* (11), 4426-4432.

CHAPTER 4

INSIGHTS INTO THE STABILITY OF ZEOLITIC-IMIDAZOLATE FRAMEWORKS IN HUMID ACIDIC ENVIRONMENTS FROM FIRST-PRINCIPLES CALCULATIONS*

4.1 Introduction

Metal-Organic Frameworks (MOFs), crystalline porous materials composed of metal centers/clusters connected by organic ionic ligands, have attracted great attention from both academia and industry. Their tunable chemical and physical properties[1-4] and high internal surface areas make MOFs promising candidates for applications[5-6] such as the storage and separation of gases,[7-11] catalysis,[12] and drug delivery.[13-14] Stability is a prerequisite for any industrial applications, and as such understanding the factors that govern MOF stability, as well as practical strategies for increasing stability, will play an important role in the development of these applications. The stability of MOFs has been investigated by many studies,[15] particularly with respect to exposure to water.[16-20] For instance, the resistance of MOFs towards hydrolysis can be improved by using cations with higher valence, with, for example, MILs based on Fe^{3+} cations displaying higher stability as compared to those based on divalent cations.[21] The coordination number of metal cations

* Portions of this chapter have been published previously in article "Insights into the Stability of Zeolitic Imidazolate Frameworks in Humid Acidic Environments from First-Principles Calculations" by Chu Han, Chenyang Zhang, Nina Tyminska J.R. Schmidt, and David Sholl in *the Journal of Physical Chemistry C*, 2018, volume 122, issue 8, pages 4339—4348.

is another key to high chemical and mechanical stability, with a higher coordination number usually correlated with higher stability; the UiO series of MOFs are stable in large part as a consequence of their 12-coordinated ZrO cluster centers.[19] Introducing hydrophobic or basic functional groups[22-23] into the structures can also improve the stability of MOFs.

As a subclass of MOFs, Zeolitic Imidazolate Frameworks (ZIFs), with tetrahedrally coordinated Zn or Co metal centers and organic imidazolate linkers, show excellent thermal stability and chemical stability under neutral and basic conditions.[24-27] In conjunction with their structural versatility and high surface areas, these factors make ZIFs excellent candidates for applications such as the adsorption-[28] and diffusion-based[29-30] separation of gases, supercapacitors,[31-32] and sensors.[33] Experimental work has shed light on the stability of ZIFs. ZIF-8 and ZIF-11 retain their powder-XRD (PXRD) patterns when heated and held at temperature of 500 and 300 ^{o}C, respectively, and also retain their PXRD patterns after 7 days of exposure to boiling organic solvents, water, and basic solution. This stability is matched by only a few MOFs with relatively dense structures.[24] Upon exposure to humid air, dry SO_2, and aqueous SO_2 at ambient temperature, ZIF-8's bulk properties (XRD spectra, BET surface areas) are preserved,[25-26] although ZIF-8 surfaces in various crystalline facets display degradation to different extents.[26] However, exposure of ZIF-8 to a low concentration of SO_2 in the presence of high relative humidity led to irreversible bulk structural degradation,[25,34] which indicated the synergistic effects of SO_2 and humidity in this degradation.

In addition to these experimental studies on the stability of ZIFs, computational simulation can provide atomistic insight into properties that are currently difficult to detect

experimentally. Density functional theory (DFT) calculations are widely used for this purpose and have recently been used to investigate the stability of ZIFs. Zhang *et al.*[35] investigated water-induced point defects in ZIF-8 via DFT and found that the formation of defects in this ZIF is exothermic and kinetically feasible at sufficiently high temperature. Han *et al.*[36] reported that low-energy extended stacking fault defects are plausible in ZIFs. Aside from bulk properties, Chizallet *et al.*[37] examined the stability of ZIF-8 external surfaces as a function of the coordinating conditions of surface Zn cations via cluster DFT calculations. As ZIFs adopt versatile structures based on zeolite net topologies, the influence of topology on the relative mechanical and chemical stability of hypothetical ZIF polymorphs have been studied.[27,38-40] Recent work by Akimbekov *et al.*[41] showed that thermodynamic (as opposed to chemical) stability of ZIF polymorphs is correlated with their density, with the ligand substitution playing a crucial role. Ethyl substituted ZIFs were typically found to be more stable than their methyl-substituted equivalent polymorphs, as the former ligand leads to formation of denser phases.

Despite ongoing experimental and computational efforts, many open questions remain regarding ZIF stability and reactivity, particularly under the acid-gas environments to which ZIFs may be exposed in practical applications.[42] In this work, we use DFT to study the chemical stability of ZIFs by investigating the interaction and reaction of acid-gases with bulk ZIFs and ZIF surfaces, including pristine (defect-free) and defective structures in bulk pores and on external surfaces. We also use calculations to examine the influence of ligand functionalization and framework topology, probing not only various factors which govern ZIF stability, but also their interplay.

4.2 Computational Methods

4.2.1 Overview

We utilize ZIF-2 and ZIF-8 as prototypical materials for our calculations. These two ZIFs differ in their pore sizes, topologies, and ligand functionalization. To evaluate the stability of ZIFs under acid-gas environments, we compared the gas-phase reaction energy for the formation of a dangling linker (Figure 4.1), a type of point defect proposed in our previous work,[35] induced by water, H_2S, SO_2, SO_3, H_2SO_3, or H_2SO_4. The latter acids are potential products of SO_x reacting with water, while SO_3 may form by oxidation of SO_2 in the working environment of ZIFs.[23,25-26] We then extended our study from defect-free bulk structures to the external surfaces of these two ZIFs and their bulk polymorphs to better understand the influence from local crystalline structures. To investigate the influence of various factors (e.g. ligand functionalization, ZIF topologies) on stability, we compared the defect formation energies of two sets of hypothetical ZIFs adopting various zeolite net topologies, with each set having either imidazolate (IM) or 2-methylimidazolate (mIM) ligands.

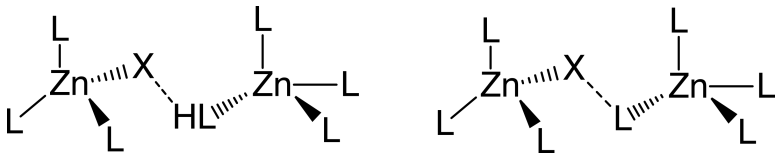

Figure 4.1 Illustration of acid-induced dangling linkers in bulk ZIFs. L denotes organic imidazolate linkers, HX and X are Brønsted and Lewis acid molecules, respectively.

The ZIF defects generated by the proposed degradation reactions may interact with acid gases differently from their defect-free parent structures, with potential implications

for defect propagation. For example, MOFs exhibiting open-metal sites (OMS) display strong adsorption sites for acid gases.[43] As such, we have also calculated the adsorption energies of several acid gases in defective ZIF bulk and surface models with OMS to compare their binding strength to the defects.

4.2.2 Periodic Density Functional Theory (DFT) Calculations

Periodic DFT calculations were performed using the Vienna Ab-initio Simulation Package (VASP) with a plane-wave basis set and the projector-augmented-wave method.[44-48] The PBE exchange-correlation functional with generalized gradient approximation and a basis set cutoff energy of 600 eV were used in all calculations.[49] Dispersion corrections were included via the DFT-D3 method.[50-51] The Brillouin zone was sampled at the Γ-point and all the ZIF structures were optimized until interionic forces were less than 0.05 eV/ Å. The Nudged Elastic Band (NEB) method[52] was used to locate reaction pathways and their associated transition states (TS), with subsequent refinement via the climbing image[53-54] NEB method. More details are given in Appendix B.

4.2.3 Models of ZIF Bulk and Surface Structures

Unit cell structures of ZIF-2 and ZIF-8 were constructed from the XRD crystal structures in the Cambridge Structural Database (CSD).[24] ZIF-2 has IM ligands, forms in the *crb* topology, with apertures of 4.8 Å, and 272 atoms per unit cell, while ZIF-8 has mIM ligands, forms in the *sod* topology, with apertures of 3.4 Å, and 276 atoms per unit cell. Geometry optimizations on these structures were performed with their lattice parameters and ionic positions fully relaxed. The optimized unit cell structures were then used to construct defective ZIF bulk models, keeping the lattice parameters fixed at the

defect-free ones for all the following energy-minimization calculations under the assumption that defects at low concentration do not alter the crystal's lattice parameters. Surface models were built in a similar way to that introduced in Chapter 3.[26] Briefly, surface slab models of ZIF-2 and ZIF-8 were constructed by cleaving Zn-N bonds crossing a (001) crystal plane and inserting a vacuum space between the upper and lower surfaces that are created to avoid interactions between image slabs in [001] direction. Here (001) surfaces were adopted to represent typical external surfaces of ZIF-2 and ZIF-8, because this crystal facet is known for ZIF-8 to be relatively more stable towards attack from acid gases.[26] To the best of our knowledge, there is no report on the stability of ZIF-2 external surfaces, so for consistency with ZIF-8, we also used the ZIF-2 (001) surface. More computational details about ZIF surfaces are given in Appendix B. For both ZIF (001) surfaces, four possible terminations exist for each ZIF, but the one with the lowest surface energy[26] was used for the following calculations. The 3-coordinated Zn atoms in the top layer of the slabs were capped with water molecules to further stabilize the surface structures. Water molecules were chosen because they have relatively higher concentration in humid condition than other species that potentially bind to Zn atoms[25-26] and these capping water molecules do not change the relative stability of various terminations. Similarly to our treatment of bulk structures calculations, energy-minimization calculations were then performed on the defective surface slabs constructed from the optimized hydrated surface models.

4.2.4 Methods for Studying Reactions Between ZIFs and Acid-Gas Molecules

In this work, the relative stability of ZIFs was investigated by studying their reactions with water and/or acid-gas molecules in the pores of bulk ZIFs and on ZIF

surfaces. In bulk ZIFs and on their surfaces, an acid-gas molecule can break a Zn-N bond, possibly protonating the imidazolate ligand, resulting in a dangling linker (DL). The relative stability of ZIF systems was determined by comparing their reaction energy for DL formation reactions,

$$\Delta E_{rxn,DL} = E_{ZIF,DL} - E_{ZIF} - E_{mol}, \quad (4.1)$$

where $\Delta E_{rxn,DL}$ is the reaction energy for the formation of a DL, $E_{ZIF,DL}$, E_{ZIF}, and E_{mol} are energies of a defective ZIF unit cell containing a DL, a pristine ZIF unit cell, and an isolated reactant molecule, respectively. A positive reaction energy denotes an endothermic reaction. The activation energies were also calculated for all the reactions in bulk and part of that on surfaces by using the NEB method. The activation energy is defined as the difference between the energies of transition state and initial state of the system.

Another type of interaction between ZIFs and acid gases, the adsorption of these species in bulk ZIFs as well as on their external surfaces, was also examined. The adsorption energy was defined by

$$\Delta E_{ads} = E_{mol+ZIF} - E_{mol} - E_{ZIF}, \quad (4.2)$$

where ΔE_{ads} is the adsorption energy, $E_{mol+ZIF}$, E_{mol}, and E_{ZIF} are energies of ZIF-molecule complex, an isolated gas molecule, and a ZIF bulk or surface unit cell, respectively. A negative adsorption energy denotes exothermic adsorption.

4.2.5 Steric Effects: Topology and Ligand Functionalization

In addition to ZIF-2 and ZIF-8, two sets of ZIF polymorphs[38-39,55] were constructed to study the influence of ligand functionalization and topology. Eight framework

topologies, *dia*, *crb*, *sod*, *unc*, *cfc*, *gis*, *sra*, and *pcl*, that have distinct apertures and cavity sizes (Table B.1), were used. ZIFs in most of these eight topologies have been synthesized, although for functionalization that differ from those of ZIF-2 [($Zn(IM)_2$) and ZIF-8 [$Zn(mIM)_2$].[24,56] The unit cell structures of these hypothetical ZIFs were constructed by taking the structures reported by Baburin *et al*.[55] as initial configurations and optimizing these structures with DFT calculations in the same way as described above for ZIF-2 and ZIF-8. The resulting $Zn(IM)_2$ materials in the *crb* topology has the same net connectivity as ZIF-2, but distortions in the material's cages result in different lattice constants from that of ZIF-2. This variation is not entirely surprising, as ZIF-1 and ZIF-2 have both been synthesized experimentally in the *crb* topology with the same stoichiometry but different porosity.[24] We investigated the water stability of these sets of polymorphs by calculating the reaction energy for the formation of a point defect as in Section 4.2.4.

4.3 Results and Discussion

4.3.1 Chemical Stability of Bulk ZIFs Under Humid Acid-Gas Conditions

Degradation in ZIFs presumably begins with Zn-N bond cleavage, which may result in point defects such as dangling linkers (DL), linker vacancies (LV), and metal cation vacancies.[35] Among the potential point defects, DLs are thought to emerge first, with the formation of other defects following the formation of DLs.[25-26] We studied the formation of a DL in bulk ZIF-2 and ZIF-8 to investigate ZIF initial degradation under humid acid-gas conditions. Potential degradation mechanisms for ZIFs with a Brønsted acid-gas molecule (HX) and a Lewis acid (X) are presented in Figure 4.2. During the

reaction with a Brønsted acid (HX), a proton transfers from HX to an imidazolate linker with the conjugate base (X^-) binding to the Zn atom that originally binds to this linker. A Lewis acid such as SO_2 is able to insert into a Zn-N bond by forming a Zn-O bond and a N-S bond.

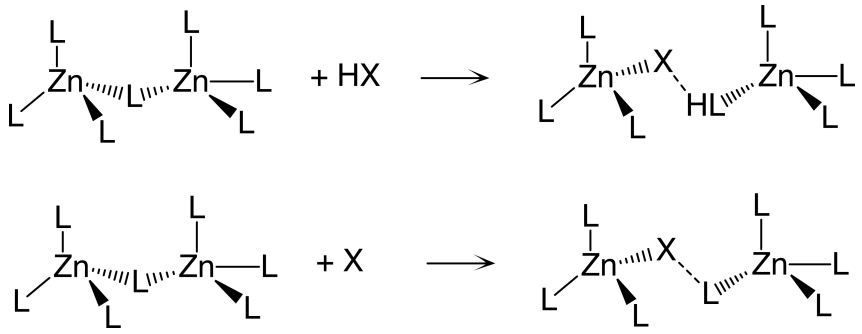

Figure 4.2 Dangling linker formation reactions in bulk ZIF with Brønsted and Lewis acid gas molecules (HX and X, respectively). L denotes an organic imidazolate ligand.

The DFT-calculated reaction energies for DL formation between bulk ZIFs and H_2O, H_2S, H_2SO_3, H_2SO_4, SO_2, or SO_3, are shown in Table 4.1. These calculations do not consider the presence of any additional solvent or other molecules in the ZIF's pores. Most of the reactions with acid-gas molecules were exothermic except those between ZIF-2 and SO_2, ZIF-8 and SO_2, H_2O, and H_2S. The reaction energy for both ZIFs with H_2O and the Brønsted acids H_2S, H_2SO_3, and H_2SO_4 decreases as the acidity increases. The Brønsted acids can be compared by their gas-phase acidity, defined as the Gibbs free energy change ($\Delta_{acid}G$) for the reaction $AH \rightarrow A^- + H^+$ at 298 K. A lower $\Delta_{acid}G$ indicates a stronger acid. $\Delta_{acid}G$ for H_2O, H_2S, and H_2SO_4 are 382.8, 344.7, and 302.6 kcal/mol, respectively,[57] which are in the same order as their pK_a in aqueous solution.[58] SO_3, which is a stronger Lewis

acid than SO_2, leads to much more exothermic defect formation than SO_2. It is interesting to note that ZIF-8 exhibits a systematically higher reaction energy than ZIF-2 (by about 7-12 kcal/mol) for all species examined.

To further understand the kinetic stability of the bulk ZIFs, we performed reaction pathway calculations to obtain the activation energies (ΔE^a) for the aforementioned reactions. The resulting activation energies are provided in Table 4.1. Similarly to the trends of reaction energy, the values of ΔE^a are systematically higher in ZIF-8 than in ZIF-2. The difference in activation energies between the two ZIFs is similar to the difference in the reaction energies. The activation energies for the Brønsted acids (H_2S, H_2SO_3, and H_2SO_4) and Lewis acids (SO_2 and SO_3) separately show the same trends as their reaction energies. Considering both thermal and kinetic stability, H_2SO_4 degrades ZIF structures more easily compared with water. SO_3 is the most potent reactant for bulk ZIF-2. In general, ZIF-2 and ZIF-8 are more prone to degradation by strong acid gases such as H_2SO_4 and SO_3 than hydrolysis.[25-26,59] However, ZIF-8 is more stable than ZIF-2 to an acid-gas-induced first step of the degradation process. Our calculations are consistent with the experimental observations that ZIF-8 resists dry SO_2 but degrades in the presence of water (due to possible formation of H_2SO_3) or via SO_2 oxidation (leading to formation of SO_3/H_2SO_4).[25-26] The detailed mechanisms of reactions with sulfurous and sulfuric acids are discussed further in section 4.3.3.

Table 4.1 Reaction energy (ΔE_{rxn} in Eq. 4.1) and activation energy (ΔE^a) in kcal/mol for the formation of a dangling linker induced by H_2O, H_2S, H_2SO_3, H_2SO_4, SO_2, and SO_3 in bulk ZIFs. The acid gases are categorized as Brønsted and Lewis acids in ascending order of acidity (descending order of pK_a values). pK_a values of Lewis acids are taken from their products with water.

Reactant		pK_a [58]	$\Delta E_{rxn,DL}$		ΔE^a	
			ZIF-2	ZIF-8	ZIF-2	ZIF-8
Brønsted acid	H_2O	14	-1.6	8.2	13.8	22.2
	H_2S	7.1	-6.8	5.7	22.1	29.6
	H_2SO_3	1.9	-17.7	-7.0	15.2	21.5
	H_2SO_4	-9.0 [60]	-27.0	-17.7	13.5	16.8
Lewis acid	SO_2	1.9	0.1	7.5	19.0	31.3
	SO_3	-9.0	-26.4	-19.6	4.0	22.3

4.3.2 Stability as a Function of ZIF Topology and Ligand Species

All ZIFs, including ZIF-2 and ZIF-8, exhibit identical local structure, with tetrahedrally coordinated Zn metal centers; these ZIFs differ only in their topology and ligand functionalization. Interestingly, the data above shows that ZIF-8 is less reactive than ZIF-2 upon exposure to water and all the acid gas species we considered. Here we aim to understand whether pore topology or ligand functionalization dominates in controlling the relative stability of the two ZIFs. To isolate the effects of topology and functionalization, we used two sets of ZIF polymorphs, namely, $Zn(mIM)_2$, of which ZIF-8 is a member, and $Zn(IM)_2$, of which ZIF-2 is a member. Eight topologies, *dia*, *crb*, *sod*, *unc*, *cfc*, *gis*, *sra*, and *pcl*, were adopted for each set of ZIF polymorphs. With these hypothetical ZIF polymorphs, we were able to make comparison between ZIFs with the same topology but different ligands, or with the same ligands but different topologies. The stability of these

polymorphs was determined by examining the reaction energies for the formation of a linker vacancy (LV) formed by two water molecules replacing a ligand and resulting in Zn atoms bonded to a hydroxyl group and a water molecule, as shown in Figure 4.3. The LV was used to investigate the relative stability of polymorphs because this type of defect has the same number of atoms (H_3O_2 as shown in Figure 4.3) between two Zn atoms for both $Zn(mIM)_2$ and $Zn(IM)_2$, which makes the comparison simpler. In contrast, in the case of a DL defect, the nature of the "dangling" linker varies between $Zn(IM)_2$ and $Zn(mIM)_2$. The reaction energy for forming a linker vacancy is calculated by

$$\Delta E_{rxn,LV} = E_{ZIF+LV} + E_{HL} - E_{ZIF} - 2E_{H_2O}, \tag{4.3}$$

where $\Delta E_{rxn,LV}$ is the reaction energy for the formation of a LV, E_{ZIF+LV}, E_{HL}, E_{ZIF}, and E_{H_2O} are energies of a defective ZIF unit cell, an isolated 2-methylimidazole (for $Zn(mIM)_2$) or imidazole (for $Zn(IM)_2$) molecule, a pristine ZIF unit cell, and an isolated water molecule, respectively. A positive reaction energy denotes an endothermic reaction.

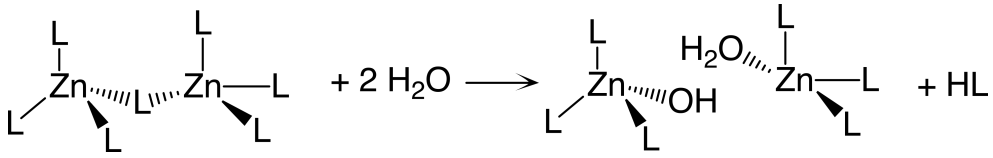

Figure 4.3 Formation of a linker vacancy by two water molecules. L denotes an organic imidazolate ligand, whereas HL denotes its protonated equivalent.

The comparison of thermodynamic stability between various topologies for $Zn(mIM)_2$ and $Zn(IM)_2$ polymorphs is shown in Figure 4.4a. Despite substantial differences in pore diameters, aperture sizes, etc. amongst the various topologies, we find that reaction energies of forming a LV for $Zn(IM)_2$ polymorphs vary between 5 and 9

kcal/mol. Similarly, in the case of $Zn(mIM)_2$ polymorphs the reaction energies were found to be in the range of 9 to 14 kcal/mol. As noted above, our calculations included two different ZIF-2 structures in the *crb* topology; these structures give reaction energies that differ by ~2 kcal/mol. We did not observe an obvious correlation in the overall set of results between the calculated reaction energies and structural factors such as the cavity or aperture sizes (Figure B.1).

The most obvious trend from our calculations is that the $Zn(mIM)_2$ materials have a systemically higher reaction energy than $Zn(IM)_2$ materials, consistent with observed trends for the specific case of ZIF-8 vs. ZIF-2. This is likely because the larger steric bulk of the mIM ligands somewhat protects the Zn metal centers from attack by water. As mentioned, above bulkier ligands have been shown to increase thermodynamic stability of ZIF polymorphs,[41] however the influence of ligand on the chemical stability may not be as pronounced. Based on result from our calculations that the overall variability due to changes in topology (left side of Fig. 4.4b) and changes in the ligand (right side of Fig. 4.4b) is similar. That is, we cannot conclude that one of these factors dominates in these examples. The variation in reaction energies among topologies with the same ligand could be due to the difference in the intrinsic stability of the pristine structures, where this quantity is judged using the relative energy of the pristine structures. Among the eight $Zn(mIM)_2$ polymorphs, *dia* and *pcl* are the most and least stable structures based on the calculated energy of a $Zn(mIM)_2$ formula unit, while the formation of a LV in these two structures is the least and one of the most energetically favorable. Seven out of eight topologies for the $Zn(mIM)_2$ polymorphs show the trend that formation of a LV in more stable structures is less energetically favorable (Figure B.1).

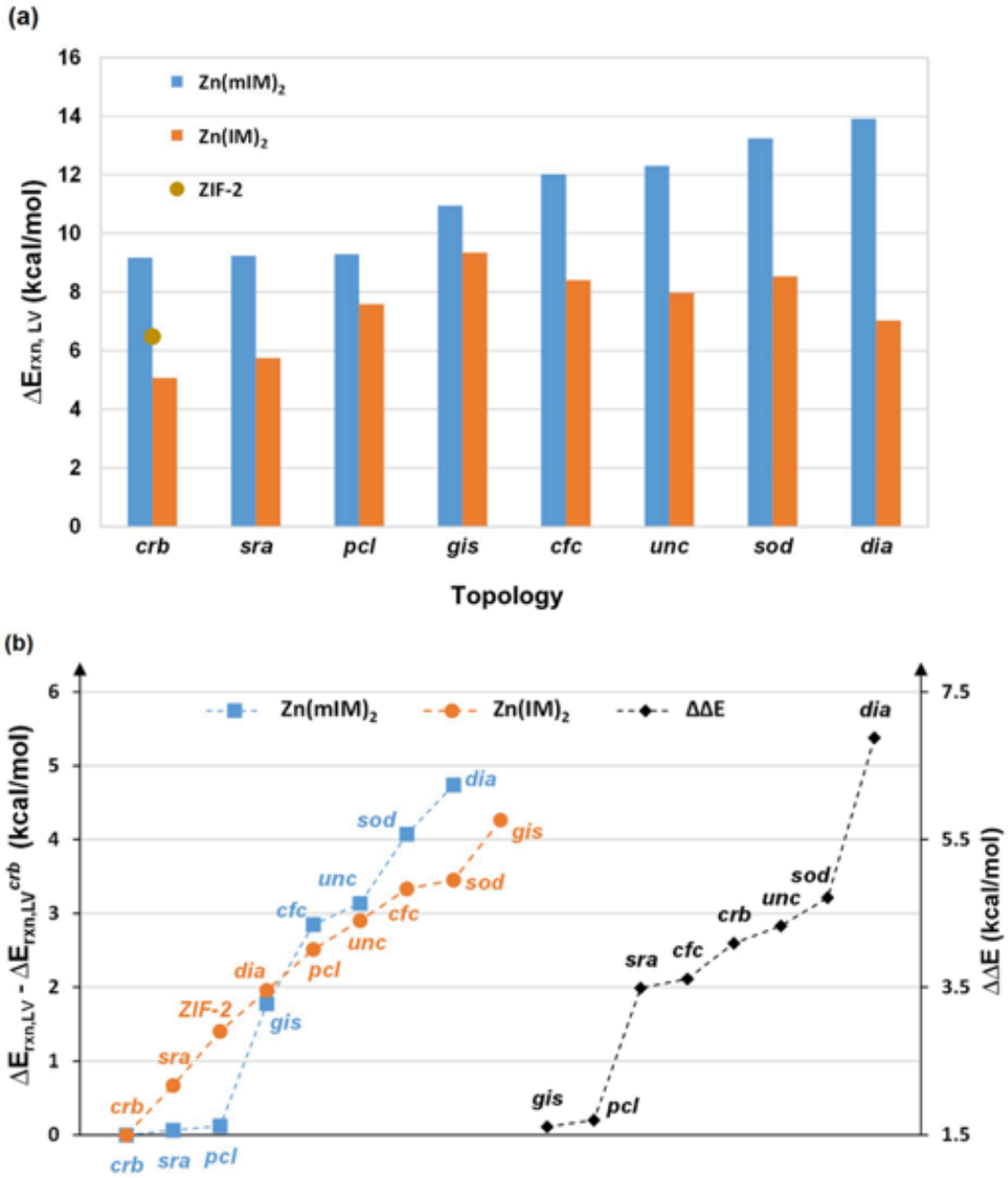

Figure 4.4 (a) Linker vacancy formation energies ($\Delta E_{rxn,LV}$) in the pores of bulk ZIF polymorphs with various topologies. Because the *crb* $Zn(IM)_2$ polymorph has distorted cages and different lattice parameters from ZIF-2, $\Delta E_{rxn,LV}$ for ZIF-2 (indicated by a yellow bullet) and the *crb* $Zn(IM)_2$ polymorph are different. (b) $\Delta E_{rxn,LV}$ for $Zn(mIM)_2$ (blue squares) and $Zn(IM)_2$ (orange bullets) polymorphs relative to that of their *crb* structure, which has the lowest $\Delta E_{rxn,LV}$ for both sets of polymorphs. Results for each pore topology are plotted in ascending order equally spaced along the horizontal axis with dotted lines to guide the eye. $\Delta\Delta E = \Delta E_{rxn,\ LV}[Zn(mIM)_2] - \Delta E_{rxn,\ LV}[Zn(IM)_2]$ is also plotted with corresponding topology codes (black diamonds) in ascending order (values on right vertical axis).

4.3.3 Reactions Between ZIF-8 and H_2O/H_2SO_x

As mentioned in the Introduction, recent experimental work[25] has shown that prolonged exposure to humid SO_2 leads to degradation of ZIF-8. These experiments showed the presence of S-containing products (bi-sulfite and bi-sufate) associated with SO_2 reactions with water after reactivation of the material after exposure. Note that H_2SO_4 could potentially form via oxidation of SO_2 in humid air. These observations motivated us to investigate the degradation process for a pristine ZIF-8 crystal in a humid H_2SO_x environment. The results in section 4.3.1 suggest that formation of a DL in bulk ZIF-8 by reactions with H_2SO_x species may provide information about to what extent a relatively more stable ZIF may degrade when exposed to severe acidic environments, since this represents a key step in the degradation of the most stable material we examined with the most reactive species we considered.

Pristine ZIF structures experience a two-step reaction to form a LV. An H_2SO_x molecule is adsorbed into the pore and then breaks a Zn-N bond with the donation of a proton to the N of a mIM ligand. This step results in a DL that can be thought of as an intermediate for the formation of a LV. This reaction (noted as I in Figure 4.5a) is energetically demanding (ΔE_1^a = 21.5 kcal/mol and 16.8 kcal/mol for H_2SO_3 and H_2SO_4 in ZIF-8, respectively). The second reaction (noted as II in Figure 5a) involves adsorption of a water molecule into the pore followed by the attack of this molecule on a second Zn-N bond, generating a protonated organic ligand (HL). The subsequent process of cleaving this bond is less energetically demanding (ΔE_2^a =16.3 kcal/mol and 12.5 kcal/mol for H_2SO_3 and H_2SO_4 in ZIF-8, respectively). Overall the LV formation reaction is exothermic ($\Delta E_{rxn,LV}$ = -23.4 kcal/mol), and it leaves a chemisorbed HSO_3^- in the framework, consistent

with XPS showing residual S in degraded ZIF-8.[25] Our results imply that even a small amount of SO_3/H_2SO_4 provides a relatively low barrier pathway for a stoichiometric reaction between ZIF-8 and adsorbed molecules.

Although reactions involving SO_2/H_2SO_3 display larger barriers as compared to H_2SO_4, the presence of even trace amounts of the latter in conjunction with the former opens a low-barrier catalytic pathway to degradation. Figure 4.5b shows the reactions between ZIF-8 and H_2SO_3/H_2O in the presence of H_2SO_4. The recovery of a sulfuric acid from a defect formed by H_2SO_4/H_2O involves adsorption of an H_2SO_3, followed by the exchange of its HSO_3^- with the HSO_4^- ion of the defect and regenerating a H_2SO_4 molecule that remains physisorbed in pores and ready for the next reaction cycle. Details regarding the recovery process can be found in Appendix B together with associated energy profiles. The energy barrier associated with HSO_3^-/HSO_4^- exchange is small (~5 kcal/mol) and the reaction is strongly exothermic. This could be because H_2SO_3 introduces less steric hindrance than H_2SO_4. The desorption of sulfuric acid out of the framework is energetically demanding (Figure B.2), but is likely to be bypassed in practice, since this strong acid simply remains physisorbed in the pore and breaks a subsequent Zn-N bond. To the best of our knowledge, this work is the first elucidation of the full mechanism of the LV formation in ZIFs with H_2SO_3/H_2O and the same reaction catalyzed by a trace amount of H_2SO_4

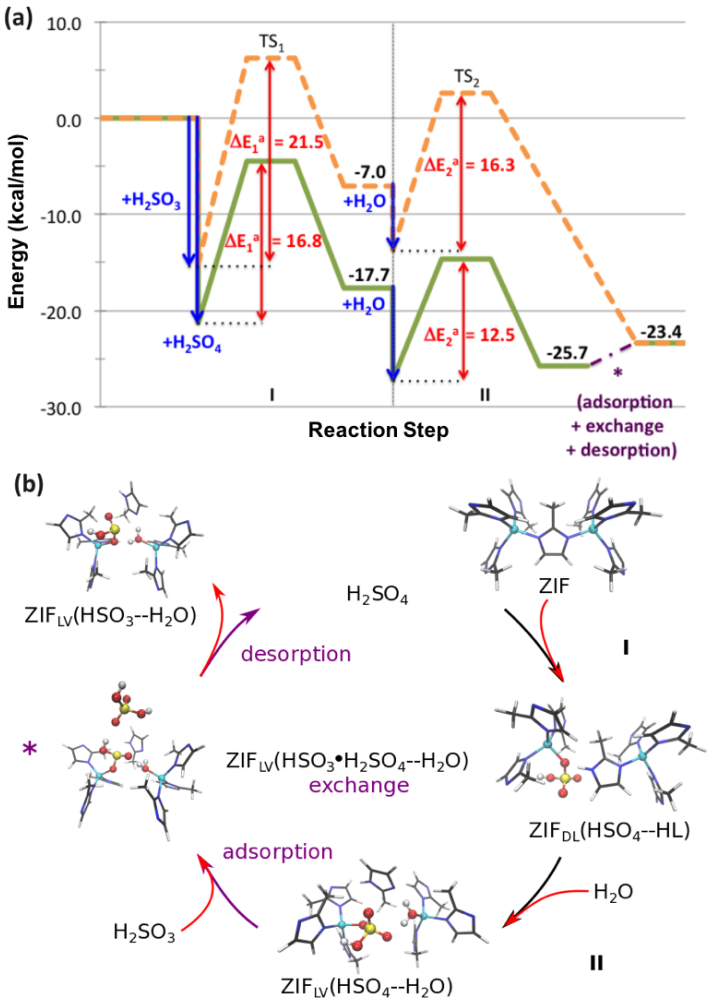

Figure 4.5 (a) Energy profiles associated with a linker vacancy (LV) formation reaction between bulk ZIF-8 and H_2SO_3/H_2O with (green solid line) and without (orange dashed line) the presence of H_2SO_4. An energy of zero corresponds to isolated bulk ZIF-8 (unit cell), acid species, and water molecules. Reaction step I involves the adsorption of an H_2SO_x molecule into the pore, followed by the formation of a dangling linker (DL). Step II involves adsorption of an H_2O molecule, followed by the formation of a LV. The energy barriers for steps I and II are provided in red (denoted as ΔE_1^a and ΔE_2^a, respectively), while the reaction energies are given in black. TS_1 and TS_2 denote positions of the transition states for steps I and II relative to the energy (dotted lines) of frameworks and physisorbed reacting molecules in pores. The dashed purple line shows the total energy change for the processes of H_2SO_3 adsorption, H_2SO_3 and H_2SO_4 exchange, and H_2SO_4 desorption after the formation of a LV by H_2SO_4/H_2O. More detailed energy profiles for these steps can be found in Figure B.2. (b) A schematic thermodynamic cycle for a LV formation in ZIF-8 reacting with H_2SO_3, H_2SO_4 and H_2O (corresponding to the energy profile labeled by green solid and purple dashed lines in (a)). Local structures of intermediate products are shown. Labels ZIF, $ZIF_{DL}(HSO_4\text{--}HL)$, $ZIF_{LV}(HSO_x\text{--}H_2O)$, and $ZIF_{LV}(HSO_3\bullet H_2SO_4—H_2O)$ correspond to pristine bulk ZIF-8, defective ZIF-8 containing a DL having an HSO_4^- ion, defective ZIF-8 containing a LV composed of an HSO_x^- ion and a water molecule, and defective ZIF-8 containing a physisorbed H_2SO_4 and a LV composed of an HSO_3^- ion and a water molecule. H, C, N, O, S and Zn atoms are colored in white, black, blue, red, yellow and cyan, respectively.

4.3.4 Chemical Stability of ZIF (001) Surfaces Under Humid Acid-Gas Conditions

In addition to the internal pores of ZIFs and similar materials, the external surfaces of ZIFs can also potentially present sites that lead to degradation. External surfaces are particularly important for nano-sized particles, since in that instance the surface area associated with external surfaces can approach the internal surface area of even high surface area porous materials[1,61]. The external surfaces of ZIFs have intrinsically lower coordination environments and/or different chemical terminations than the interior pores of these materials. It is therefore of considerable interest to compare the reactivity of the external surfaces of ZIFs with their interior pores. Here we use (001) crystal facets of ZIF-2 and ZIF-8 as a prototypical example of a ZIF external surface; we have shown previously that the (001) surface is one of ZIF-8's most stable surfaces under humid acid-gas conditions.[26] In our surface slab models, the external Zn atoms coordinated with three organic linkers and terminated by water molecules. We considered the formation of dangling linkers (DL) for these sites as illustrated in Figure 4.6.

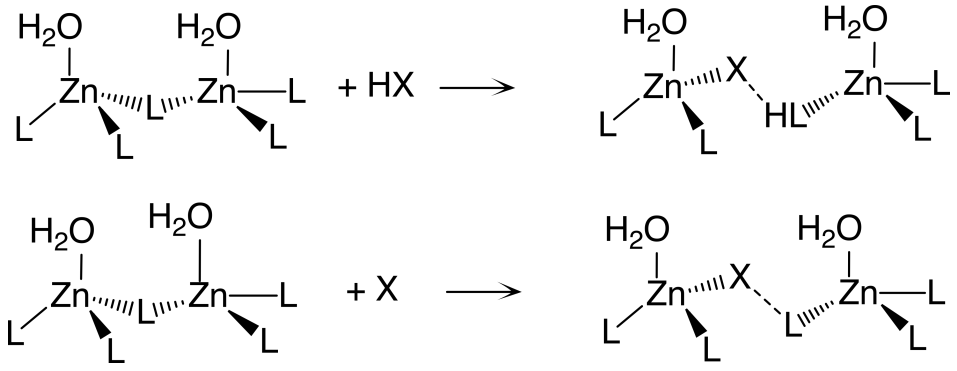

Figure 4.6 Dangling linker formation reactions on hydrated ZIF surfaces with Brønsted and Lewis acid gas molecules (HX and X, respectively). The Zn atoms shown belong to the external layer of surfaces, which are initially terminated by water molecules.

The reaction energies for DL formation between ZIF surfaces and H_2O, H_2S, H_2SO_3, H_2SO_4, SO_2, or SO_3 are shown in Table 4.2. The general trends on the surfaces are similar to those for the bulk materials (Table 4.1), with most of the reactions being exothermic, except those with SO_2. In most cases the formation energies for the surface defects are more favorable than in the bulk, in some instances by more the 20 kcal/mol. The most exothermic reactions for ZIF surfaces were those with H_2SO_3 or H_2SO_4. The DFT-optimized defective surface structures show an HSO_x^- ion interacting with terminating water molecules by forming a weak hydrogen bond between one of its dangling oxygen atom and one of the hydrogen atoms of a water molecule (Figure B.11); this type of interaction was not observed for other species. To further understand the role of the surface water molecules, we examined the same reactions on "clean" surfaces that had unsaturated surface Zn atoms (without terminating water molecules). The calculated reaction energies for DL formation of clean surfaces with H_2SO_3 and H_2SO_4 are -15.1 and -24.0 kcal/mol for ZIF-2, -16.1 and -23.9 kcal/mol for ZIF-8, respectively. These results highlight the importance of surface water molecules in stabilizing the reaction products, particularly for the ZIF-2 surface.

Table 4.2 Reaction energy ($\Delta E_{rxn,DL}$ in Eq. 4.1) in kcal/mol for the formation of a dangling linker induced by H_2O, H_2S, H_2SO_3, H_2SO_4, SO_2, and SO_3 on hydrated ZIF (001) surfaces. The acid gases are categorized as Brønsted and Lewis acids in ascending order of acidity (descending order of pK_a values). pK_a values of Lewis acids are taken from their products with water.

Reactant		pK_a [58]	ZIF-2	ZIF-8
Brønsted Acid	H_2O	14	-7.7	-5.7
	H_2S	7.1	-19.1	-16.0
	H_2SO_3	1.9	-40.3	-23.0
	H_2SO_4	-9.0 [60]	-42.7	-28.5
Lewis Acid	SO_2	1.9	0.1	0.2
	SO_3	-9.0	-27.2	-23.5

A comparison of the DL formation reaction energies in the pore of bulk ZIFs versus their surfaces is illustrated in Figure 4.7. Surfaces are systematically more reactive than bulk structures for both ZIF-2 and ZIF-8 based of the comparison of the reaction energies for the same reactions in bulk and on surfaces. One possible explanation is that surfaces are more flexible than bulk and therefore more prone to make steric accommodation for the deformation caused by defects such as a DL. Furthermore, consistent with the trend in bulk ZIFs, the ZIF-8 surface also shows higher thermodynamic stability vs. the ZIF-2 surface, which likely results from the difference in topology and bulkier ligands (mIM).

To further understand the kinetic stability of ZIF surfaces relative to the bulk, we examined the activation energy for DL formation on ZIF-8 surface induced by water. The calculated activation energy for DL formation by a water molecule at a hydrated ZIF-8 external surface is ~7.5 kcal/mol lower than the same reaction in bulk ZIF-8 and ~2

kcal/mol lower than the DL formation by an H_2SO_4 molecule in bulk ZIF-8, which is the most energetically favorable reaction in bulk ZIF-8 that we have examined. As the terminating water molecules stabilize the reaction products, the DL formation by a water molecule at a clean surface has a higher activation energy (ΔE^a =17.3 kcal/mol) than that on hydrated surface, yet it is still ~5 kcal/mol lower than the same reaction in bulk. Assuming the activation energy for surface reactions follows the same trend as in bulk, then the reaction with H_2SO_4 on ZIF-8 surface would have a lower activation energy than that with water, with DL formation with H_2SO_4 on surface substantially more kinetically favorable as compared to the bulk. Consequently, since reaction energies are both systematically more thermodynamically (i.e. exothermic) and kinetically favorable on surfaces, the degradation process is likely to be dominated by the attack of acid gases on the outer surfaces of ZIFs.

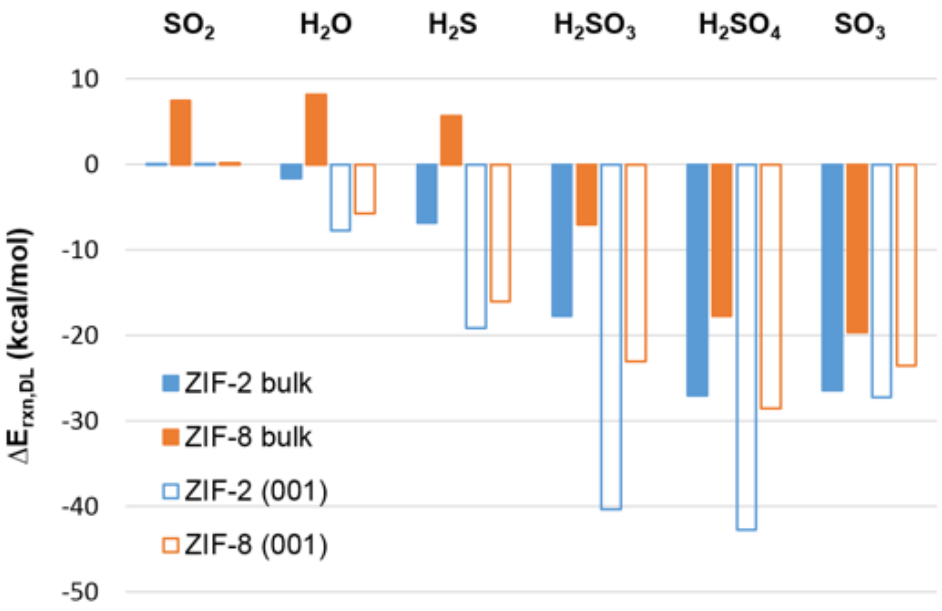

Figure 4.7 Reaction energy of dangling linker formation in bulk ZIFs and on ZIF surfaces for acid gases SO_2, H_2O, H_2S, H_2SO_3, H_2SO_4, and SO_3. The values of $\Delta E_{rxn,DL}$ are from Tables 4.1 and 4.2.

4.3.5 Adsorption of Acid-Gas Molecules by Defective ZIFs

From our investigation on the defect formation in ZIFs, one can imagine that one or more Zn-N bonds break upon reactions in humid acidic environment. Although we have not yet investigated defect propagation, as an step toward this goal, we also examined the interactions between defective ZIFs and acid gases; these interactions may also be relevant to possible regeneration methodologies[62-63] as well as in ZIF applications such as gas separation/capture[64] and catalysis (owing to functionalization by chemisorbed acid groups).[65] Unsaturated Zn atoms, known as open-metal sites (OMS), a type of strong adsorption sites for acid gases,[43] are an inevitable product of ZIF point defects. Here we built defective bulk and surface models of ZIFs containing OMS to study the adsorption strength of H_2O, H_2S, H_2SO_3, H_2SO_4, SO_2, and SO_3 to these OMS.

To construct the model for defective bulk ZIFs, we removed a linker from a ZIF unit cell, resulting in two OMS and a void between them in a bulk unit cell. This model is different from the structure of a LV described earlier (where the two Zn atoms are fully coordinated, since an ion [OH^-] and a neutral molecule [H_2O] become terminating groups). This structure is relevant for at least two reasons. First, this structure has "pure" OMS, eliminating the influence from other adsorbates on the adsorption of acid gases; second, this structure may exist after "activation" of defective ZIFs with linker vacancies, where application of temperature/vacuum may induce loss of terminating groups. This defective bulk ZIF model could be also relevant for freshly cleaved surface. To make a defective ZIF surface model comparable to the bulk model, we built a clean surface model, with the same coordination numbers of the Zn atoms at defect sites in bulk, all the external surface Zn atoms are 3-coordinated with imidazolate ligands (i.e., without terminating molecules bond

to them). In the clean surface models of ZIF-2 and ZIF-8, there are 8 and 4 unsaturated Zn atoms in a unit cell on the external layer, respectively. To minimize the interactions between adsorbates, in our simulation we kept only one adsorbate molecule per unit cell. The defective bulk and surface models are shown in Figure B.5.

Table 4.3 lists the adsorption energy of water and several acid gases on OMS in defective ZIF-2 and ZIF-8. The relative adsorption strengths for the six adsorbates to OMS are consistent for bulk and surfaces, with water and H_2S relatively weakly adsorbed, H_2SO_x molecules adsorbed with a moderate strength, and SO_x molecules the most strongly adsorbed. The order of adsorption strength for H_2S, H_2O and SO_2 on ZIF surfaces agrees with that reported for Zn-BDC sheets calculated at the same level of theory.[43] Crucially, these results suggest that under humid acid-gas conditions, adsorption of acid gases on OMS is favored over water in defective ZIFs, with potential implications for subsequent defect propagation. In addition, we note that for both ZIFs, adsorption is stronger in the bulk than on external surfaces since binding in the bulk is bidentate while binding on external surfaces is monodentate. Interestingly, we found that dissociative adsorption of H_2S, H_2SO_3, and H_2SO_4 molecules in bulk is favorable compared with their molecular (non-dissociative) adsorption. More details about adsorption calculations and optimized structures are included in Appendix B.

Table 4.3 Adsorption energies (in kcal/mol) of water and acid-gas molecules at OMS in defective bulk ZIFs and ZIF (001) surfaces. Numbers in parentheses are adsorption energies for dissociative H_2S, H_2SO_3, and H_2SO_4 molecules.

	$\Delta E_{ads,bulk}$		$\Delta E_{ads,(001)}$	
Reactant	**ZIF-2**	**ZIF-8**	**ZIF-2**	**ZIF-8**
H_2O	-27.0	-25.0	-14.5	-15.0
H_2S	-18.7 (-34.1)	-17.2 (-33.5)	-12.9	-13.5
H_2SO_3	(-55.2)	(-53.7)	-20.6	-15.5
H_2SO_4	-53.1 (-61.7)	-45.8 (-52.9)	-20.5	-29.1
SO_2	-73.6	-71.7	-44.6	-54.4
SO_3	-87.7	-83.7	-80.1	-85.2

Examining the adsorption energies of molecules to OMS in defective ZIFs, we speculate that acid-gas species such as SO_x and H_2SO_x would remain adsorbed in the defective structures at mild operating conditions due to their strong adsorption strength. Consequently, if OMS is a key factor in the potential applications of ZIFs, once contaminated by these acid gases, these OMS in ZIFs can only be regenerated under very demanding requirements, for instance, through chemical routes combined with the most commonly used thermal activation.[66]

4.4 Summary

We have performed a systematic computational investigation of the chemical stability of ZIFs under humid acid-gas condition via DFT, comparing the interactions of defect-free bulk structures, external surfaces, and point defects in ZIF pores with acid gases and water. Examining the degradation of two prototypical ZIFs, ZIF-2 and ZIF-8, by acid gases (including H_2O, H_2S, SO_2, SO_3, H_2SO_3, or H_2SO_4) demonstrates that both ZIFs show

higher stability in the interior of their pores than on their external surfaces, thus suggesting that the degradation of ZIFs starts from the external surfaces. We find that ZIF-8 is more thermodynamically and kinetically stable than ZIF-2 based on their reactions with all the studied acid gases, with ZIF stability governed, more generally, by both topology and ligand functionalization.

We also find that weak-acid-induced degradation of ZIFs can be catalyzed by a small amount of strong acid such as sulfuric acid. This finding implies that the kinetic barriers obtained by current models are the upper bounds of real activation energies associated with the degradation cause by a mixture of acid gases.

The adsorption of acid gases to defective ZIF structures also reveals potential challenges in the regeneration of these materials as well as possible influence on defect propagation. Our study paves the way for the future exploration of these two topics.

4.5 References

(1) Sholl, D. S.; Lively, R. P., Defects in Metal-Organic Frameworks: Challenge or Opportunity? *J. Phys. Chem. Lett.* **2015,** *6* (17), 3437-3444.

(2) Joshi, J. N.; Garcia-Gutierrez, E. Y.; Moran, C. M.; Deneff, J. I.; Walton, K. S., Engineering Copper Carboxylate Functionalities on Water Stable Metal-Organic Frameworks for Enhancement of Ammonia Removal Capacities. *J. Phys. Chem. C* **2017,** *121* (6), 3310-3319.

(3) Fang, Z. L.; Bueken, B.; De Vos, D. E.; Fischer, R. A., Defect-Engineered Metal-Organic Frameworks. *Angew. Chem., Int. Ed.* **2015,** *54* (25), 7234-7254.

(4) McGuire, C. V.; Forgan, R. S., The surface chemistry of metal-organic frameworks. *Chem. Commun.* **2015,** *51* (25), 5199-5217.

(5) Falcaro, P.; Ricco, R.; Doherty, C. M.; Liang, K.; Hill, A. J.; Styles, M. J., MOF positioning technology and device fabrication. *Chem. Soc. Rev.* **2014,** *43* (16), 5513-5560.

(6) Furukawa, H.; Cordova, K. E.; O'Keeffe, M.; Yaghi, O. M., The Chemistry and Applications of Metal-Organic Frameworks. *Science* **2013,** *341* (6149), 1230444.

(7) Zhao, Z. X.; Ma, X. L.; Kasik, A.; Li, Z.; Lin, Y. S., Gas Separation Properties of Metal Organic Framework (MOF-5) Membranes. *Ind. Eng. Chem. Res.* **2013,** *52* (3), 1102-1108.

(8) Zhang, L. L.; Wu, G.; Jiang, J. W., Adsorption and Diffusion of CO_2 and CH_4 in Zeolitic Imidazolate Framework-8: Effect of Structural Flexibility. *J. Phys. Chem. C* **2014,** *118* (17), 8788-8794.

(9) Wang, H.; Yao, K. X.; Zhang, Z. J.; Jagiello, J.; Gong, Q. H.; Han, Y.; Li, J., The first example of commensurate adsorption of atomic gas in a MOF and effective separation of xenon from other noble gases. *Chem. Sci.* **2014,** *5* (2), 620-624.

(10) Ma, S. Q.; Zhou, H. C., Gas storage in porous metal-organic frameworks for clean energy applications. *Chem. Commun.* **2010,** *46* (1), 44-53.

(11) Alezi, D.; Belmabkhout, Y.; Suyetin, M.; Bhatt, P. M.; Weselinski, L. J.; Solovyeva, V.; Adil, K.; Spanopoulos, I.; Trikalitis, P. N.; Emwas, A. H.; Eddaoudi, M., MOF Crystal Chemistry Paving the Way to Gas Storage Needs: Aluminum-Based soc-MOF for CH_4, O_2, and CO_2 Storage. *J. Am. Chem. Soc.* **2015,** *137* (41), 13308-13318.

(12) Burgun, A.; Crees, R. S.; Cole, M. L.; Doonan, C. J.; Sumby, C. J., A 3-D diamondoid MOF catalyst based on in situ generated $[Cu(L)_2]$ N-heterocyclic carbene (NHC) linkers: hydroboration of CO_2. *Chem. Commun.* **2014,** *50* (79), 11760-11763.

(13) Orellana-Tavra, C.; Baxter, E. F.; Tian, T.; Bennett, T. D.; Slater, N. K. H.; Cheetham, A. K.; Fairen-Jimenez, D., Amorphous metal-organic frameworks for drug delivery. *Chem. Commun.* **2015,** *51* (73), 13878-13881.

(14) Horcajada, P.; Serre, C.; Vallet-Regi, M.; Sebban, M.; Taulelle, F.; Ferey, G., Metal-organic frameworks as efficient materials for drug delivery. *Angew. Chem. Int. Ed.* **2006,** *45* (36), 5974-5978.

(15) Howarth, A. J.; Liu, Y. Y.; Li, P.; Li, Z. Y.; Wang, T. C.; Hupp, J.; Farha, O. K., Chemical, thermal and mechanical stabilities of metal-organic frameworks. *Nat. Rev. Mater.* **2016,** *1* (3), 15018.

(16) Burtch, N. C.; Jasuja, H.; Walton, K. S., Water Stability and Adsorption in Metal-Organic Frameworks. *Chem. Rev.* **2014,** *114* (20), 10575-10612.

(17) Jiao, Y.; Morelock, C. R.; Burtch, N. C.; Mounfield, W. P.; Hungerford, J. T.; Walton, K. S., Tuning the Kinetic Water Stability and Adsorption Interactions of Mg-MOF-74 by Partial Substitution with Co or Ni. *Ind. Eng. Chem. Res.* **2015,** *54* (49), 12408-12414.

(18) Zhou, K.; Mousavi, B.; Luo, Z. X.; Phatanasri, S.; Chaemchuen, S.; Verpoort, F., Characterization and properties of Zn/Co zeolitic imidazolate frameworks vs. ZIF-8 and ZIF-67. *J. Mater. Chem. A* **2017,** *5* (3), 952-957.

(19) DeCoste, J. B.; Peterson, G. W.; Schindler, B. J.; Killops, K. L.; Browe, M. A.; Mahle, J. J., The effect of water adsorption on the structure of the carboxylate containing metal-organic frameworks Cu-BTC, Mg-MOF-74, and UiO-66. *J. Mater. Chem. A* **2013,** *1* (38), 11922-11932.

(20) Ma, D. Y.; Li, Y. W.; Li, Z., Tuning the moisture stability of metal-organic frameworks by incorporating hydrophobic functional groups at different positions of ligands. *Chem. Commun.* **2011,** *47* (26), 7377-7379.

(21) Chevreau, H.; Devic, T.; Salles, F.; Maurin, G.; Stock, N.; Serre, C., Mixed-Linker Hybrid Superpolyhedra for the Production of a Series of Large-Pore Iron(III) Carboxylate Metal-Organic Frameworks. *Angew. Chem. Int. Ed.* **2013,** *52* (19), 5056-5060.

(22) Nguyen, J. G.; Cohen, S. M., Moisture-Resistant and Superhydrophobic Metal-Organic Frameworks Obtained via Postsynthetic Modification. *J. Am. Chem. Soc.* **2010,** *132* (13), 4560-4561.

(23) Mounfield, W. P.; Han, C.; Pang, S. H.; Tumuluri, U.; Jiao, Y.; Bhattacharyya, S.; Dutzer, M. R.; Nair, S.; Wu, Z.; Lively, R. P.; Sholl, D. S.; Walton, K. S., Synergistic Effects of Water and SO_2 on Degradation of MIL-125 in the Presence of Acid Gases. *J. Phys. Chem. C* **2016,** *120* (48), 27230-27240.

(24) Park, K. S.; Ni, Z.; Cote, A. P.; Choi, J. Y.; Huang, R. D.; Uribe-Romo, F. J.; Chae, H. K.; O'Keeffe, M.; Yaghi, O. M., Exceptional chemical and thermal stability of zeolitic imidazolate frameworks. *Proc. Natl. Acad. Sci. U.S.A.* **2006,** *103* (27), 10186-10191.

(25) Bhattacharyya, S.; Pang, S. H.; Dutzer, M. R.; Lively, R. P.; Walton, K. S.; Sholl, D. S.; Nair, S., Interactions of SO_2-Containing Acid Gases with ZIF-8: Structural Changes and Mechanistic Investigations. *J. Phys. Chem. C* **2016,** *120* (48), 27221-27229.

(26) Pang, S. H.; Han, C.; Sholl, D. S.; Jones, C. W.; Lively, R. P., Facet-Specific Stability of ZIF-8 in the Presence of Acid Gases Dissolved in Aqueous Solutions. *Chem. Mater.* **2016,** *28* (19), 6960-6967.

(27) Tan, J. C.; Bennett, T. D.; Cheetham, A. K., Chemical structure, network topology, and porosity effects on the mechanical properties of Zeolitic Imidazolate Frameworks. *Proc. Natl. Acad. Sci. U.S.A.* **2010,** *107* (22), 9938-9943.

(28) Zhang, K.; Lively, R. P.; Zhang, C.; Koros, W. J.; Chance, R. R., Investigating the Intrinsic Ethanol/Water Separation Capability of ZIF-8: An Adsorption and Diffusion Study. *J. Phys. Chem. C* **2013,** *117* (14), 7214-7225.

(29) Hara, N.; Yoshimune, M.; Negishi, H.; Haraya, K.; Hara, S.; Yamaguchi, T., Diffusive separation of propylene/propane with ZIF-8 membranes. *J. Membr. Sci.* **2014,** *450*, 215-223.

(30) Kwon, H. T.; Jeong, H. K., In Situ Synthesis of Thin Zeolitic-Imidazolate Framework ZIF-8 Membranes Exhibiting Exceptionally High Propylene/Propane Separation. *J. Am. Chem. Soc.* **2013,** *135* (29), 10763-10768.

(31) Salunkhe, R. R.; Young, C.; Tang, J.; Takei, T.; Ide, Y.; Kobayashi, N.; Yamauchi, Y., A high-performance supercapacitor cell based on ZIF-8-derived nanoporous carbon using an organic electrolyte. *Chem. Commun.* **2016,** *52* (26), 4764-4767.

(32) Zhang, P.; Sun, F.; Shen, Z. G.; Cao, D. P., ZIF-derived porous carbon: a promising supercapacitor electrode material. *J. Mater. Chem. A* **2014,** *2* (32), 12873-12880.

(33) Lu, G.; Hupp, J. T., Metal-Organic Frameworks as Sensors: A ZIF-8 Based Fabry-Perot Device as a Selective Sensor for Chemical Vapors and Gases. *J. Am. Chem. Soc.* **2010,** *132* (23), 7832-7833.

(34) Jayachandrababu, K. C.; Bhattacharyya, S.; Chiang, Y. D.; Sholl, D. S.; Nair, S., Recovery of Acid Gas-Degraded Zeolitic Imidazolate Frameworks by Solvent-Assisted Crystal Redemption (SACRed). *ACS Appl. Mater. Interfaces, Article ASAP* **2017**.

(35) Zhang, C.; Han, C.; Sholl, D. S.; Schmidt, J. R., Computational Characterization of Defects in Metal–Organic Frameworks: Spontaneous and Water-Induced Point Defects in ZIF-8. *The Journal of Physical Chemistry Letters* **2016,** *7* (3), 459-464.

(36) Han, R.; Sholl, D. S., Computational Model and Characterization of Stacking Faults in ZIF-8 Polymorphs. *J. Phys. Chem. C* **2016,** *120* (48), 27380-27388.

(37) Chizallet, C.; Bats, N., External Surface of Zeolite Imidazolate Frameworks Viewed Ab Initio: Multifunctionality at the Organic-Inorganic Interface. *J. Phys. Chem. Lett.* **2010,** *1* (1), 349-353.

(38) Gee, J. A.; Sholl, D. S., Characterization of the Thermodynamic Stability of Solvated Metal-Organic Framework Polymorphs Using Molecular Simulations. *J. Phys. Chem. C* **2013,** *117* (40), 20636-20642.

(39) du Bourg, L. B.; Ortiz, A. U.; Boutin, A.; Coudert, F. X., Thermal and mechanical stability of zeolitic imidazolate frameworks polymorphs. *APL Mater.* **2014,** *2* (12), 124110.

(40) Lewis, D. W.; Ruiz-Salvador, A. R.; Gomez, A.; Rodriguez-Albelo, L. M.; Coudert, F. X.; Slater, B.; Cheetham, A. K.; Mellot-Draznieks, C., Zeolitic imidazole frameworks: structural and energetics trends compared with their zeolite analogues. *Crystengcomm* **2009,** *11* (11), 2272-2276.

(41) Akimbekov, Z.; Katsenis, A. D.; Nagabhushana, G. P.; Ayoub, G.; Arhangelskis, M.; Morris, A. J.; Friscic, T.; Navrotsky, A., Experimental and Theoretical Evaluation of the Stability of True MOF Polymorphs Explains Their Mechanochemical Interconversions. *J. Am. Chem. Soc.* **2017,** *139* (23), 7952-7957.

(42) Li, Z. J.; Xiao, Y. L.; Xue, W. J.; Yang, Q. Y.; Zhong, C. L., Ionic Liquid/Metal-Organic Framework Composites for H2S Removal from Natural Gas: A Computational Exploration. *J. Phys. Chem. C* **2015,** *119* (7), 3674-3683.

(43) Howe, J. D.; Liu, Y.; Flores, L.; Dixon, D. A.; Sholl, D. S., Acid Gas Adsorption on Metal-Organic Framework Nanosheets as a Model of an "All-Surface" Material. *J. Chem. Theory Comput.* **2017,** *13* (3), 1341-1350.

(44) Kresse, G.; Hafner, J., Abinitio Molecular-Dynamics for Liquid-Metals. *Phys. Rev. B* **1993,** *47* (1), 558-561.

(45) Kresse, G.; Hafner, J., Ab-Initio Molecular-Dynamics Simulation of the Liquid-Metal Amorphous-Semiconductor Transition in Germanium. *Phys. Rev. B* **1994,** *49* (20), 14251-14269.

(46) Kresse, G.; Furthmuller, J., Efficient iterative schemes for *ab initio* total-energy calculations using a plane-wave basis set. *Phys. Rev. B* **1996,** *54* (16), 11169-11186.

(47) Kresse, G.; Furthmuller, J., Efficiency of *ab-initio* total energy calculations for metals and semiconductors using a plane-wave basis set. *Comput. Mater. Sci.* **1996,** *6* (1), 15-50.

(48) Blöchl, P. E., Projector Augmented-Wave Method. *Phys. Rev. B* **1994,** *50* (24), 17953-17979.

(49) Perdew, J. P.; Burke, K.; Ernzerhof, M., Generalized gradient approximation made simple. *Phys. Rev. Lett.* **1996,** *77* (18), 3865-3868.

(50) Grimme, S.; Antony, J.; Ehrlich, S.; Krieg, H., A consistent and accurate ab initio parametrization of density functional dispersion correction (DFT-D) for the 94 elements H-Pu. *J. Chem. Phys.* **2010,** *132* (15), 154104.

(51) Grimme, S.; Ehrlich, S.; Goerigk, L., Effect of the Damping Function in Dispersion Corrected Density Functional Theory. *J. Comput. Chem.* **2011,** *32* (7), 1456-1465.

(52) Mills, G.; Jonsson, H.; Schenter, G. K., Reversible Work Transition-State Theory - Application to Dissociative Adsorption of Hydrogen. *Surf. Sci.* **1995,** *324* (2-3), 305-337.

(53) Henkelman, G.; Uberuaga, B. P.; Jonsson, H., A climbing image nudged elastic band method for finding saddle points and minimum energy paths. *J. Chem. Phys.* **2000,** *113* (22), 9901-9904.

(54) Henkelman, G.; Jonsson, H., Improved tangent estimate in the nudged elastic band method for finding minimum energy paths and saddle points. *J. Chem. Phys.* **2000,** *113* (22), 9978-9985.

(55) Baburin, I. A.; Leoni, S., The energy landscapes of zeolitic imidazolate frameworks (ZIFs): towards quantifying the presence of substituents on the imidazole ring. *J. Mater. Chem.* **2012,** *22* (20), 10152-10154.

(56) Lo, Y.; Lam, C. H.; Chang, C. W.; Yang, A. C.; Kang, D. Y., Polymorphism/pseudopolymorphism of metalorganic frameworks composed of zinc(II) and 2methylimidazole: synthesis, stability, and application in gas storage. *RSC Adv.* **2016,** *6* (92), 89148-89156.

(57) Bartmess, J. E., "Negative Ion Energetics Data" in NIST Chemistry WebBook, NIST Standard Reference Database Number 69, Eds. P.J. Linstrom and W.G. Mallard, National Institute of Standards and Technology, Gaithersburg MD, 20899. **2017**.

(58) "DISSOCIATION CONSTANTS OF INORGANIC ACIDS AND BASES". In *CRC Handbook of Chemistry and Physics,* Internet Version 2005; Lide, D. R., Ed.; CRC Press: Boca Raton, FL, 2005; http://www.hbcpnetbase.com/.

(59) Zhang, H. F.; Liu, D. F.; Yao, Y.; Zhang, B. Q.; Lin, Y. S., Stability of ZIF-8 membranes and crystalline powders in water at room temperature. *J. Membr. Sci.* **2015,** *485*, 103-111.

(60) T. W. Graham Solomons, C. B. F., Scott Snyder, *Organic Chemistry*. 11 ed.; Wiley: 2012.

(61) Zhang, C.; Gee, J. A.; Sholl, D. S.; Lively, R. P., Crystal-Size-Dependent Structural Transitions in Nanoporous Crystals: Adsorption-Induced Transitions in ZIF-8. *J. Phys. Chem. C* **2014,** *118* (35), 20727-20733.

(62) Haque, E.; Lo, V.; Minett, A. I.; Harris, A. T.; Church, T. L., Dichotomous adsorption behaviour of dyes on an amino-functionalised metal-organic framework, amino-MIL-101(Al). *J. Mater. Chem. A* **2014,** *2* (1), 193-203.

(63) Wu, C. S.; Xiong, Z. H.; Li, C.; Zhang, J. M., Zeolitic imidazolate metal organic framework ZIF-8 with ultra-high adsorption capacity bound tetracycline in aqueous solution. *RSC Adv.* **2015,** *5* (100), 82127-82137.

(64) Bae, Y. S.; Snurr, R. Q., Development and Evaluation of Porous Materials for Carbon Dioxide Separation and Capture. *Angew. Chem. Int. Ed.* **2011,** *50* (49), 11586-11596.

(65) Lee, J.; Farha, O. K.; Roberts, J.; Scheidt, K. A.; Nguyen, S. T.; Hupp, J. T., Metal-organic framework materials as catalysts. *Chem. Soc. Rev.* **2009,** *38* (5), 1450-1459.

(66) Kim, H. K.; Yun, W. S.; Kim, M. B.; Kim, J. Y.; Bae, Y. S.; Lee, J.; Jeong, N. C., A Chemical Route to Activation of Open Metal Sites in the Copper-Based Metal-Organic Framework Materials HKUST-1 and Cu-MOF-2. *J. Am. Chem. Soc.* **2015,** *137* (31), 10009-10015.

CHAPTER 5

ASSESSING THE IMPACT OF POINT DEFECTS ON MOLECULAR DIFFUSION IN ZIF-8 USING MOLECULAR SIMULATIONS*

5.1 Introduction

Gas separation and purification is traditionally an energy-intensive process based on methods such as distillation.[1] To develop less energy-intensive separation processes, techniques exploiting porous materials such as zeolites, activated carbon, and metal-organic frameworks (MOFs) have been widely studied.[2-4] Gas separation in porous materials can be achieved by methods exploiting molecular sieving by size-exclusion, differences in equilibrium adsorption, or kinetic separation. Molecular sieving occurs when certain components in a gas mixture are prohibited from entering pores of an adsorbent due to size/shape exclusion. Absolute ethylene/ethane separation was achieved in silver-exchanged zeolite A, for which the pore size falls between the kinetic diameters of the two adsorbate molecules.[5] Propylene/propane separation was realized in a pillar-structured MOF (KAUST-7) by replacing the $(SiF6)^{2-}$ pillar with a bulkier $(NbOF_5)^{2-}$ one, which effectively reduced the aperture opening by tilting the pyrazine molecule on the linker.[6] Thermodynamic equilibrium separations take advantage of the difference in adsorption affinity of different gas components in an adsorbent. When the adsorption strength does not strongly distinguish between adsorbates, kinetic separation, which relies

* Portions of this chapter have been published previously in article "Assessing the Impact of Point Defects on Molecular Diffusion In ZIF-8 Using Molecular Simulations" by Chu Han, Ross Verploegh, and David Sholl in the *Journal of Physical Chemistry Letters*, 2018, volume 9, issue 14, pages 4037—4044.

on differences in the diffusion rates of adsorbing components, can be considered. To give just one example, propane and propene have almost identical adsorption capacities but different diffusion coefficients in ZIF-8.[7] This has made it possible to develop ZIF-8 membranes that are selective to propane/propene permeation.[8]

With versatile structures, tunable pore sizes, and large surface areas, MOFs are attractive adsorbents for chemical separations. ZIF-8 has been widely studied because of its relatively high thermal and chemical stability,[9] facile synthesis,[10] and scalable preparation.[11] Kinetic separation has been extensively studied in ZIF-8 both experimentally and computationally. Bux *et al.*[12] synthesized a ZIF-8 membrane with a microwave-assisted solvothermal process and investigated the selectivity for H_2 with respect to CO_2, O_2, N_2, and CH_4. The high separation factor between CH_4 and H_2 found in Bux *et al.*'s study was further investigated by computational simulations. Hertag *et al.*[13] performed molecular dynamics simulations to calculate the self-diffusivities of CH_4 and H_2 with flexible ZIF-8 models using several sets of force field parameters. They found that the flexibility was a crucial factor to describe the diffusion of methane in ZIF-8. The framework flexibility of ZIF-8 makes the effective aperture size larger than the XRD-derived pore size, so ZIF-8 can be used to separate C4 hydrocarbons such as n-C_4H_{10} and iso-C_4H_{10}, which have kinetic diameters large than the pore diameter determined directly from the XRD structure.[14] Separations of other mixtures, including ethene/ethane[15], propene/propane,[7] propylene/propane,[16-19] ethanol/water,[20] have also been studied in ZIF-8 experimentally. The characteristics of molecular diffusion in ZIF-8 have also been widely investigated by computational simulations. For example, Verploegh *et al.*[21] reported molecular simulations using transition-state theory methods

examining self-diffusivity of 15 adsorbate species as a function of temperature and loading. Their results showed excellent agreement with experimental results. This work has recently been extended to diffusion of molecules in hybrid ZIFs that are closely related to ZIF-8.[22-23] Krokidas *et al.*[24] developed a set of force field parameters that combined the AMBER force field and parameters derived from *ab initio* calculations that predicted propane/propylene separation with high accuracy and good agreement with experimental results.

All previous modeling studies of molecular diffusion in ZIF-8 were conducted under the assumption that ZIF-8 is a defect-free crystal. However, as with all materials, ZIF-8 crystals are likely to contain defects due either to their synthesis conditions[25] or to form defects because of reactions with surrounding molecules such as water or acid gases.[26-28] Computational studies have provided atomistic insights into the formation of such defects, particularly the defects that are expected to arise in ZIF-8 under humid acidic conditions.[29-30] Defects in MOFs may enhance or hinder their separation potential in certain applications.[31] The influence of defects on gas adsorption and separation has only been investigated in a limited range of MOFs. For example, missing-linker defects that were deliberately introduced into UiO-66 have been shown to enhance the separation performance for large molecules by increasing the aperture size while the crystal retained its chemical and thermal stability.[32] Heinke *et al.* observed significant mass transfer resistances associated with uptake of adsorbates in HKUST-1. They interpreted these resistances as arising from "surface barriers" caused by blocked pores associated with degradation of the crystal surfaces by water.[33] Lee *et al*. reported the time-dependent selectivity of propylene of ZIF-8 membranes prepared by CD and MW methods.[34] They

found that the propylene permeance of the CD-ZIF-8 membrane dropped by ~75% of its initial value after 60 days of off-stream measurement, an observation attributed to defects formed in the membrane.

The ubiquitous presence of defects in MOFs such as ZIF-8 implies that it is important to understand whether these defects will play a strong role in the material's performance. In this study, we present the first examination of the impact of experimentally-relevant point defects on molecular diffusion in ZIF-8. The general classification of defects that can exist in MOFs is well known from extensive previous work on zeolites.[31] In zeolites, both point defects and extended defects such as grain boundaries have been characterized. Although there is evidence that extended defects are likely to exist in some framework topologies that are accessible as ZIFs,[35] there is no indication to date that these kinds of defects are common in the SOD topology in which ZIF-8 forms. We therefore focus entirely on point defects.

The point defects we consider are dangling linker and linker vacancies induced by water molecules, which are formed by a water molecule inserting into a Zn-N bond and a water molecule together with an OH group replacing a mIM ligand, respectively (Figure 5.1). These types of point defects have been examined by previous computational studies, which suggested the thermodynamic plausibility of their formation under ambient conditions.[29] The relevant defect structures were also inferred to exist experimentally in ZIF-8 structures after exposure to humid acidic environments.[26] Although here we focus on the point defects induced by water, we expect our methods would be transferable to the same types of point defects induced by other species.[30]

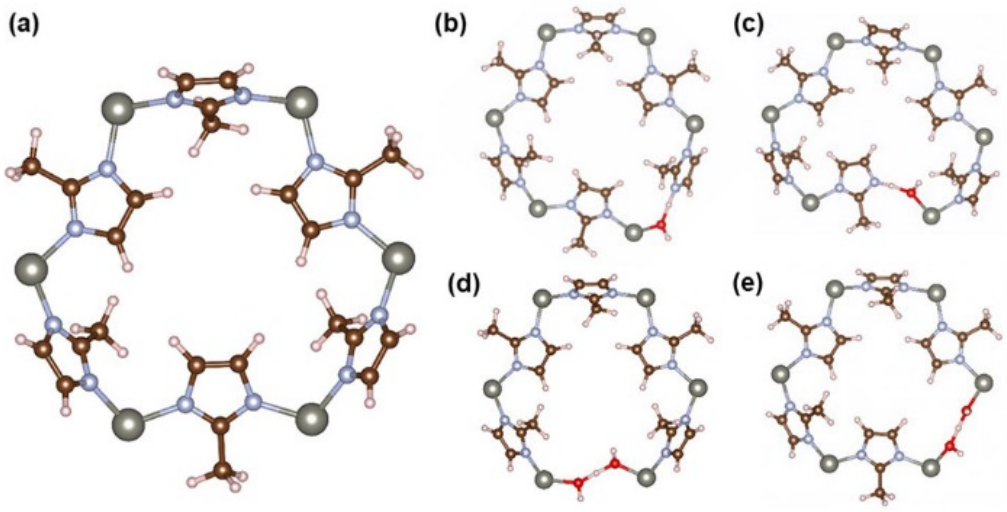

Figure 5.1 DFT-optimized structures of (a) pristine and (b—e) defective ZIF-8 6-member-ring windows. Each of the defective windows contains (b—c) a dangling linker or (d—e) a linker vacancy. C, H, N, O, and Zn atoms are represented by brown, white, blue, red, and grey balls. DFT optimization was performed with a periodic ZIF-8 structure, but only a single 6-member-ring is shown for clarity.

5.2 Computational Methods

5.2.1 Flexible Force Field for Defective ZIF-8 Structures

A set of flexible force field (FF) parameters developed by Zhang *et al*.[36] was used to describe ZIF-8 in our simulations. To the best of our knowledge, there is no reported FF appropriate for describing point defects in ZIF-8. The defective structures involve more atom types (e.g. oxygen), bonds (e.g. Zn-O), angles (e.g. H-O-H), and torsion types (e.g. H-C-N-H in dangling linker) than pristine ZIF-8. Instead of developing a special set of FF parameters for defective structures from scratch, we adopted existing parameters from a variety of resources to model components of a point defect. Specifically, a combination of general AMBER FF (GAFF)[37-38] parameters, FF parameters of other MOFs with similar local geometries,[39-40] and parameters from a FF for pristine ZIF-8[36]

were used to describe bonded interactions, UFF parameters[41] were used for non-bonded interactions, and DDEC charges[42] were used for the atomic charges in defective structures. The Zn-O-H angles in both dangling linkers and linker vacancies were kept rigid at the values of their energy minimized structures optimized by density functional theory (DFT) calculations because we did not have appropriate FF parameters for these angles. Approximating these degrees of freedom as rigid reduces the flexibility of windows, so our method should be viewed as giving a lower bound for diffusive hopping rates that are influenced by framework flexibility. It will be seen below that this approximation does not affect the key conclusions of our calculations. More details about DFT calculations and the FF used in our calculations are included in Appendix C.

5.2.2 Force Fields for Adsorbates

The TraPPE united atom FF was adopted to describe adsorbate-adsorbate interactions for methane, ethane, propane, n-butane, and isobutane.[43] With this approach, the bonds and angles of all the five species are flexible and united atoms have no charge. H_2S was modeled as a three-site model where the S atom is a Lennard-Jones (LJ) site while partial charges are centered on each atom. The H-S bond length is fixed at 1.34 Å and the H-S-H angle is flexible with an equilibrium angle of 92.5°.[44] SO_2 was modeled as a three-site LJ model with fixed S-O bond length of 1.432 Å and flexible O-S-O angle with an equilibrium angle of 119.3°.[45] H_2O was described by the rigid simple point-charge (SPC) model with a fixed O-H bond length of 1.00 Å and a fixed H-O-H angle of 109.47°.[40] CO_2 was described by the rigid EPM2 FF with a fixed bond length of 1.16 Å.[46] NO and NO_2 were described by two- and three-site LJ models, respectively, with partial charges assigned on each site.[47] NO has a fixed N-O bond length of 1.15 Å, while NO_2

has a fixed N-O bond length of 1.20 Å and a fixed O-N-O angle of 134.3°. All adsorbate FF parameters can be found in Appendix C. With the adsorbate-adsorbate and framework FFs defined as just described, adsorbate-framework interactions were modeled using LJ interactions defined via Lorentz-Berthelot mixing rules. This relatively common strategy for modeling molecular adsorption in MOFs has been shown to give good agreement with experimental data for CO_2 physisorption in MOFs for which detailed analysis of the literature identified enough experiments to assess experimental reproducibility.[48] To date, a similar analysis is not available for other molecular adsorbates.

5.2.3 Transition State Theory Methods

Adsorbates with kinetic diameters similar to or greater than the ZIF-8 window diameter experience a relatively high activation energy to jump through a window.[21] Therefore, intracrystalline adsorbate diffusion in ZIF-8 can be characterized by an uncorrelated sequence of molecular hops through the 6-member-ring (6MR) windows that connect two identical cages. Due to the symmetry of ZIF-8 about the [111] direction, which is perpendicular to the planes of 6MR windows, the movement for a molecule through a 6MR window can be described by a one-dimensional reaction coordinate (RC) connecting the center of one cage to that of its neighboring cage.[21] As in our earlier work,[21] we used dynamically corrected Transition State Theory (dcTST) to determine hopping rates along this reaction coordinate. Specifically, umbrella sampling[49] is used to explore the energy landscape of an adsorbate moving along a specific RC. The hopping rate for an adsorbate from cage A to cage B, $k_{A\to B}$, is calculated by

$$k_{A\to B} = \kappa \frac{1}{\sqrt{2\beta\pi m}} \frac{e^{-\beta F^*}}{\int_{state\ A} e^{-\beta F(r)} dr}, \tag{5.1}$$

where $\beta = 1/k_B T$, m is the mass of an adsorbate, $F(r)$ is the Helmholtz free energy profile along the RC, and F^* is the activation energy, taken as the maximum value of $F(r)$. κ is a dynamical correction factor, which accounts for short-time recrossings of the TS. κ is close to 1 for fast-diffusing adsorbates and can be as much as several orders of magnitude below 1 for the slow-diffusing species.[21]

5.3 Results and Discussion

5.3.1 Self-Diffusion Coefficients of Adsorbates in Pristine ZIF-8

We applied dcTST to calculate the hopping rates of eleven adsorbates through pristine and defective ZIF-8 windows at 35 ^{o}C. All the MD simulations in this study were performed by LAMMPS[50] using a 2×2×2 ZIF-8 supercell (2208 atoms for the pristine material) with periodic boundary conditions. In all calculations Ewald summation was used to calculate Coulombic interactions with a relative accuracy of 10^{-6}. The pristine ZIF-8 crystal structure was energy-minimized optimized starting from the experimental XRD structure.[9] During geometry optimization, lattice parameters and atom positions are fully relaxed by a Polak-Ribiere conjugate gradient algorithm. This gave a lattice constant of 16.943 Å. To simulate low defect concentrations, only one point defect was included in a ZIF-8 supercell by replacing a single mIM ligand. Each defective supercell was energy-minimized allowing the atomic positions and lattice parameters to relax. The lattice constant of a 2×2×2 defective ZIF-8 supercell was 34.053 Å. Umbrella sampling simulations are performed using the collective variables package[51] in LAMMPS with umbrella spacing of 0.25 Å along the RC. During an umbrella sampling simulation, an adsorbate was constrained in a 3-D region (umbrella) orthogonal to the reaction

coordinate by a spring centered at a specified value of the reaction coordinate. A spring of spring constant ranging from 10 to 25 kcal mol^{-1} $Å^{-1}$ was applied on an adsorbate molecule, where a stiffer spring was applied to a molecule with higher molecular weight. Equilibrium MD (EMD) simulations were performed in the NVT ensemble using the velocity-Verlet integration algorithm with a time step of 1 fs. For each umbrella, a 100 ps equilibration was performed followed by a 500 ps production period. The weighted histogram analysis method was used to integrate the sampling of all the umbrellas into a free energy curve.[52] Dynamical correction factors were calculated in the similar way to our previous work.[21] After the position of the TS was determined, a set of configurations were generated by constraining the adsorbate in the plane of the TS orthogonal to the reaction coordinate with a tight spring of spring constant 1000 kcal mol^{-1} $Å^{-1}$. A set of trajectories for the adsorbate were then simulated starting from these configurations, with no constraints on the adsorbate, with all atoms including adsorbate and framework initially assigned randomized velocities according to the Maxwell-Boltzmann distribution. 1000 trajectories for each adsorbate were recorded and each trajectory was run for 3 ps forward and 3 ps backward in time to allow calculation of dynamical correction factors.

The calculated self-diffusion coefficients of adsorbates in pristine ZIF-8 are shown in Table 1. All five of the hydrocarbons we examined and the acid gases H_2S, SO_2, and NO_2 have kinetic diameters larger than ZIF-8's nominal pore size, which would prohibit them from diffusing in a rigid ZIF-8 framework. This is an example of the observation made in multiple previous studies that including framework flexibility is vital

in quantitatively describing hopping of tight fitting molecules in nanopores.[53-56] The self-diffusion coefficients are given by[21]

$$D_{self} = \frac{1}{6}\left(\sum_{i=1}^{n} k_{A\to B,i}\right)\lambda^2, \tag{5.2}$$

where λ is the distance between low energy states, *n* is the number of windows of a cage (8 for ZIF-8), and $k_{A\to B,i}$ is the hopping rate of the adsorbate hopping through window *i*. The calculated self-diffusion coefficients of CH_4, C_2H_6, C_3H_8, n-C_4H_{10}, iso-C_4H_{10} and CO_2 show a good agreement with the values reported by Verploegh *et al.*,[21] as listed in Table 5.1. The loading of adsorbates in simulations is approximately 0.045 mmol/g (1 molecule/8 unit cells). We therefore compared our calculated self-diffusion coefficients of CH_4, C_2H_6, C_3H_8, n-C_4H_{10}, iso-C_4H_{10}, and CO_2 to experimental corrected diffusivities because the values of corrected diffusivities equal self-diffusion coefficients at infinite dilution.[57] The calculated self-diffusion coefficients are in good agreement with experimental results except for iso-C_4H_{10}.For iso-C_4H_{10}, the two available experimental results differ by ~3 orders of magnitude, and the calculated value lies between the two experiments.

Table 5.1 Kinetic diameters, free energy barrier (E_b), calculated and measured self-diffusion coefficients of investigated adsorbates in pristine ZIF-8.

Adsorbate	Kinetic diameter (Å)	E_b (kJ/mol)	D_{self} (cm^2/s)	$D_{self,\ compt.}$ (cm^2/s)[21]	$D_{self,\ expt.}$ (cm^2/s)
CH_4	3.8[21]	24.9	2.76×10^{-7}	2.79×10^{-7}	$(4.0\pm0.4)\times10^{-7}$ [14]
C_2H_6	4.4[21]	31.7	1.94×10^{-8}	2.36×10^{-8}	$(8.8\pm2.7)\times10^{-8}$ [14]
C_3H_8	4.3[21]	42.4	1.27×10^{-10}	1.38×10^{-10}	$(1.7\pm0.8)\times10^{-10}$ [14]
n-C_4H_{10}	4.3[21]	43.3	1.00×10^{-10}	9.53×10^{-11}	5.7×10^{-12} [14], $(1.5\pm0.3)\times10^{-10}$ [58]
iso-C_4H_{10}	4.8[21]	70.0	2.70×10^{-16}	1.36×10^{-16}	$(3\pm1)\times10^{-15}$ [58], 2.3×10^{-18} [14]
H_2O	2.65[59]	14.2	2.50×10^{-5}		$\sim10^{-6}$ [60]
CO_2	3.3[59]	19.9	1.86×10^{-6}	2.63×10^{-6}	$(2.1\pm0.5)\times10^{-6}$ [14]
H_2S	3.6[61]	25.9	1.70×10^{-7}		
SO_2	3.6[62]	25.4	1.23×10^{-7}		
NO_2	5.12[63]	18.9	1.99×10^{-6}		
NO	3.17[61]	17.0	6.03×10^{-6}		

5.3.2 Hopping Rates of Adsorbates Through Defective ZIF-8 Windows

The hopping rates of the adsorbates were then calculated for defective windows. Because there are two orientations of mIM ligands with respect to the reaction coordinate, two distinct defective window structures exist depending on the orientation for the replaced ligand (see Figure 5.1b—e). The hopping rates of each molecule through defective and pristine windows is compared in Figure 5.2. In every case, hopping through the defective windows is faster than for the pristine window, often by several orders of magnitude. The fastest hopping rates were observed for the windows shown in Figures 5.1d and 5.1b, whose structures are severely deformed from the pristine window structure. The calculated free energy barriers, transmission coefficients, and hopping rates for the studied adsorbates in pristine and defective ZIF-8 are listed in Tables C.4, C.5, and C.6, respectively.

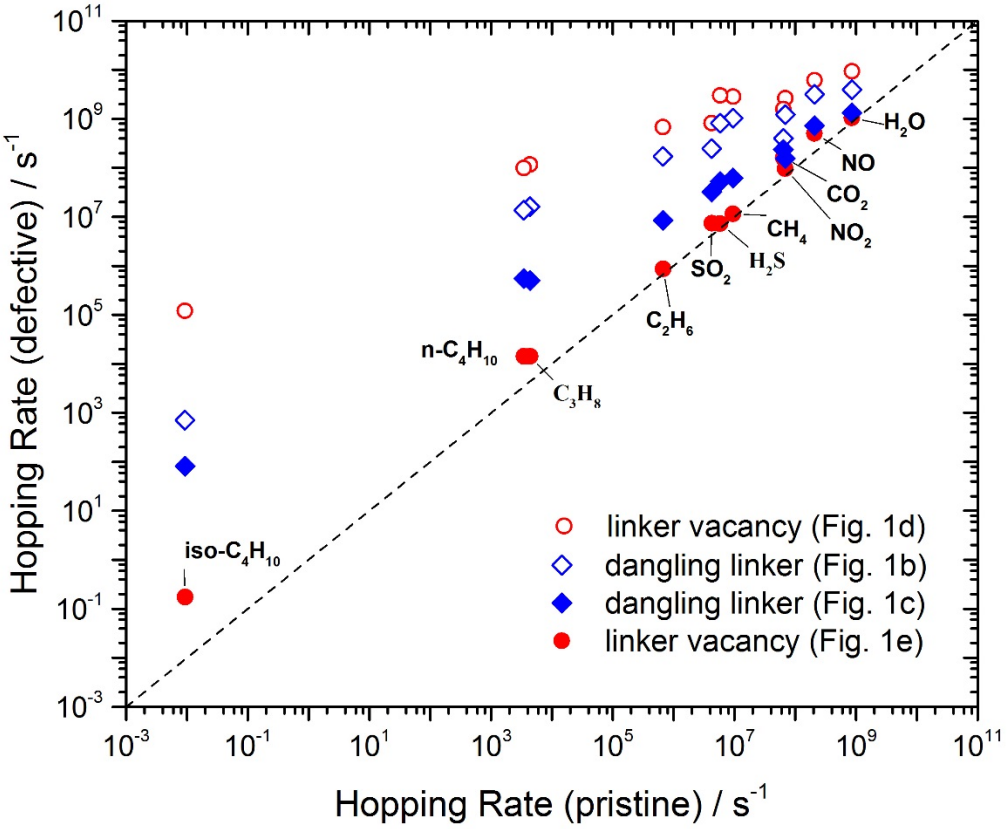

Figure 5.2 Hopping rates (vertical axis) of H_2O, NO, CO_2, NO_2, CH_4, H_2S, SO_2, C_2H_6, C_3H_8, n-C_4H_{10}, iso-C_4H_{10} through the defective ZIF-8 6-member-ring windows shown in Figure 5.1 plotted as a function of their hopping rates through a pristine ZIF-8 window (horizontal axis) at room temperature at infinite dilution.

To understand how the geometry and flexibility of the windows relate to the variation in hopping rates, we calculated the distribution of window diameters of the pristine and defective windows shown in Figure 5.1 using the grid based percolation method of Haldoupis *et al.*[64] In each case, window diameter histograms were calculated using snapshots of ZIF-8 frameworks (with no adsorbates) taken every 0.2 ps over a 200 ps EMD simulation. The calculated average window diameter for a pristine ZIF-8 window is 3.44 ± 0.17 Å. The calculated average window diameters for the defective

windows are 3.95 ± 0.22, 3.32 ± 0.32, 3.91 ± 0.24, and 3.89 ± 0.23 Å for the windows shown in Figures 5.1b, 5.1c, 5.1d, and 5.1e respectively (Figure C.2). It is notable that the structure shown in Figure 5.1c has a smaller average window diameter than pristine window, even though the hopping rates of molecules through the defective structure are higher than through the pristine window. This outcome seems less surprising considering that the standard deviation in the window size of the defective window (0.32 Å) is considerably larger than for the pristine window (0.17 Å). The kinetic diameters of most of the molecules we considered are larger than the average window diameters of any of the windows we modeled, so the ability of the flexible windows to reach configurations that allow these molecules to pass is vital to allowing molecular diffusion. Although information from the window diameter distribution for the window in the absence of adsorbates can give only incomplete information, the observations above hint that the extra flexibility available to defective windows is crucial in enabling the faster molecular hopping rates that we observe relative to defect-free ZIF-8.

The results above suggest a simple way to look at the effect of defects in ZIF-8 on molecular diffusion, namely that the defects we examined always increase the local hopping rates of molecules. This outcome appears to contradict previous descriptions of defects in nanoporous materials where defects were inferred to offer additional resistance to diffusion.[33-34] In these previous studies, the observed resistance was attributed to the blockage of pores as well as the interaction between adsorbates and defects or the byproducts of defects. This led us to reconsider the linker vacancy defects described above, in particular, to assess the fate of the linker that is released from the ZIF when these defects are formed. The formation of a linker vacancy in ZIF-8 involves removal of

a mIM ligand, which then forms a neutral molecule, HmIM, by bonding to a proton. Preliminary force field-based free energy calculations analogous to those described above gave an activation energy for HmIM in ZIF-8 of ~50 kJ/mol, suggesting that the rate at which this molecule can diffuse away from the linker vacancy at which it originates may be slow.

5.3.3 The Role of Trapped 2-Methylimidazole by a Linker Vacancy on Molecular Hopping Rates

To further probe the role of HmIM in the vicinity of a linker vacancy, we performed DFT calculations to examine the binding energy of a single HmIM molecule to several sites in the cage including those close to the linker vacancy in a ZIF-8 unit cell. The most thermodynamically favorable site is close to the linker vacancy and window center (Figure 5.3a). This finding is reminiscent of the window blocking effect caused by K^+ ions in zeolite A, where a large K^+ ion sits in the center of the 8MR window, effectively prohibiting CO_2 and N_2 from passing a 8MR window.[65] To understand the impact of this molecule on the hopping of other molecules, we need to include HmIM in our force field-based calculations. Our DFT calculations indicate that HmIM is exothermically adsorbed to the linker vacancy site with an adsorption energy of ~77 kJ/mol (relative to the gas phase). We found that applying the force fields described above did not adequately approximate the strong localization of the molecule seen in our DFT calculations. To include this effect, the HmIM molecule was coupled with the defect by a harmonic oscillator spring. The displacement of the harmonic oscillator was defined as the distance between the centers of mass of the HmIM molecule and the linker vacancy (H_3O_2), with the equilibrium position corresponding to the configuration

optimized by DFT calculations. One way to approximate the vibrational frequency of the harmonic oscillator is by using the translational modes of HmIM molecule at its lowest energy state structure in Figure 5.3a. The three DFT-calculated translational modes are 83.6, 73.1, and 39.2 cm^{-1}, which correspond to spring constants, K, of 48.7, 37.2, and 10.7 $kcal \cdot mol^{-1} \cdot Å^{-2}$, respectively.

To examine the impact of a trapped HmIM molecule on diffusion of other molecules, we calculated the hopping rate of H_2S and isobutane through windows similar to the one shown in Figure 5.3a. Figure 5.3b shows the free energy barrier and associated hopping rates of H_2S and isobutane as a function of the spring constant constraining HmIM to be near the linker vacancy. Higher values of K value allow less freedom for HmIM to move away from its equilibrium position close to window center, so it is not surprising that these values are associated with lower hopping rates for H_2S and isobutane. The HmIM molecule reduces the local hopping rates of these two species by multiple orders of magnitude relative to the linker vacancy when no HmIM is present. Critically, however, the hopping rates in the presence of HmIM, even when using the stiffest reasonable spring constants to constrain this "blocking" molecule, are only ~1 order of magnitude less than the hopping rates in pristine ZIF-8. The calculated free energy profiles of H_2S and isobutane in the presence of HmIM are shown in Figure C.4, with their free energy barriers and hooping rates listed in Table C.7.

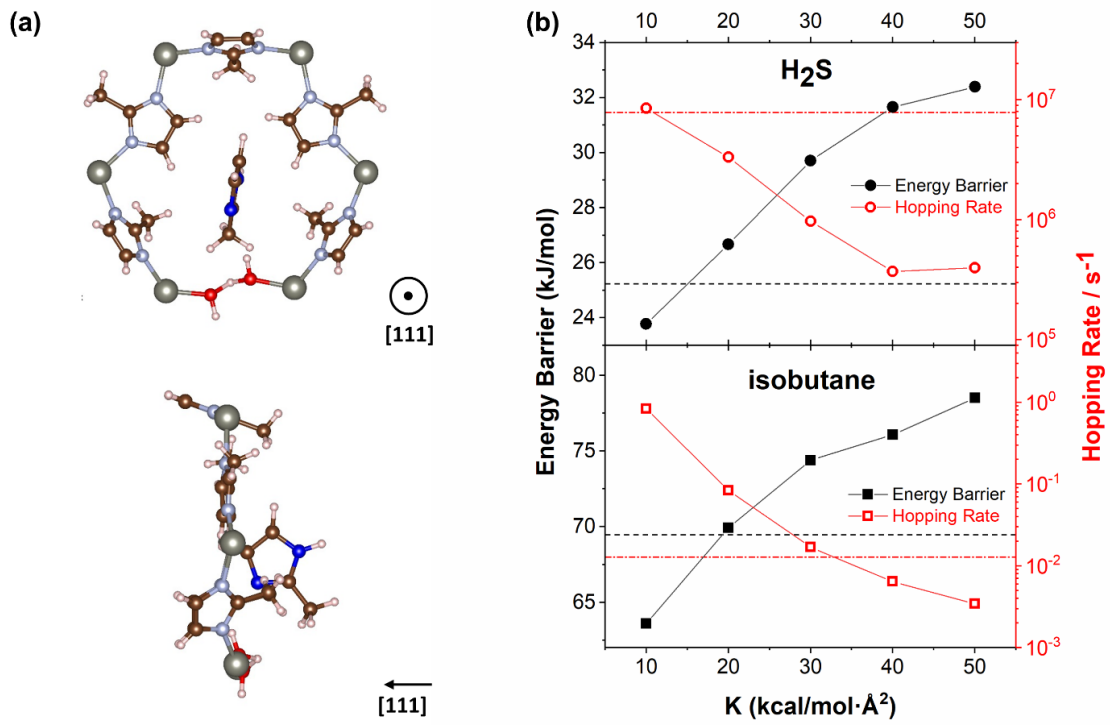

Figure 5.3 (a) DFT-optimized structure of a ZIF-8 6-member ring window with a linker vacancy (Figure 5.2d) adsorbing a 2-methylimidazole (HmIM) molecule in front view (top) and side view (bottom). Zn, C, H, and O atoms are represented by grey, brown, white, and red balls, respectively. The N atoms of ZIF-8 and those of HmIM are shown by blue and dark blue balls, respectively. (b) Free energy barrier (left vertical axis) and corresponding hopping rates (right vertical axis) of H_2S and isobutane hopping though the window shown in (a). The window and the HmIM are coupled by a spring with spring constant K (horizontal axis) in MD simulations. The diffusion energy barriers and hopping rates for the adsorbates hopping through a pristine window are labeled by the black dashed lines and red dot dashed lines, respectively.

5.3.4 The Impact of Defects on Long-Range Diffusion

The discussion above has focused on the local hopping rates of molecules through defective windows in ZIF-8. To consider the influence of these windows on long-range diffusion, it is useful to draw an analogy with molecular diffusion in mixed-linker ZIFs, a topic we have examined previously using lattice models and atomistic simulations.[22-23] Consistent with what might be expected qualitatively from percolation theory, the

influence of a low density of defective windows on diffusion in the 3D pore structure of ZIF-8 will be small. A possible exception to this outcome could arise if the defective sites strongly pin adsorbates, a scenario that would lead to strongly reduced diffusion at very low adsorbate concentrations and a rapid increase in diffusion rates as the adsorbate loading is increased.[66] To determine if this scenario was relevant, we computed the free energy profiles for SO_2 and H_2O diffusion along extended paths connecting multiple cages in the vicinity of a defective window. The results for SO_2 (H_2O) are shown in Figure 5.4 (Figure C.5). In both cases, it is clear that no pinning of the diffusing molecules in the cages adjacent to the defective windows occurs. These observations suggest that the overall impact of low densities of point defects in ZIF-8 on molecular diffusion in this material will be minimal, an outcome that is useful for efforts to use the diffusion selectivity offered by ZIF-8's pores in applications such as membrane-based separations.

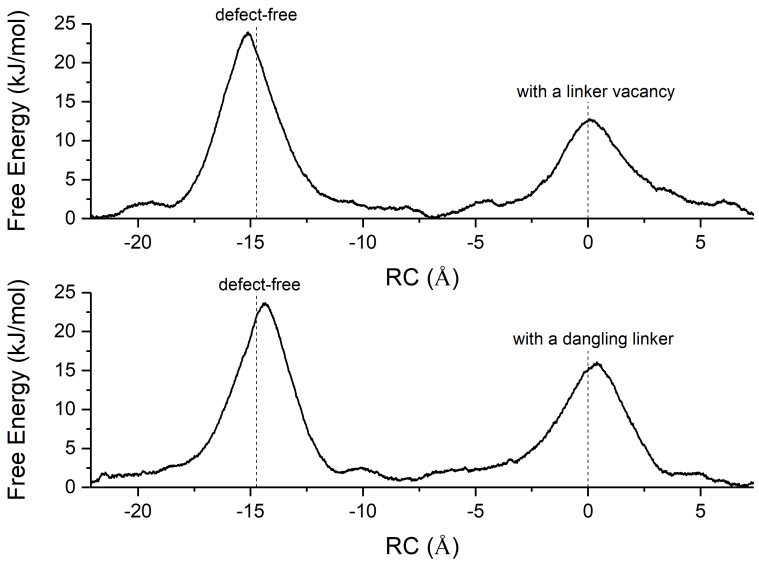

Figure 5.4 Free energy profiles of SO_2 along the [111]-oriented reaction coordinate passing through a defect-free 6MR window and a defective 6MR window. The configurations of the defective windows in top and bottom panels are shown in Figures 5.1d and 5.1b, respectively. Vertical dashed lines label the positions of window centers projected on the reaction coordinate.

5.4 Summary

In summary, we have examined the hopping rates of eleven adsorbates including water, hydrocarbons, and acid gases in pristine and defective ZIF-8 crystals. The local hopping rates are drastically increased through a defective 6MR window for all the adsorbates we investigated. However, the byproducts of forming a point defect such as a linker vacancy can reduce local hopping rates by blocking part of the defective window on the diffusion pathway. Although the impact of these local hopping rates on net diffusion through the 3D pores inside ZIF-8 is small, the effects on diffusion due to defects may be critical in materials with 1D pores or in cases where defects strongly pin adsorbates. The examples shown here are a useful initial exploration of these phenomena and will be useful for future studies assessing the influence of defects on molecular diffusion in MOFs.

5.5 References

(1) Sholl, D. S.; Lively, R. P., Seven chemical separations to change the world. *Nature* **2016,** *532* (7600), 435-437.

(2) Davis, M. E., Ordered porous materials for emerging applications. *Nature* **2002,** *417* (6891), 813-821.

(3) Nugent, P.; Belmabkhout, Y.; Burd, S. D.; Cairns, A. J.; Luebke, R.; Forrest, K.; Pham, T.; Ma, S. Q.; Space, B.; Wojtas, L.; Eddaoudi, M.; Zaworotko, M. J., Porous materials with optimal adsorption thermodynamics and kinetics for CO_2 separation. *Nature* **2013,** *495* (7439), 80-84.

(4) Li, J. R.; Kuppler, R. J.; Zhou, H. C., Selective gas adsorption and separation in metal-organic frameworks. *Chem. Soc. Rev.* **2009,** *38* (5), 1477-1504.

(5) Aguado, S.; Bergeret, G.; Daniel, C.; Farrusseng, D., Absolute Molecular Sieve Separation of Ethylene/Ethane Mixtures with Silver Zeolite A. *J. Am. Chem. Soc.* **2012,** *134* (36), 14635-14637.

(6) Cadiau, A.; Adil, K.; Bhatt, P. M.; Belmabkhout, Y.; Eddaoudi, M., A metal-organic framework-based splitter for separating propylene from propane. *Science* **2016,** *353* (6295), 137-140.

(7) Li, K. H.; Olson, D. H.; Seidel, J.; Emge, T. J.; Gong, H. W.; Zeng, H. P.; Li, J., Zeolitic Imidazolate Frameworks for Kinetic Separation of Propane and Propene. *J. Am. Chem. Soc.* **2009,** *131* (30), 10368-+.

(8) Brown, A. J.; Brunelli, N. A.; Eum, K.; Rashidi, F.; Johnson, J. R.; Koros, W. J.; Jones, C. W.; Nair, S., Interfacial microfluidic processing of metal-organic framework hollow fiber membranes. *Science* **2014,** *345* (6192), 72-75.

(9) Park, K. S.; Ni, Z.; Cote, A. P.; Choi, J. Y.; Huang, R. D.; Uribe-Romo, F. J.; Chae, H. K.; O'Keeffe, M.; Yaghi, O. M., Exceptional chemical and thermal stability of zeolitic imidazolate frameworks. *Proc. Natl. Acad. Sci. U.S.A.* **2006,** *103* (27), 10186-10191.

(10) Pan, Y. C.; Liu, Y. Y.; Zeng, G. F.; Zhao, L.; Lai, Z. P., Rapid synthesis of zeolitic imidazolate framework-8 (ZIF-8) nanocrystals in an aqueous system. *Chem. Commun.* **2011,** *47* (7), 2071-2073.

(11) Zhang, X. F.; Liu, Y. G.; Kong, L. Y.; Liu, H. O.; Qiu, J. S.; Han, W.; Weng, L. T.; Yeung, K. L.; Zhu, W. D., A simple and scalable method for preparing low-defect ZIF-8 tubular membranes. *J. Mater. Chem. A* **2013,** *1* (36), 10635-10638.

(12) Bux, H.; Liang, F. Y.; Li, Y. S.; Cravillon, J.; Wiebcke, M.; Caro, J., Zeolitic Imidazolate Framework Membrane with Molecular Sieving Properties by Microwave-Assisted Solvothermal Synthesis. *J. Am. Chem. Soc.* **2009,** *131* (44), 16000-16001.

(13) Hertag, L.; Bux, H.; Caro, J.; Chmelik, C.; Remsungnen, T.; Knauth, M.; Fritzsche, S., Diffusion of CH_4 and H_2 in ZIF-8. *J. Membr. Sci.* **2011,** *377* (1-2), 36-41.

(14) Zhang, C.; Lively, R. P.; Zhang, K.; Johnson, J. R.; Karvan, O.; Koros, W. J., Unexpected Molecular Sieving Properties of Zeolitic Imidazolate Framework-8. *J. Phys. Chem. Lett.* **2012,** *3* (16), 2130-2134.

(15) Bux, H.; Chmelik, C.; Krishna, R.; Caro, J., Ethene/ethane separation by the MOF membrane ZIF-8: Molecular correlation of permeation, adsorption, diffusion. *J. Membr. Sci.* **2011,** *369* (1-2), 284-289.

(16) Pan, Y. C.; Li, T.; Lestari, G.; Lai, Z. P., Effective separation of propylene/propane binary mixtures by ZIF-8 membranes. *J. Membr. Sci.* **2012,** *390*, 93-98.

(17) Kwon, H. T.; Jeong, H. K., In Situ Synthesis of Thin Zeolitic-Imidazolate Framework ZIF-8 Membranes Exhibiting Exceptionally High Propylene/Propane Separation. *J. Am. Chem. Soc.* **2013,** *135* (29), 10763-10768.

(18) Liu, D. F.; Ma, X. L.; Xi, H. X.; Lin, Y. S., Gas transport properties and propylene/propane separation characteristics of ZIF-8 membranes. *J. Membr. Sci.* **2014,** *451*, 85-93.

(19) Hara, N.; Yoshimune, M.; Negishi, H.; Haraya, K.; Hara, S.; Yamaguchi, T., Diffusive separation of propylene/propane with ZIF-8 membranes. *J. Membr. Sci.* **2014,** *450*, 215-223.

(20) Zhang, K.; Lively, R. P.; Zhang, C.; Koros, W. J.; Chance, R. R., Investigating the Intrinsic Ethanol/Water Separation Capability of ZIF-8: An Adsorption and Diffusion Study. *J. Phys. Chem. C* **2013,** *117* (14), 7214-7225.

(21) Verploegh, R. J.; Nair, S.; Sholl, D. S., Temperature and Loading-Dependent Diffusion of Light Hydrocarbons in ZIF-8 as Predicted Through Fully Flexible Molecular Simulations. *J. Am. Chem. Soc.* **2015,** *137* (50), 15760-15771.

(22) Verploegh, R. J.; Wu, Y.; Sholl, D. S., Lattice-Gas Modeling of Adsorbate Diffusion in Mixed-Linker Zeolitic Imidazolate Frameworks: Effect of Local Imidazolate Ordering. *Langmuir* **2017,** *33* (26), 6481-6491.

(23) Verploegh, R. J.; Wu, Y.; Boulfelfel, S. E.; Sholl, D. S., Quantitative Predictions of Molecular Diffusion in Binary Mixed-Linker Zeolitic Imidazolate Frameworks Using Molecular Simulations. *J. Phys. Chem. C* **2018,** *122* (10), 5627-5638.

(24) Krokidas, P.; Castier, M.; Moncho, S.; Brothers, E.; Economou, I. G., Molecular Simulation Studies of the Diffusion of Methane, Ethane, Propane, and Propylene in ZIF-8. *J. Phys. Chem. C* **2015,** *119* (48), 27028-27037.

(25) Cheetham, A. K.; Bennett, T. D.; Coudert, F. X.; Goodwin, A. L., Defects and disorder in metal organic frameworks. *Dalton Trans.* **2016,** *45* (10), 4113-4126.

(26) Pang, S. H.; Han, C.; Sholl, D. S.; Jones, C. W.; Lively, R. P., Facet-Specific Stability of ZIF-8 in the Presence of Acid Gases Dissolved in Aqueous Solutions. *Chem. Mater.* **2016,** *28* (19), 6960-6967.

(27) Bhattacharyya, S.; Pang, S. H.; Dutzer, M. R.; Lively, R. P.; Walton, K. S.; Sholl, D. S.; Nair, S., Interactions of SO_2-Containing Acid Gases with ZIF-8: Structural Changes and Mechanistic Investigations. *J. Phys. Chem. C* **2016,** *120* (48), 27221-27229.

(28) Jayachandrababu, K. C.; Bhattacharyya, S.; Chiang, Y. D.; Sholl, D. S.; Nair, S., Recovery of Acid-Gas-Degraded Zeolitic Imidazolate Frameworks by Solvent-Assisted Crystal Redemption (SACRed). *ACS Appl. Mater. Interfaces* **2017,** *9* (40), 34597-34602.

(29) Zhang, C.; Han, C.; Sholl, D. S.; Schmidt, J. R., Computational Characterization of Defects in Metal–Organic Frameworks: Spontaneous and Water-Induced Point Defects in ZIF-8. *J. Phys. Chem. Lett.* **2016,** *7* (3), 459-464.

(30) Han, C.; Zhang, C.; Tyminska, N.; Schmidt, J. R.; Sholl, D. S., Insights into the Stability of Zeolitic Imidazolate Frameworks in Humid Acidic Environments from First Principles Calculations. *J. Phys. Chem. C* **2018,** *122* (8), 4339-4348.

(31) Sholl, D. S.; Lively, R. P., Defects in Metal-Organic Frameworks: Challenge or Opportunity? *J. Phys. Chem. Lett.* **2015,** *6* (17), 3437-3444.

(32) Wang, K. K.; Li, C. F.; Liang, Y. X.; Han, T. T.; Huang, H. L.; Yang, Q. Y.; Liu, D. H.; Zhong, C. L., Rational construction of defects in a metal-organic framework for highly efficient adsorption and separation of dyes. *Chem. Eng. J.* **2016,** *289*, 486-493.

(33) Heinke, L.; Gu, Z. G.; Woll, C., The surface barrier phenomenon at the loading of metal-organic frameworks. *Nat. Commun.* **2014,** *5*, 4562.

(34) Lee, M. J.; Kwon, H. T.; Jeong, H. K., Defect-dependent stability of highly propylene-selective zeolitic-imidazolate framework ZIF-8 membranes. *J. Membr. Sci.* **2017,** *529*, 105-113.

(35) Han, R.; Sholl, D. S., Computational Model and Characterization of Stacking Faults in ZIF-8 Polymorphs. *J. Phys. Chem. C* **2016,** *120* (48), 27380-27388.

(36) Zhang, L. L.; Hu, Z. Q.; Jiang, J. W., Sorption-Induced Structural Transition of Zeolitic Imidazolate Framework-8: A Hybrid Molecular Simulation Study. *J. Am. Chem. Soc.* **2013,** *135* (9), 3722-3728.

(37) Wang, J. M.; Wolf, R. M.; Caldwell, J. W.; Kollman, P. A.; Case, D. A., Development and testing of a general amber force field. *J. Comput. Chem.* **2004,** *25* (9), 1157-1174.

(38) Wang, J. M.; Wang, W.; Kollman, P. A.; Case, D. A., Automatic atom type and bond type perception in molecular mechanical calculations. *J. Mol. Graphics Modell.* **2006,** *25* (2), 247-260.

(39) Bureekaew, S.; Amirjalayer, S.; Tafipolsky, M.; Spickermann, C.; Roy, T. K.; Schmid, R., MOF-FF - A flexible first-principles derived force field for metal-organic frameworks. *Phys. Status Solidi B* **2013,** *250* (6), 1128-1141.

(40) Wu, Y. J.; Tepper, H. L.; Voth, G. A., Flexible simple point-charge water model with improved liquid-state properties. *J. Chem. Phys.* **2006,** *124* (2), 024503.

(41) Rappe, A. K.; Casewit, C. J.; Colwell, K. S.; Goddard, W. A.; Skiff, W. M., Uff, a Full Periodic Table Force Field for Molecular Mechanics and Molecular Dynamics Simulations. *J. Am. Chem. Soc.* **1992,** *114* (25), 10024-10035.

(42) Manz, T. A.; Sholl, D. S., Chemically Meaningful Atomic Charges That Reproduce the Electrostatic Potential in Periodic and Nonperiodic Materials. *J. Chem. Theory Comput.* **2010,** *6* (8), 2455-2468.

(43) Martin, M. G.; Siepmann, J. I., Transferable potentials for phase equilibria. 1. United-atom description of *n*-alkanes. *J. Phys. Chem. B* **1998,** *102* (14), 2569-2577.

(44) Kamath, G.; Lubna, N.; Potoff, J. J., Effect of partial charge parametrization on the fluid phase behavior of hydrogen sulfide. *J. Chem. Phys.* **2005,** *123* (12).

(45) Ketko, M. H.; Kamath, G.; Potoff, J. J., Development of an Optimized Intermolecular Potential for Sulfur Dioxide. *J. Phys. Chem. B* **2011,** *115* (17), 4949-4954.

(46) Harris, J. G.; Yung, K. H., Carbon Dioxide's Liquid-Vapor Coexistence Curve and Critical Properties as Predicted by a Simple Molecular-Model. *J. Phys. Chem.* **1995,** *99* (31), 12021-12024.

(47) Sun, W. Z.; Lin, L. C.; Peng, X.; Smit, B., Computational screening of porous metal-organic frameworks and zeolites for the removal of SO_2 and NO_x from flue gases. *AIChE J.* **2014,** *60* (6), 2314-2323.

(48) Park, J.; Howe, J. D.; Sholl, D. S., How Reproducible Are Isotherm Measurements in Metal-Organic Frameworks? *Chem. Mater.* **2017,** *29* (24), 10487-10495.

(49) Kastner, J., Umbrella sampling. *WIREs Comput. Mol. Sci.* **2011,** *1* (6), 932-942.

(50) Plimpton, S., Fast Parallel Algorithms for Short-Range Molecular-Dynamics. *J. Comput. Phys.* **1995,** *117* (1), 1-19.

(51) Fiorin, G.; Klein, M. L.; Henin, J., Using collective variables to drive molecular dynamics simulations. *Mol. Phys.* **2013,** *111* (22-23), 3345-3362.

(52) Grossfield, A., WHAM: the weighted histogram analysis method, version 2.0.9, http://membrane.urmc.rochester.edu/content/wham.

(53) Haldoupis, E.; Watanabe, T.; Nair, S.; Sholl, D. S., Quantifying Large Effects of Framework Flexibility on Diffusion in MOFs: CH_4 and CO_2 in ZIF-8. *ChemPhysChem* **2012,** *13* (15), 3449-3452.

(54) Amirjalayer, S.; Tafipolsky, M.; Schmid, R., Molecular dynamics simulation of benzene diffusion in MOF-5: Importance of lattice dynamics. *Angew. Chem. Int. Ed.* **2007,** *46* (3), 463-466.

(55) Fairen-Jimenez, D.; Moggach, S. A.; Wharmby, M. T.; Wright, P. A.; Parsons, S.; Duren, T., Opening the Gate: Framework Flexibility in ZIF-8 Explored by Experiments and Simulations. *J. Am. Chem. Soc.* **2011,** *133* (23), 8900-8902.

(56) Greathouse, J. A.; Allendorf, M. D., The interaction of water with MOF-5 simulated by molecular dynamics. *J. Am. Chem. Soc.* **2006,** *128* (33), 10678-10679.

(57) Skoulidas, A. I.; Sholl, D. S., Self-diffusion and transport diffusion of light gases in metal-organic framework materials assessed using molecular dynamics simulations. *J. Phys. Chem. B* **2005,** *109* (33), 15760-15768.

(58) Eum, K.; Jayachandrababu, K. C.; Rashidi, F.; Zhang, K.; Leisen, J.; Graham, S.; Lively, R. P.; Chance, R. R.; Sholl, D. S.; Jones, C. W.; Nair, S., Highly Tunable Molecular Sieving and Adsorption Properties of Mixed-Linker Zeolitic Imidazolate Frameworks. *J. Am. Chem. Soc.* **2015,** *137* (12), 4191-4197.

(59) Ismail, A. F.; Khulbe, K.; Matsuura, T., *Gas Separation Membranes: Polymeric and Inorganic*; Springer: Cham, Switzerland, 2015.

(60) Zhang, K.; Lively, R. P.; Zhang, C.; Chance, R. R.; Koros, W. J.; Sholl, D. S.; Nair, S., Exploring the Framework Hydrophobicity and Flexibility of ZIF-8: From Biofuel Recovery to Hydrocarbon Separations. *J. Phys. Chem. Lett.* **2013,** *4* (21), 3618-3622.

(61) Matteucci, S.; Yampolskii, Y.; Freeman, B. D.; Pinnau, I., *"Transport of gases and vapors in glassy and rubbery polymers" in, Yampolskii, Yuri; Freeman, Benny D.; Pinnau, Ingo, Materials Science of Membranes for Gas and Vapor Separation, pp. 1-47*. John Wiley & Sons: 2006.

(62) Breck, D. W., *Zeolite Molecular Sieves: Structure, Chemistry, and Use*. New York: Wiley: 1974.

(63) Xie, L. J.; Liu, F. D.; Liu, K.; Shi, X. Y.; He, H., Inhibitory effect of NO2 on the selective catalytic reduction of NO_x with NH_3 over one-pot-synthesized Cu-SSZ-13 catalyst. *Catal. Sci. Technol.* **2014,** *4* (4), 1104-1110.

(64) Haldoupis, E.; Nair, S.; Sholl, D. S., Efficient Calculation of Diffusion Limitations in Metal Organic Framework Materials: A Tool for Identifying Materials for Kinetic Separations. *J. Am. Chem. Soc.* **2010,** *132* (21), 7528-7539.

(65) Mace, A.; Laasonen, K.; Laaksonen, A., Free energy barriers for CO_2 and N_2 in zeolite NaKA: an ab initio molecular dynamics approach. *Phys. Chem. Chem. Phys.* **2014,** *16* (1), 166-172.

(66) Hao, S. Q.; Sholl, D. S., Rapid prediction of hydrogen permeation through amorphous metal membranes: an efficient computational screening approach. *Energy Environ. Sci.* **2013,** *6* (1), 232-240.

CHAPTER 6

OUTLOOK

6.1 Thesis Summary

In my thesis work, I utilized computational methods to investigate potential point defects in metal-organic frameworks (MOFs) as well as the degradation reactions that result in these defects.[1-4] Based on the proposed defects, I also explored the impact of these defects on molecular diffusion in zeolitic-imidazolate frameworks (ZIFs) by using molecular dynamics simulations.[5]

Drawing on analogies with conventional silicon-based zeolites, in Chapter 3, we utilized density functional theory (DFT) calculations to examine the structure and stability of putative point-defect structures including vacancies and "dangling" linkers within the prototypical ZIF-8 bulk structure.[1] Considering both post-synthetic (gas-phase) and synthetic (solution-phase) conditions, we found that several of the defect structures lie low in energy relative to the defect-free parent crystal, with barriers to defect formation that are large but surmountable under relevant temperatures. These results were consistent with experimental observations of ZIF stability and reactivity[6-7] and suggested that defects may play an important role in influencing the long-term stability of MOFs under conditions that include exposure to water vapor and trace contaminants such as acid gases. Of the point defects in bulk ZIF-8, the dangling-linker models were applied to ZIF-8 external surfaces and MIL-125 bulk structures to predict the degradation reactions in these materials. Coupled with experimental observations, our predictions were shown to be plausible.[2-3]

To further understand the degradation mechanisms of ZIFs, in Chapter 4, we conducted a comprehensive study utilizing DFT calculations to investigate the chemical stability of bulk ZIFs and their external surfaces under conditions of acid-gas exposure. We also examined the influence of steric factors such as topology and ligand functionalization on the relative chemical stability of prototypical ZIFs, ZIF-2 and ZIF-8, including their hypothetical polymorphs. We found that defect formation is more thermodynamically and kinetically favorable at ZIF external surfaces versus the bulk, and that both topology and ligand functionalization impact defect formation. In addition, we provided a detailed mechanism for the reaction of ZIF crystal with sulfurous and sulfuric acids, of which the latter serves as a catalyst in potential degradation reactions of ZIFs. Finally, in this chapter, we provided information about the adsorption strength of a range of acid gases to defective ZIF structures, which can inform potential strategies to regenerate ZIFs and/or achieve defect engineering in these materials.

Because defects are ubiquitous in materials, they may play an important role in affecting the performance of materials in practical applications. In Chapter 5, we investigated the influence of point defects on the diffusion of molecules including water, hydrocarbons, and acid gases in ZIF-8 using molecular simulations. To make these simulations possible, we introduced a force field that extends previous descriptions of pristine ZIF-8 to include experimentally relevant point defects. In general, the point defects we examined increase the local hopping rate for molecular diffusion, suggesting that low concentrations of these defects will not dominate long range molecular diffusion in ZIF-8.

My thesis work aims to facilitate the understanding of MOF materials in an atomistic level and suggest potential impacts of the degradation on MOF applications.

Extending from this thesis, several topics deserve future consideration. In the following section, I will focus on two topics that closely related to this thesis work.

6.2 Potential Directions for Future Work

6.2.1 The Role of ZIF Topology and Flexibility on Molecular Diffusion

In Chapter 5 we have investigated the impact of defective structures on the molecular diffusion in ZIF-8. There are many other factors of interest influencing the molecular diffusion in ZIFs, for example, topology and flexibility. As we know from Chapter 5, defective structures in ZIF-8 mainly alter pore sizes and the flexibility of local structures, or more specifically, the 6-member-ring (6MR) windows. As a result, the local hopping rates for all the adsorbate molecules investigated are significantly changed by the presence of defects.

ZIF polymorphs are ideal models to study topology's influence as the only difference between a set of ZIF polymorphs is their topologies. ZIFs adopt structures of zeolites, so it is possible to construct a series of hypothetical ZIF polymorphs by using different zeolite net topologies. Table 6.1 lists the codes of all the 6MR zeolite structures in the database of zeolite structures,[8] which can serve as a guidance for the construction of 6MR ZIF polymorphs. ZIF-8 polymorphs with 2-methylimidazolate (mIM) linkers are good candidates for studying 6MR ZIFs because there are established flexible force field parameters for ZIF-8 that can be applied to other $Zn(mIM)_2$ crystals that have identical local structures of ZIF-8. We can use TST methods coupled with MD simulations to derive local hopping rates of various adsorbate molecules in these hypothetical structures.

Calculations of this kind can give insight into the factors that control molecular diffusivities in MOFs.

Table 6.1 6MR zeolite structures from the database of zeolite structures.[8]

AFG	AST	DOH	FAR	FRA	GIU	LIO
LOS	MAR	MEP	MSO	MTN	NON	RUT
SGT	SOD	SVV	TOL	UOZ		

Preliminary results for several ZIF-8 polymorphs are shown in Table 6.2, which lists the window size distributions of 6MR windows (for empty pores) as well as energy barriers, transmission coefficients, and hopping rates of methane through corresponding windows at room temperature by using the flexible force fields of ZIF-8 we used in Chapter 5.[9] The reaction pathways of methane and the position of 6MR windows are shown in Figure 6.1. We can see that the window sizes and their deviations alone are not well correlated to the hopping rates of methane (Figure 6.2), so that additional features of the polymorph structures need to be explored to quantify the topology. A feasible direction towards this goal is to make analogies to zeolites, for example, measuring the window's harmonicity of vibrations or number of distinct window directions.[10-11]

Table 6.2 Calculated window diameters with standard deviations, energy barriers, transmission coefficients, and hopping rates of methane at 35°C in $Zn(mIM)_2$ polymorphs DOH, SGT, and LOS.

ZIF window	Diameter (Å)	Standard Deviation (Å)	Energy (kJ/mol)	Transmission Coefficient	Hopping rate (s^{-1})
DOH window 1	3.28 ± 0.01	0.24	13.61	0.2517	1.26×10^8
DOH window 2	3.17 ± 0.01	0.23	16.44	0.2936	6.14×10^7
SGT window 1	3.05 ± 0.01	0.30	16.41	0.4462	1.28×10^8
SGT window 2	3.41 ± 0.01	0.38	12.15	0.3011	4.07×10^8
LOS window 1	3.21 ± 0.01	0.25	13.05	0.1541	1.22×10^8
LOS window 2	3.11 ± 0.01	0.28	10.00	0.7007	1.91×10^9

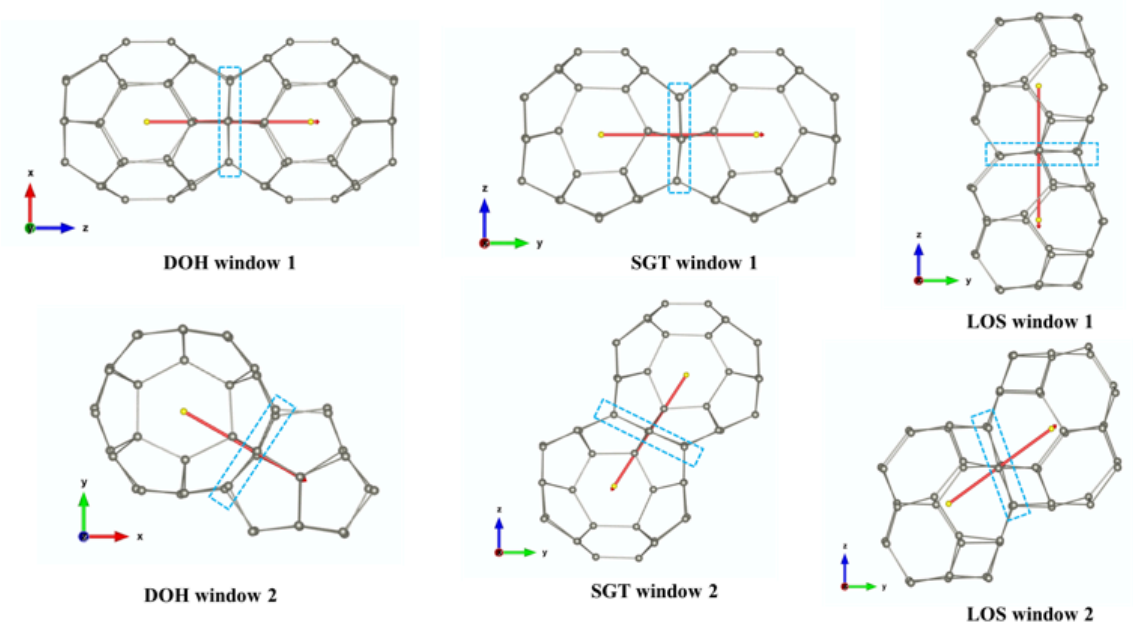

Figure 6.1 Local structures of ZIF polymorphs listed in Table 6.2, where only Zn atoms are shown for clarity. The red arrows label the reaction pathways of a methane hopping through a 6MR window, which is in the blue dotted rectangular, with the starting and ending points marked by yellow bullets.

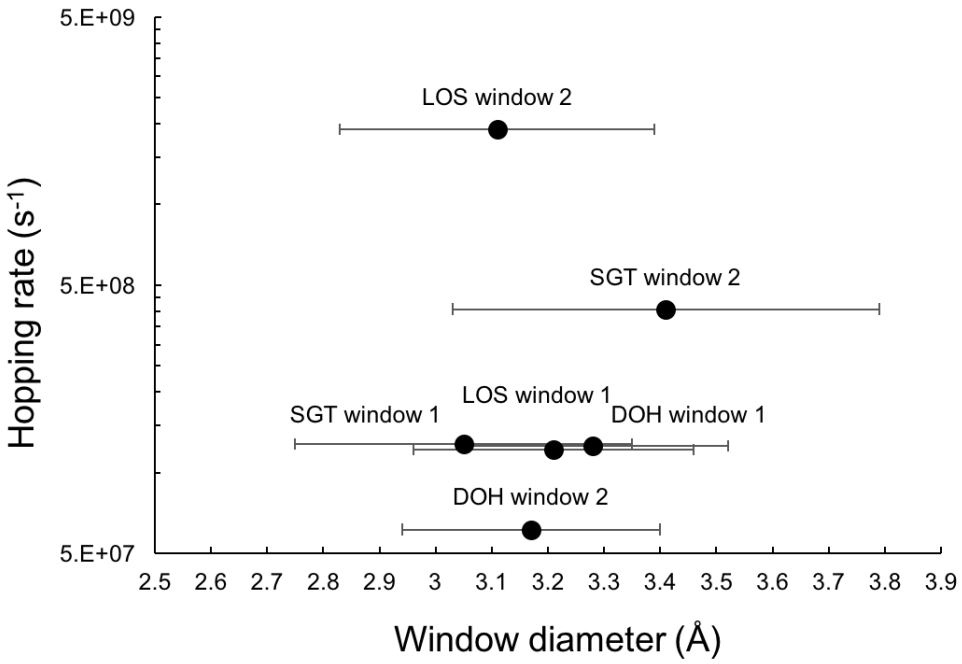

Figure 6.2 Hopping rate of methane in ZIF polymorphs listed in Table 6.2 as a function of the window diameter. The horizontal segment represents the standard deviation of the window diameter for each data point.

The investigation of topology requires development of polymorph structures, while the study of structural flexibility is in another potentially useful direction. In MD simulations, we can artificially tune the flexibility of a ZIF structure by changing its force field parameters such as bonds, angles, and dihedrals. Therefore, a feasible approach to tackle this question using a range of force fields is straightforward, and this method is not limited to ZIFs and may be transferable to other MOF systems.

6.2.2 Propagation of Point Defects During Degradation of MOFs

In my thesis work, I focused on possible point defects induced in pristine MOF structures, which I assumed was the "first step" of degradation process. However, degradation does not stop at this step, for instance, the retained pore volume and percentage

of cleaved Zn-N bonds were found to decrease and increase, respectively, over several days exposure to humid acidic environments.[7] To have a "big picture" of the entire degradation process and more comparable modeling to what has been observed by experiments, it is necessary to figure out the following steps of degradation processes, *i.e.*, the propagation of defects. The propagation of defects has been explored in various materials. The surface observations of HKUST-1 by the confocal fluorescence microscopy indicated that defective fractures propagate in the crystal interior either along {111} or {100} crystalline planes.[12] An important factor that facilitate defect propagation is possibly the coupling of various of defects, for example, in two-dimensional material WS_2 a strong coupling between Mo dopants and S vacancies as well as grain boundaries was found by scanning transmission electron microscopy (STEM). Most of the S vacancies identified by STEM colocalize with Mo dopants.[13] Recently our research group has found that the formation of a second linker vacancy in ZIFs is relatively more energetic favorable when it is adjacent to the initial vacancy, which indicates that defects propagate in the way of clustering in ZIF materials. The results in this thesis work about degradation reactions provide a strong basis from which propagation and growth of defects in ZIFs can be studied in a quantitative way.

6.3 References

(1) Zhang, C. Y.; Han, C.; Sholl, D. S.; Schmidt, J. R., Computational Characterization of Defects in Metal-Organic Frameworks: Spontaneous and Water-Induced Point Defects in ZIF-8. *J. Phys. Chem. Lett.* **2016,** *7* (3), 459-464.

(2) Pang, S. H.; Han, C.; Sholl, D. S.; Jones, C. W.; Lively, R. P., Facet-Specific Stability of ZIF-8 in the Presence of Acid Gases Dissolved in Aqueous Solutions. *Chem. Mater.* **2016,** *28* (19), 6960-6967.

(3) Mounfield, W. P.; Han, C.; Pang, S. H.; Tumuluri, U.; Jiao, Y.; Bhattacharyya, S.; Dutzer, M. R.; Nair, S.; Wu, Z.; Lively, R. P.; Sholl, D. S.; Walton, K. S., Synergistic Effects of Water and SO_2 on Degradation of MIL-125 in the Presence of Acid Gases. *J. Phys. Chem. C* **2016,** *120* (48), 27230-27240.

(4) Han, C.; Zhang, C. Y.; Tyminska, N.; Schmidt, J. R.; Sholl, D. S., Insights into the Stability of Zeolitic Imidazolate Frameworks in Humid Acidic Environments from First-Principles Calculations. *J. Phys. Chem. C* **2018,** *122* (8), 4339-4348.

(5) Han, C.; Verploegh, R. J.; Sholl, D. S., Assessing the impact of point defects on molecular diffusion in ZIF-8 using molecular simulations. *J. Phys. Chem. Lett.* **2018,** *9*, 4037–4044.

(6) Bhattacharyya, S.; Pang, S. H.; Dutzer, M. R.; Lively, R. P.; Walton, K. S.; Sholl, D. S.; Nair, S., Interactions of SO_2-Containing Acid Gases with ZIF-8: Structural Changes and Mechanistic Investigations. *J. Phys. Chem. C* **2016,** *120* (48), 27221-27229.

(7) Bhattacharyya, S.; Han, R.; Kim, W. G.; Chiang, Y. D.; Jayachandrababu, K. C.; Hungerford, J. T.; Dutzer, M. R.; Ma, C.; Walton, K. S.; Sholl, D. S.; Nair, S., Acid Gas Stability of Zeolitic Imidazolate Frameworks: Generalized Kinetic and Thermodynamic Characteristics. *Chem. Mater.* **2018,** *30* (12), 4089-4101.

(8) Baerlocher, Ch.; McCusker, L. B. Database of Zeolite Structures: http://www.iza-structure.org/databases/.

(9) Zhang, L. L.; Hu, Z. Q.; Jiang, J. W., Sorption-Induced Structural Transition of Zeolitic Imidazolate Framework-8: A Hybrid Molecular Simulation Study. *J. Am. Chem. Soc.* **2013,** *135* (9), 3722-3728.

(10) Awati, R. V.; Ravikovitch, P. I.; Sholl, D. S., Efficient and Accurate Methods for Characterizing Effects of Framework Flexibility on Molecular Diffusion in Zeolites: CH_4 Diffusion in Eight Member Ring Zeolites. *J. Phys. Chem. C* **2013,** *117* (26), 13462-13473.

(11) Awati, R. V.; Ravikovitch, P. I.; Sholl, D. S., Efficient Calculation of Gas Diffusivity in Single-Component and Binary Mixtures of Spherical Adsorbates in Flexible 8MR Zeolites. *J. Phys. Chem. C* **2015,** *119* (29), 16596-16605.

(12) Ameloot, R.; Vermoortele, F.; Hofkens, J.; De Schryver, F. C.; De Vos, D. E.; Roeffaers, M. B. J., Three-Dimensional Visualization of Defects Formed during the Synthesis of Metal-Organic Frameworks: A Fluorescence Microscopy Study. *Angew. Chem., Int. Ed.* **2013,** *52* (1), 401-405.

(13) Azizi, A.; Wang, Y. X.; Stone, G.; Elias, A. L.; Lin, Z.; Terrones, M.; Crespi, V. H.; Alem, N., Defect Coupling and Sub-Angstrom Structural Distortions in $W_{1-x}Mo_xS_2$ Monolayers. *Nano Lett* **2017,** *17* (5), 2802-2808.

APPENDIX A: SUPPORTING INFORMATION FOR CHAPTER 3

A.1 Additional Information for Section 3.4

Finite cluster models of bulk ZIF-8 were constructed by carving out the appropriate fragment from the periodic system, with dangling imidazolate nitrogen lone pairs terminated with Li ions to mimic dative ligand bonding to the missing Zn(II) cation. The optimal Li-N bond distance was previously calculated to best reproduce the charge density of the periodic ZIF.[1] We utilized a $Zn_2Im_7Li_6^{3+}$ cluster (see Figure A.1) as the basis for linker-vacancy and dangling linker defect models, introducing the linker defect between the two Zn atoms to minimize edge effects. In the case of metal defects, we utilized a smaller $ZnIm_4Li_4^{2+}$ cluster (see Figure A.1), removing the central Zn and protonating the dangling imidazolate linkers as described in the main text (see Figure 3.2 iv/v, Li ions omitted).

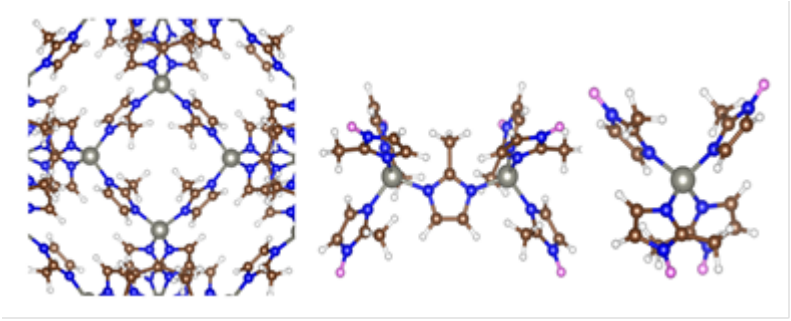

Figure A.1 Periodic (left) and cluster (middle and right) models of ZIF-8. Cluster models are utilized only to estimate solvation effects on the gas-phase reaction energies (calculated via plane-wave DFT). The larger cluster (middle) is used for modeling dangling linker and linker vacancy formation reactions, while the smaller cluster (right) one is used to model metal vacancies. The cluster models were constructed by carving out a proper fragment from the periodic system. The dangling nitrogen lone pairs were capped with Li ions to mimic dative ligand bonding.

During all cluster optimizations and energy calculations, only a subset of "active" atoms are allowed to relax. In the case of the larger cluster models (containing two Zn atoms), only the Zn ions, nearest six nitrogen atoms and linker between two Zn ions are allowed to relax. For the smaller models (containing one Zn atom), only the Zn ions and nearest four nitrogen atoms are allowed to relax. All of the other atoms outside of active subsystem are kept fixed to represent the surrounding rigid crystal framework. These constrained optimization were performed using LBFGS[2] algorithm as implemented in ASE (Atomic Simulation Environment,[3] invoking GAUSSIAN09[4] to calculate forces with Def2-SVP[5-6] basis set). Optimization and subsequent single point calculations employed PBE[7] and B3LYP,[8-9] respectively, for consistency with the periodic calculations. Single point energy calculations utilized the Def2-TZVPD[5-6] basis set for Zn atoms and Def2-TZVP[5-6] for all other atoms. The cluster models were validated via comparison of calculated defect formation reaction energetics against calculations utilizing the full periodic system (see Table A.1).

A strain/deformation energy correction has been included for the dangling linker formation reaction (i)-(iii). The strain energy is defined as the energy difference between the optimized, defective, ZIF (after removing any adsorbates, e.g. water and/or other proton donating agents) and the optimized, defect-free ZIF. This strain energy is calculated for both the periodic and cluster models, with the strain energy correction defined as the difference between the periodic and cluster strain energies. This correction accounts for the non-local strain on the surrounding crystal lattice induced by the defect, which is necessarily absent in the finite cluster model.

Table A.1 Comparison of calculated formation energies for the possible point defects in ZIF-8. ΔE^{gas}, ΔZPE (periodic PBE level), and $\Delta\Delta E^{solv}$ correspond to the gas-phase energy difference, zero-point energy correction, and solvation correction, respectively. Here, 'cr' refers to solid crystal structure; 'p' or 'c' denotes periodic or cluster models, respectively.

(kcal/mol)		Linker vacancy			Zn vacancy		Dangling linker		
	NO.	**i**	**ii**	**iii**	**iv**	**v**	**vi**	**vii**	**viii**
	Defects	**Zn-OH_2…HO-Zn**	**Zn-OH_2…NO_3-Zn**	**Zn-OH_2…COOH-Zn**	**V_{Zn}[Zn$(OH)_2$]**	**V_{Zn}[Zn$(NO_3)_2$]**	**Zn-OH…HmIm-Zn**	**Zn-NO_3…HmIm-Zn**	**Zn-COOH…HmIm-Zn**
ΔE^{gas}	PBE(p)	2.1	-4.7	-4.7	42.1(-5.9,cr)	20.6(-26.3,cr)	12.1	3.0	7.0
	B3LYP(p)	0.0	-9.1	-7.1	45.5(-2.3,cr)	21.2(-25.4,cr)	15.4	3.8	9.9
	PBE(c)	1.5	-3.6	-3.9	45.4	23.9	9.1	4.9	9.6
	B3LYP(c)	1.2	-7.0	-5.6	47.7	21.7	10.3	3.4	8.8
	PBE-D3	13.6(-4.5)	1.6(-8.4)	-2.2(-9.7)	45.2(-8.9,cr)	22.8(-44.1,cr)	9.1	3.2	0.3
	B3LYP-D3	17.7(-0.9)	0.8(-9.4)	3.6(-8.4)	52.4(-10.2,cr)	26.8(-52.5,cr)	10.7	0.2	-0.8
ΔZPE	PBE	0.9	2.2	1.7	0.8(3.0,cr)	-1.0(5.9,cr)	2.8	3.0	2.6
$\Delta\Delta E^{solv}$	PBE	-3.9	-2.8	-3.3	(26.9,cr)	(13.2,cr)	8.8	6.8	0.5
	B3LYP	-3.8	-1.0	-2.0	(29.0,cr)	(15.3,cr)	8.9	4.6	-0.8

Table A.2 ΔE^{gas} of reactions (i) and (vi) in Table A.1 at the B3LYP level with geometries relaxed at the PBE (PBE/B3LYP) or B3LYP (B3LYP/B3LYP) levels. The differences due to the relaxation at the B3LYP level are < 1 kcal/mol.

Opt/SP	ΔE(i)	ΔE(vi)
PBE/B3LYP	0.0	15.4
B3LYP/B3LYP	0.0	15.2

Table A.3 Lattice constants of ZIF-8, estimated by PBE and PBE-D3, as compared with the experimentally measured lattice constant.

Method	a(ZIF-8)
PBE	17.179
PBE-D3	16.996
Experiment	16.991

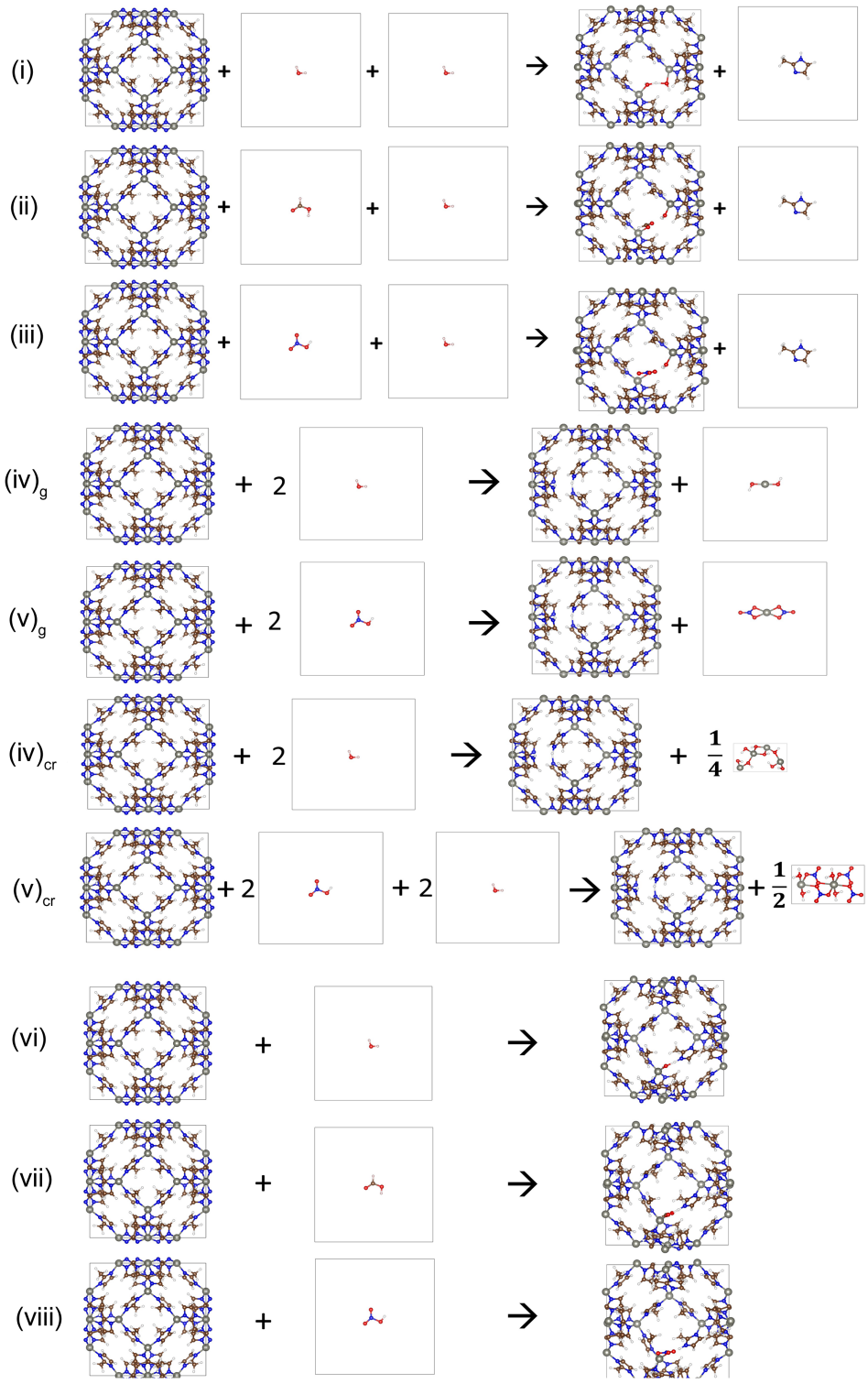

Figure A.2 Schematic diagram of various reactions of point-defect formation reactions: (i)-(iii) linker vacancy, (iv)-(v) zinc vacancy, (vi)-(viii) dangling linker. Here, the square box represents the unit cell, 'g' denotes product structure of $Zn(OH)_2$ or $Zn(NO_3)_2$ in gas phase; 'cr' means product structure of $Zn(OH)_2$ or $Zn(NO_3)_2{\cdot}2H_2O$ in crystal solid state.

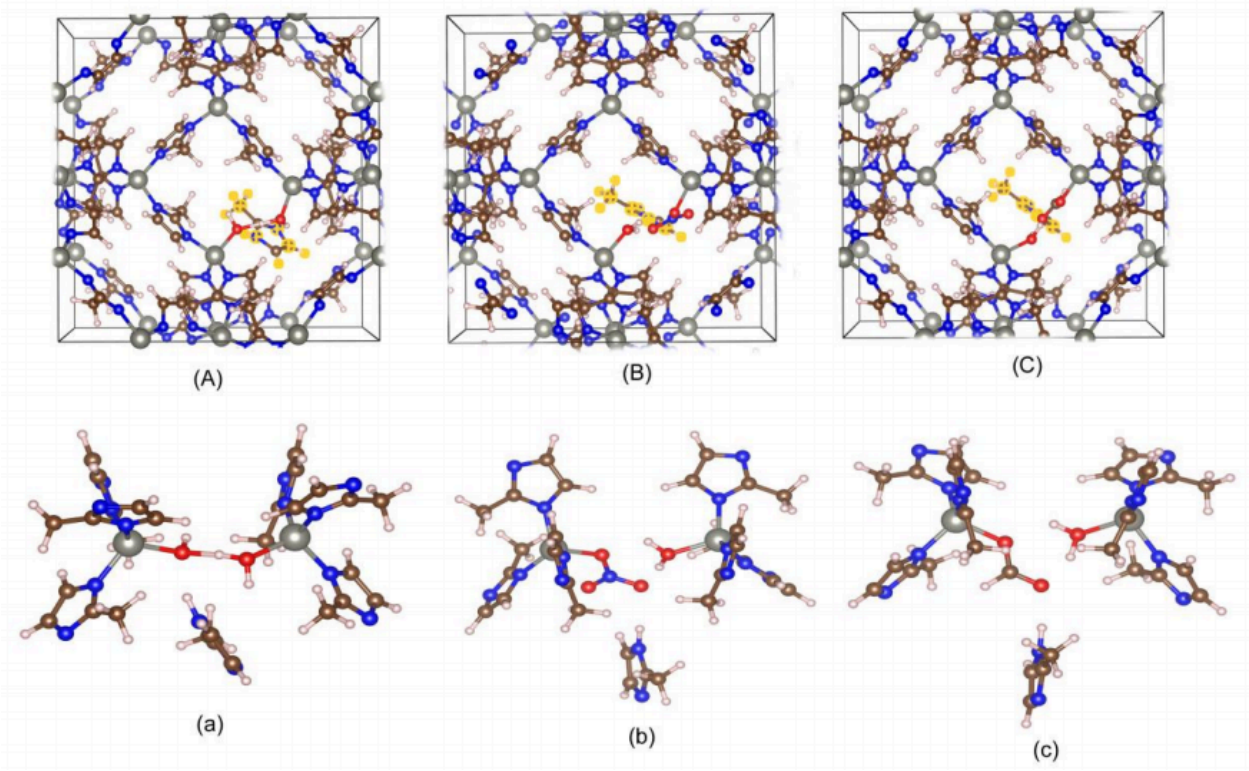

Figure A.3 Illustration of interacting product complexes for linker vacancy formation reactions. Periodic unit cell structures in panels (A) – (C) correspond to the defects (i) – (iii) in Table 3.1, respectively. The removed imidazole molecule (highlighted in yellow) remains adsorbed within the ZIF pore. The corresponding local structure are shown in panels (a) – (c).

Solvation effects have been incorporated using a combination of experimental solvation enthalpies (where available) and computational Polarizable Continuum Model (PCM)[10] estimates. As shown in Figure A.4, aqueous solvation energies are estimated using standard experimental data for simple molecules (H_2O, HNO_3, HCOOH，$Zn(NO_3)_2$，$Zn(OH)_2$), while the PCM[10] approach has been used to calculate aqueous solvation energies of perfect and defective ZIF-8 (using the cluster models described above) and neutral imidazole. Note that while the absolute solvation energies of the cluster models are

physically irrelevant (since they are finite clusters), the relevant solvation corrections only appear as *differences* of the defective and defect-free cluster models. We utilize the SMD solvation model of Truhlar and coworkers,[11] and cluster structures are further optimized in presence of the continuum solvent to account for deformation effects due to solvent.

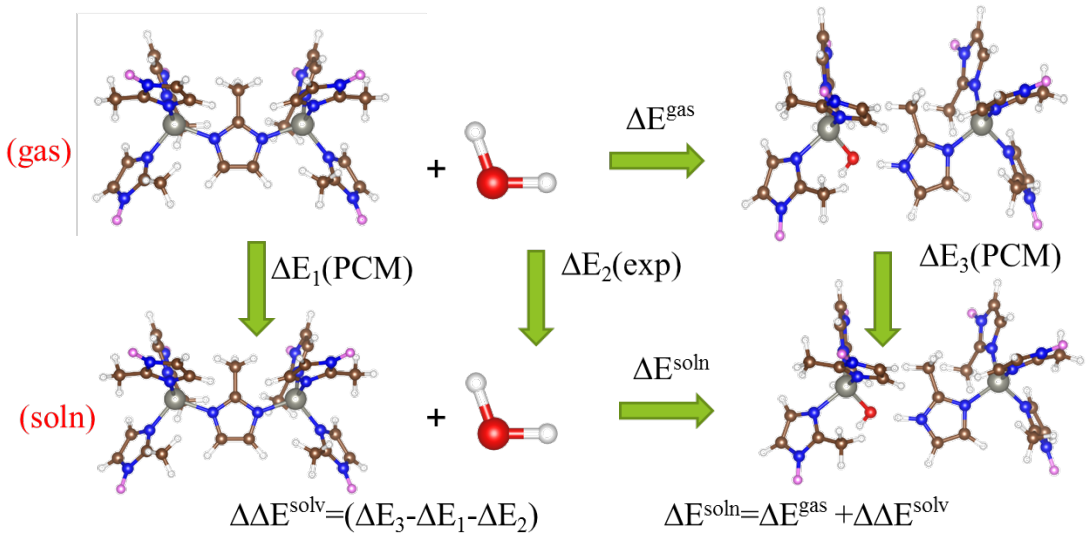

Figure A.4 Computational scheme for evaluating solvation effects on the gas-phase defect formation reactions. Aqueous solvation energies of perfect (ΔE_1) and defective (ΔE_3) ZIF-8 were estimated using a polarizable continuum (PCM) approach in conjunction with finite cluster models, ΔE_2 is evaluated using experimental solvation enthalpies, corrected to energies (where appropriate) assuming ideal gas behavior. ΔE^{gas}, $\Delta\Delta E^{solv}$, ΔE^{soln} refer to the gas phase reaction energy, solvation correction and solution-phase reaction energy, respectively.

Table A.4 Solvation energies of the various relevant species. For solvation energy calculations (i-viii), solvation energies of perfect and defective ZIF-8 are estimated using cluster models and a PCM approach at either a B3LYP or PBE level of theory, with PBE results given in parentheses. Cluster model structures for (i-viii) are shown in Figure A.1 (Li atoms are omitted). Other species (a-e) are estimated using experimental data (ΔH^{soln}(298.15K)), where ΔE is estimated assuming ideal gas behavior (ΔH- Δn*RT). 'cr': crystal state, 'ai': aqueous ionic state, 'aq': aqueous phase, 'g': gas phase.

		Reactions	ΔE^{soln} **kcal·mol^{-1}**	ΔH^{soln} **kcal·mol^{-1}**
PCM	(i)	Zn-OH_2…HO-Zn(cr) → Zn-OH_2…HO-Zn(aq)	-274.4(-273.3)	--
	(ii)	Zn-OH_2…NO_3-Zn(cr) → Zn-OH_2…NO_3-Zn(aq)	-279.1(-275.9)	--
	(iii)	Zn-OH_2…COOH-Zn(cr) → Zn-OH_2…COOH-Zn(aq)	-273.7(-273.2)	--
	(iv)/(v)	$V_{Zn}(mIm)_4Li_4$(cr) → $V_{Zn}(mIm)_4Li_4$(aq)	-145.3(-144.8)	--
	(vi)	Zn-OH…HmIm-Zn(cr)→ Zn-OH…HmIm-Zn(aq)	-262.3(-261.1)	--
	(vii)	Zn-NO_3…HmIm-Zn(cr)→Zn-NO_3…HmIm-Zn(aq)	-273.4(-269.9)	--
	(viii)	Zn-COOH…HmIm-Zn(cr)→Zn-COOH…HmIm-Zn(aq)	-272.5(-269.9)	--
		$Zn(mIm)_4Li_4$(cr) → $Zn(mIm)_4Li_4$(aq)	-147.5 (-144.9)	--
		$Zn_2(mIm)_7Li_4$(cr) → $Zn_2(mIm)_7Li_4$(aq)	-261.3(-260)	--
		HmIm(g) →HmIm(aq)	-10.5(-10.4)	--
Exp[12]	(a)	HNO_3 (g) →HNO_3 (ai)	-16.7	-17.3
	(b)	H_2O (g) → H_2O (l)	-9.9	-10.5
	(c)	HCOOH (g) → HCOOH (ai)	-10.6	-11.2
	(d)	$Zn(OH)_2$ (cr) → $Zn(OH)_2$ (ai)	7.0	7.0
	(e)	$Zn(NO_3)_2$ (cr) → $Zn(NO_3)_2$ (ai)	-20.3	-20.3

Table A.5 Computational estimates for entropic effects for gas-phase linker vacancy formation, reaction (i). Translational, rotational, and vibrational entropy for all gas-phase species (H_2O, HNO_3, formate, imidazole) were calculated at the PBE level, using "standard" conditions of 298 K and 1 atm. The "upper bound" estimate assumes that the reacting water and proton-donating agent lose all (translational, rotational, and vibrational) entropy upon reaction, while the "best guess" estimate assumes the water and proton-donating agent retain their rotational entropy after reaction. In solution, the entropic effects will be dramatically reduced due to decreased translational/rotational entropy of the gas-phase species.

kcal/mol	-TΔS (Upper bound)	-TΔS (Best guess)
X=OH-	4.7	-1.4
X=NO3-	10.2	-3.1
X=Formate	8.9	-2.7

A.2 Additional Information for Section 3.5

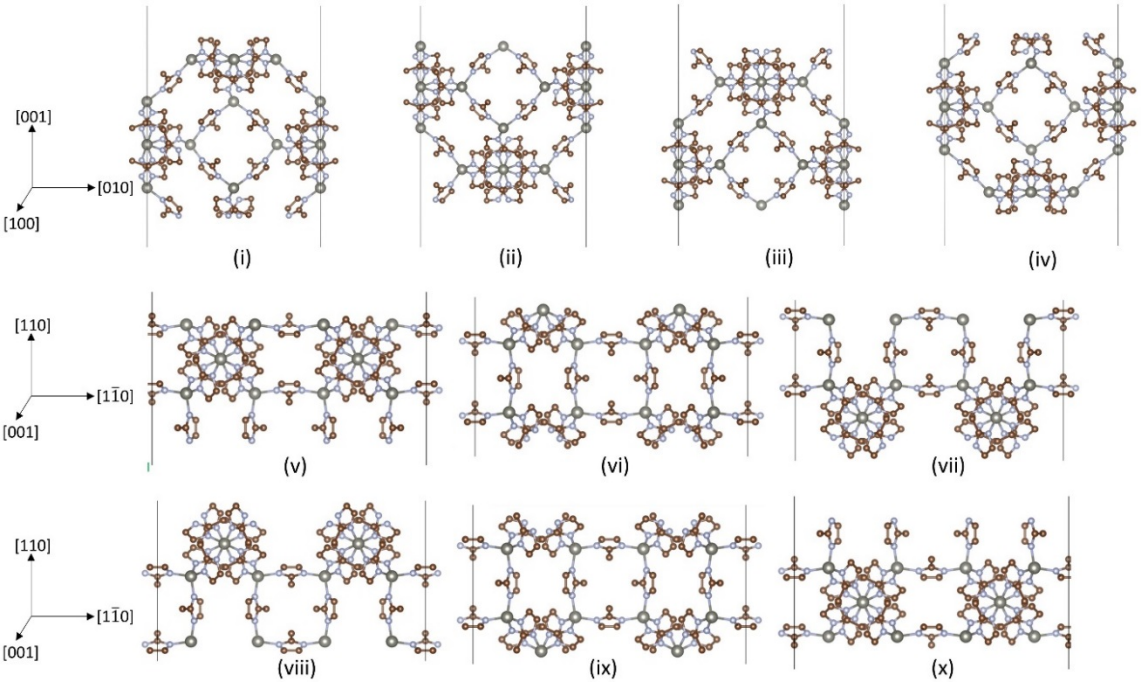

Figure A.5 Side view of proposed (i-iv) {100} surfaces and (v-x) {110} surfaces of ZIF-8. The atoms on the top of each slab are fully relaxed to represent the surface, while the atoms at the bottom are fixed at the bulk ZIF-8 positions. Hydrogen atoms are not shown.

Table A.6 Surface energies of proposed ZIF-8 surfaces in Figure A.5.

Surface	Termination	Surface Energy (J/m^2)
{100}	i	0.72
	ii	0.67
	iii	0.64
	iv	0.72
{110}	v	0.43
	vi	0.93
	vii	0.90
	viii	0.87
	ix	0.90
	x	0.47

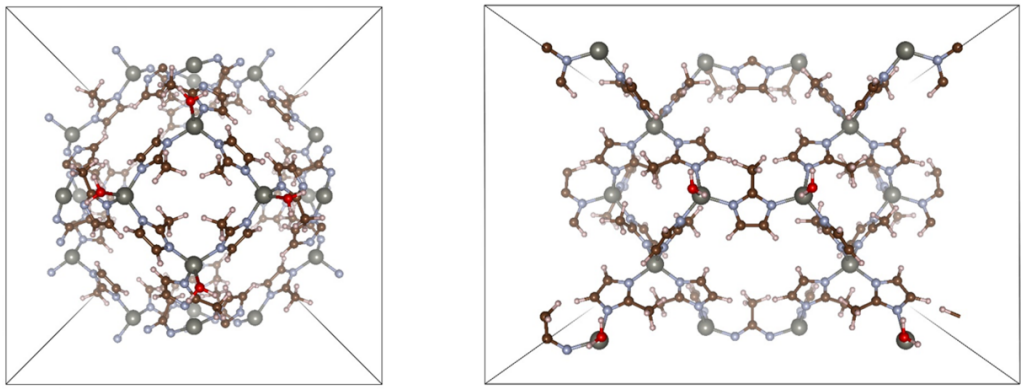

Figure A.6 Top-down view of the {100} and {110} surfaces showing the differences in atomic packing. The {100} surface is more close-packed with the six-member rings at an angle with respect to the surface, whereas the {110} surface contains six-member rings in the plane of the surface. Zn atoms at the external surface would be undercoordinated and so have been terminated with water molecules.

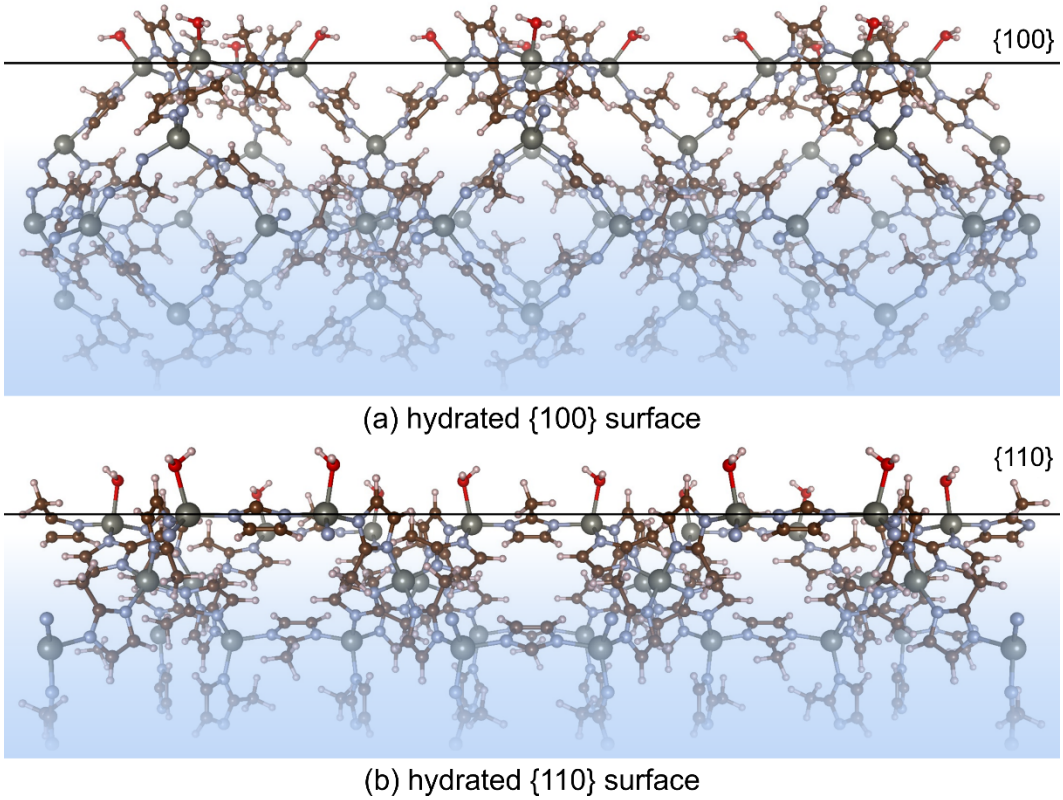

Figure A.7 Side view of the {100} and {110} surfaces (multiple unit cells). Zn atoms at the external surface would be undercoordinated and so have been terminated with water molecules.

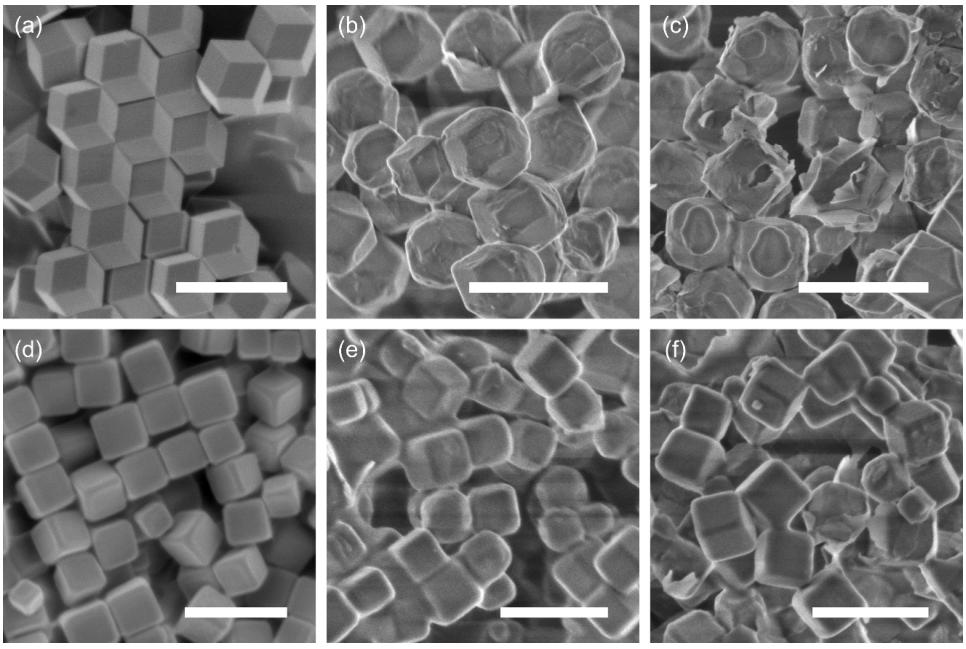

Figure A.8 SEM images of (a-c) ZIF-8 rhombic dodecahedra and (d-f) cubes show increased degradation on the rhombic dodecahedra {110} facets compared to the {100} facets of the cubes. (a, d) as synthesized particles, and particles exposed to 1.8 mmol/L SO_2 at 25 °C for (b, e) 1 day and (c, f) 7 days. Scale bars: (a-c) 1 μm, (d-f) 500 nm.

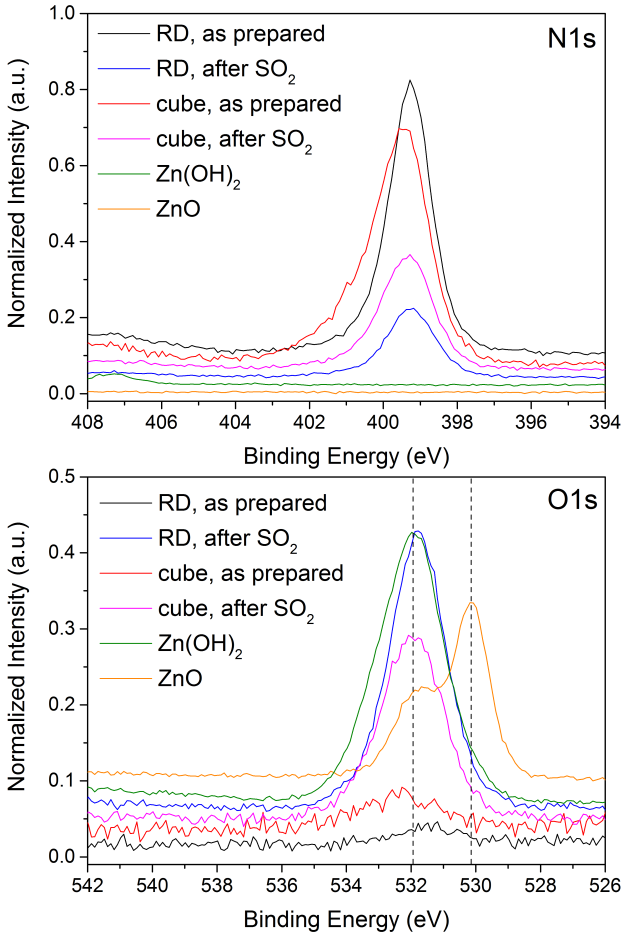

Figure A.9 High-resolution x-ray photoelectron spectra for the N 1s and O 1s binding energy regions for the as-prepared and SO_2-degraded rhombic dodecahedra (RD) and cubes. $Zn(OH)_2$ and ZnO are included as reference spectra, with peak positions indicated by the dashed lines on the O 1s spectra. Spectra have been vertically shifted for clarity.

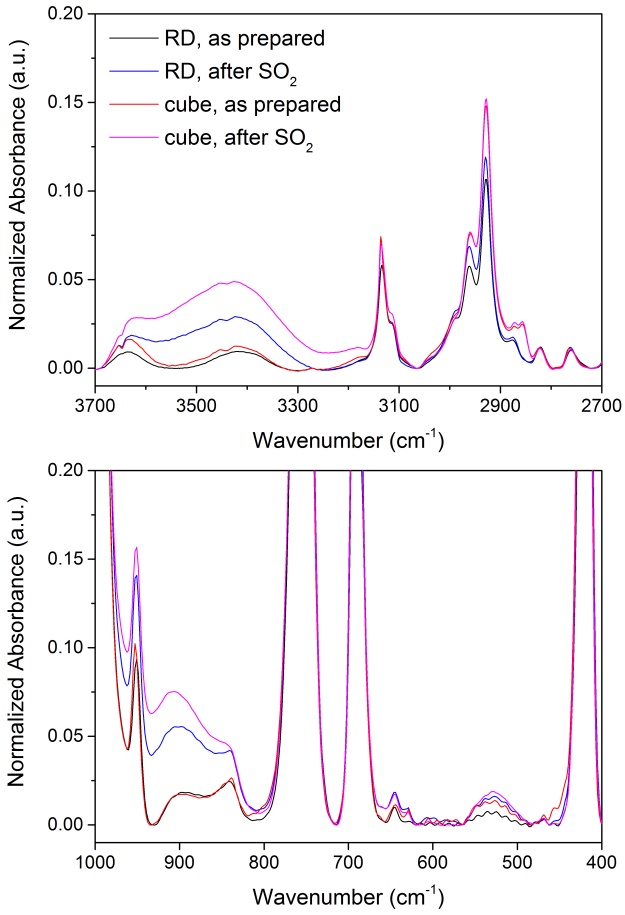

Figure A.10 FTIR spectra for the as-prepared and SO_2-degraded rhombic dodecahedra (RD) and cubes show and increase in the intensity for bands associated with O-H stretching near 3400-3500 cm^{-1} (top) and S-O stretching near 900 cm^{-1} (bottom).

A.3 Additional Information for Section 3.6

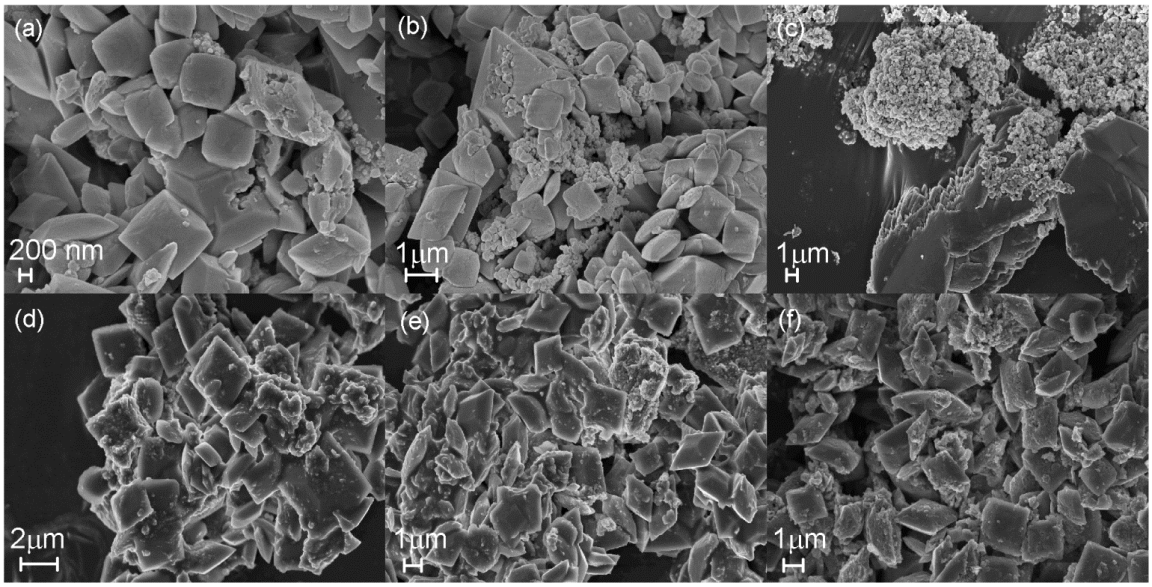

Figure A.11 SEM images of MIL-125 after aqueous SO_2 exposure for (a) 1.67 ppm-h, (b) 10 ppm-h, (c) 20 ppm-h, and after humid SO_2 exposure for (d) 1.25 ppm-h, (e) 15 ppm-h, (f) 2365 ppm-h.

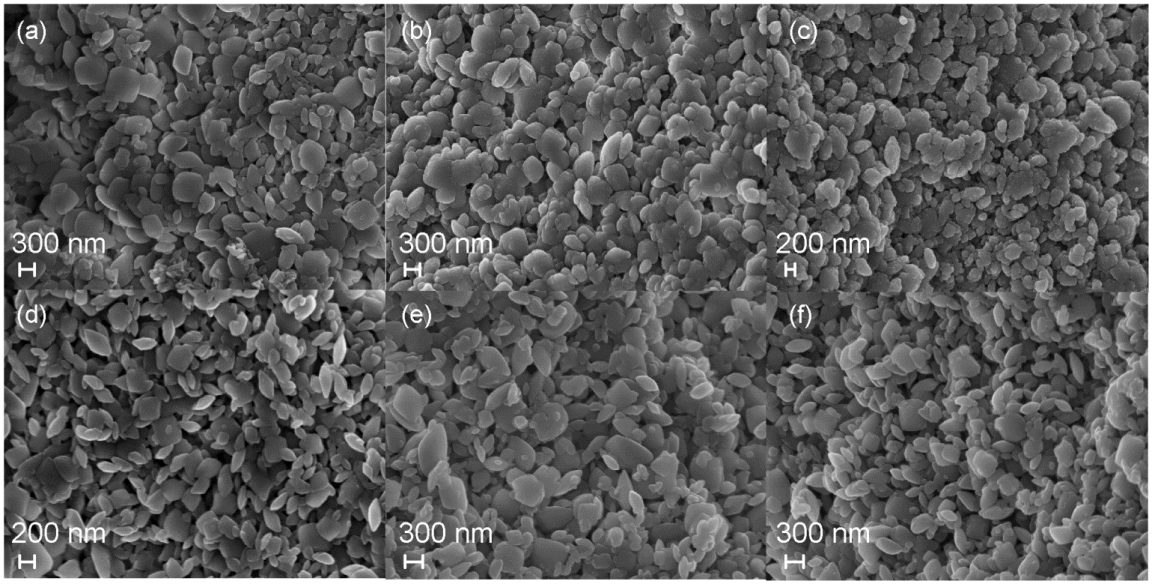

Figure A.12 SEM images of MIL-125-NH_2 after aqueous SO_2 exposure for (a) 20 ppm-h, (b) 240 ppm-h, (c) 1440 ppm-h, and after humid SO_2 exposure for (d) 1.25 ppm-h, (e) 15 ppm-h, (f) 2365 ppm-h.

Table A.7 Calculated vibrational modes of the cluster models shown in **Figure 3.12**

Wavenumber (cm^{-1})	Vibrational mode	cluster
446	Ti-OH stretching	$Ti_8O_8(OH)_4(COOH)_{12}$
656	Ti-O stretching	$Ti_8O_8(OH)_4(COOH)_{12}$
715	S-OH stretching	$Ti_8O_8(OH)_4(COOH)_{11}(HSO_3)$
723	Asy. O-S-OH stretching, Ti-O stretching	$Ti_8O_8(OH)_4(COOH)_{11}(H_2O)(HSO_3)$
742	S-OH stretching, Ti-O stretching	$Ti_8O_8(OH)_4(COOH)_{11}(HSO_3)$
750	Sym. O-S-OH stretching, Ti-O stretching	$Ti_8O_8(OH)_4(COOH)_{11}(H_2O)(HSO_3)$
824	S-O(-Ti) stretching	$Ti_8O_8(OH)_4(COOH)_{11}(H_2O)(HSO_3)$
894	Asy. S-O stretching (weak)	$Ti_8O_8(OH)_4(COOH)_{11}(HSO_3)$
956	Asy. S-O stretching (strong)	$Ti_8O_8(OH)_4(COOH)_{11}(HSO_3)$
975	Sym. S-O stretching	$Ti_8O_8(OH)_4(COOH)_{11}(HSO_3)$
1010	Asy. S-O stretching (very weak)	$Ti_8O_8(OH)_4(COOH)_{11}(HSO_3)$
1054	S=O stretching	$Ti_8O_8(OH)_4(COOH)_{11}(H_2O)(HSO_3)$
1102	S-O-H bending	$Ti_8O_8(OH)_4(COOH)_{11}(HSO_3)$
1139	S-O-H bending	$Ti_8O_8(OH)_4(COOH)_{11}(H_2O)(HSO_3)$
1369	Sym. C-O stretching	$Ti_8O_8(OH)_4(COOH)_{12}$
1565	Water (adsorbed by Ti) bending	$Ti_8O_8(OH)_4(COOH)_{11}(H_2O)(HSO_3)$
1580	Asy. C-O stretching	$Ti_8O_8(OH)_4(COOH)_{12}$
2839	O-H (of water) stretching	$Ti_8O_8(OH)_4(COOH)_{11}(H_2O)(HSO_3)$
3472	O-H (of HSO_3) stretching	$Ti_8O_8(OH)_4(COOH)_{11}(H_2O)(HSO_3)$

A.4 References

(1) McDaniel, J. G.; Yu, K.; Schmidt, J. R., *Ab Initio*, Physically Motivated Force Fields for CO_2 Adsorption in Zeolitic Imidazolate Frameworks. *J. Phys. Chem. C* **2012,** *116* (2), 1892-1903.

(2) Byrd, R. H.; Lu, P. H.; Nocedal, J.; Zhu, C. Y., A Limited Memory Algorithm for Bound Constrained Optimization. *SIAM J. Sci. Comput.* **1995,** *16* (5), 1190-1208.

(3) Bahn, S. R.; Jacobsen, K. W., An object-oriented scripting interface to a legacy electronic structure code. *Comput. Sci. Eng.* **2002,** *4* (3), 56-66.

(4) Frisch, M. J.; Trucks, G. W.; Schlegel, H. B.; Scuseria, G. E.; Robb, M. A.; Cheeseman, J. R.; Scalmani, G.; Barone, V.; Petersson, G. A.; Nakatsuji, H.; Li, X.; Caricato, M.; Marenich, A. V.; Bloino, J.; Janesko, B. G.; Gomperts, R.; Mennucci, B.; Hratchian, H. P.; Ortiz, J. V.; Izmaylov, A. F.; Sonnenberg, J. L.; Williams; Ding, F.; Lipparini, F.; Egidi, F.; Goings, J.; Peng, B.; Petrone, A.; Henderson, T.; Ranasinghe, D.; Zakrzewski, V. G.; Gao, J.; Rega, N.; Zheng, G.; Liang, W.; Hada, M.; Ehara, M.; Toyota, K.; Fukuda, R.; Hasegawa, J.; Ishida, M.; Nakajima, T.; Honda, Y.; Kitao, O.; Nakai, H.; Vreven, T.; Throssell, K.; Montgomery Jr., J. A.; Peralta, J. E.; Ogliaro, F.; Bearpark, M. J.; Heyd, J. J.; Brothers, E. N.; Kudin, K. N.; Staroverov, V. N.; Keith, T. A.; Kobayashi, R.; Normand, J.; Raghavachari, K.; Rendell, A. P.; Burant, J. C.; Iyengar, S. S.; Tomasi, J.; Cossi, M.; Millam, J. M.; Klene, M.; Adamo, C.; Cammi, R.; Ochterski, J. W.; Martin, R. L.; Morokuma, K.; Farkas, O.; Foresman, J. B.; Fox, D. J. *Gaussian 16 Rev. B.01*, Wallingford, CT, 2016.

(5) Weigend, F.; Ahlrichs, R., Balanced basis sets of split valence, triple zeta valence and quadruple zeta valence quality for H to Rn: Design and assessment of accuracy. *Phys. Chem. Chem. Phys.* **2005,** *7* (18), 3297-3305.

(6) Weigend, F., Accurate Coulomb-fitting basis sets for H to Rn. *Phys. Chem. Chem. Phys.* **2006,** *8* (9), 1057-1065.

(7) Perdew, J. P.; Burke, K.; Ernzerhof, M., Generalized gradient approximation made simple [Phys. Rev. Lett. 77, 3865 (1996)]. *Phys. Rev. Lett.* **1997,** *78* (7), 1396-1396.

(8) Becke, A. D., Density-Functional Thermochemistry .3. The Role of Exact Exchange. *J. Chem. Phys.* **1993,** *98* (7), 5648-5652.

(9) Lee, C. T.; Yang, W. T.; Parr, R. G., Development of the Colle-Salvetti Correlation-Energy Formula into a Functional of the Electron-Density. *Phys. Rev. B* **1988,** *37* (2), 785-789.

(10) Cossi, M.; Barone, V.; Cammi, R.; Tomasi, J., *Ab initio* study of solvated molecules: A new implementation of the polarizable continuum model. *Chem. Phys. Lett.* **1996,** *255* (4-6), 327-335.

(11) Marenich, A. V.; Cramer, C. J.; Truhlar, D. G., Universal Solvation Model Based on Solute Electron Density and on a Continuum Model of the Solvent Defined by the Bulk Dielectric Constant and Atomic Surface Tensions. *J. Phys. Chem. B* **2009,** *113* (18), 6378-6396.

(12) Wagman, D. D.; Evans, W. H.; Parker, V. B.; Schumm, R. H.; Halow, I.; Bailey, S. M.; Churney, K. L.; Nuttall, R. L., The NBS Tables of Chemical Thermodynamic Properties - Selected Values for Inorganic and C_1 and C_2 Organic-Substances in SI Units. *J. Phys. Chem. Ref. Data* **1982,** *11*, (Supplement No. 2).

APPENDIX B: SUPPORTING INFORMATION FOR CHAPTER 4

B.1 Additional Computational Details

In order to correctly account for van der Waals interactions, DFT-D3 scheme (see Ref. 50 and 51 of Chapter 4) was applied. In particular for reactions occurring at the ZIFs (001) surfaces the Becke and Johnson (BJ-damping) was used (noted here as PBE-D3(BJ)). This dispersion correction was employed as implemented in VASP while for reactions in the bulk we used PBE-D3(BJ, ABC), which contains three body term (Ref. 51 of Chapter 4). To assure this change does not influence our conclusions on reactivity of outer surfaces and the bulk, calculations for dangling linker formation reaction ($\Delta E_{rxn,DL}$, defined in the Eq. 4.1) at "clean" ZIF-8(001) surface were performed. The calculated $\Delta E_{rxn,DL}$ is -8.10 kcal/mol at the PBE-D3(BJ) level of theory and -8.15 kcal/mol at PBE-D3(BJ, ABC) level of theory, respectively.

The defect formation reactions transition states were found by utilizing the climbing-image nudged elastic band (cNEB) method (Ref. 53, 54 of Chapter 4). Before employing cNEB, NEB calculations were performed for all considered ZIF model systems (except of those for which energy barriers are not provided) to explore the minimum energy reaction pathway for dangling linker (step 1) and ligand vacancy formation (step 2). This was done by creating eight (approximately evenly distributed) images between (interacting) reactants and product(s) of a given step. The convergence criteria are the same as for reaction energy calculations (forces $\leq$ 0.05 eV/ Å) with the same energy cutoff and the Brillouin zone is also sampled at the Γ point.

The PBE functional is known for underestimating barrier heights.[1-2] However, using more sophisticated DFT methods (e.g. M06 hybrid meta functional with a good accuracy "across-the board"[3]) with the plane wave basis employed for large systems under periodic boundary conditions is prohibitively expensive.[4] On the other hand, the relative activation energies obtained with standard DFT functionals such as PBE are reliable.[5]

It is important to note that the generality of the defect formation in crystalline ZIFs also depends on other factors such as temperature, pressure, heating rate and size of the particle.[6] Reaction energies and their associated barriers calculated here do not include vibrational free energy $F_{vib} = ZPE - TS_{vib}$, where ZPE is zero-point energy, T is temperature and S_{vib} is vibrational entropy, as well as configurational entropy TS_{conf}, which would be included in the free energy barriers $\Delta G^{\ddagger}(T) = \Delta E^{\ddagger} + \Delta F^{\ddagger}_{vib} - T\Delta S^{\ddagger}_{conf} + pV$. The calculations are performed in vacuum (p = 0 atm). Nevertheless observed here trends obtained from the electronic structure calculations are expected to be similar to those for the free energy calculations, because the Zn-N bond breaking process is dominated by energetic term.[7]

B.2 Surface Slab Models

ZIF surface slabs were generated and optimized with the same method described in Chapter 3. ZIF (001) surface slabs were generated by cleaving Zn-N bonds crossing the same planes in [001] direction. The thickness of slabs are c_0 (17.0 Å) and $c_0/2$ (12.2 Å) for ZIF-8 and ZIF-2, respectively. ZIF-8 (001) surface used a tetragonal cell with a base

defined by a_0[100] (17.0 Å) and b_0[010] (17.0 Å) with inter-layer spacing (distance in crystal direction between two adjacent Zn atoms) of $c_0/4$ (4.25 Å). The ZIF-2 (001) surface used a tetragonal cell with a base defined by $2a_0$[100] (19.3 Å) and b_0[010] (24.1 Å) with inter-layer spacing of ~$c_0/6$ (4.1 Å). Both ZIF-8 and ZIF-2 surface slab unit cells contain the same number of atoms as their bulk unit cells. Slabs were separated by a vacuum region of 20 Å in [001] direction from their periodic images to minimize their interactions. Dipole moment corrections were applied to all the slab calculations to eliminate the dipole interaction between periodic images. Due to their large unit cell size, we adopted asymmetric slab models for both ZIFs, with the atoms in the bottom two layers fixed at their equilibrium positions in bulk during geometry optimization.

All possible terminations of (001) surfaces were examined with their surface energy calculated for both ZIFs using equation 3.2, and the one with the lowest surface energy was used for the following study of surface reactions. Because the surfaces were generated by cleaving Zn-N bonds, both ZIF-2 and ZIF-8 have 3-coordinated Zn atoms on the external layer. Considering humid conditions, where H_2O has relatively high concentration, we coordinated the unsaturated Zn atoms with H_2O molecules by forming Zn-O bonds. By comparing the dangling linker formation reactions on hydrated surface and "clean" surface (3-coordinated Zn atoms at external layer) with the same reacting acid-gas molecule, we found that terminating water molecules played a role facilitating the reactions (decreasing the reaction energy $\Delta E_{rxn,DL}$ by 1~7 kcal/mol), but the relative stability of the surface to acid gases were not affected (Table B.4).

B.3 ZIF polymorphs

Table B.1 Aperture and cavity sizes of $Zn(mIM)_2$ polymorphs calculated by Zeo++[8-10]

Topology	Aperture size (Å)	Cavity size (Å)
dia	1.3	2.2
crb	4.0	5.9
sod	3.3	11.5
unc	4.8	5.1
cfc	3.3	5.2
gis	5.2	9.1
sra	6.4	7.0
pcl	5.5	7.8

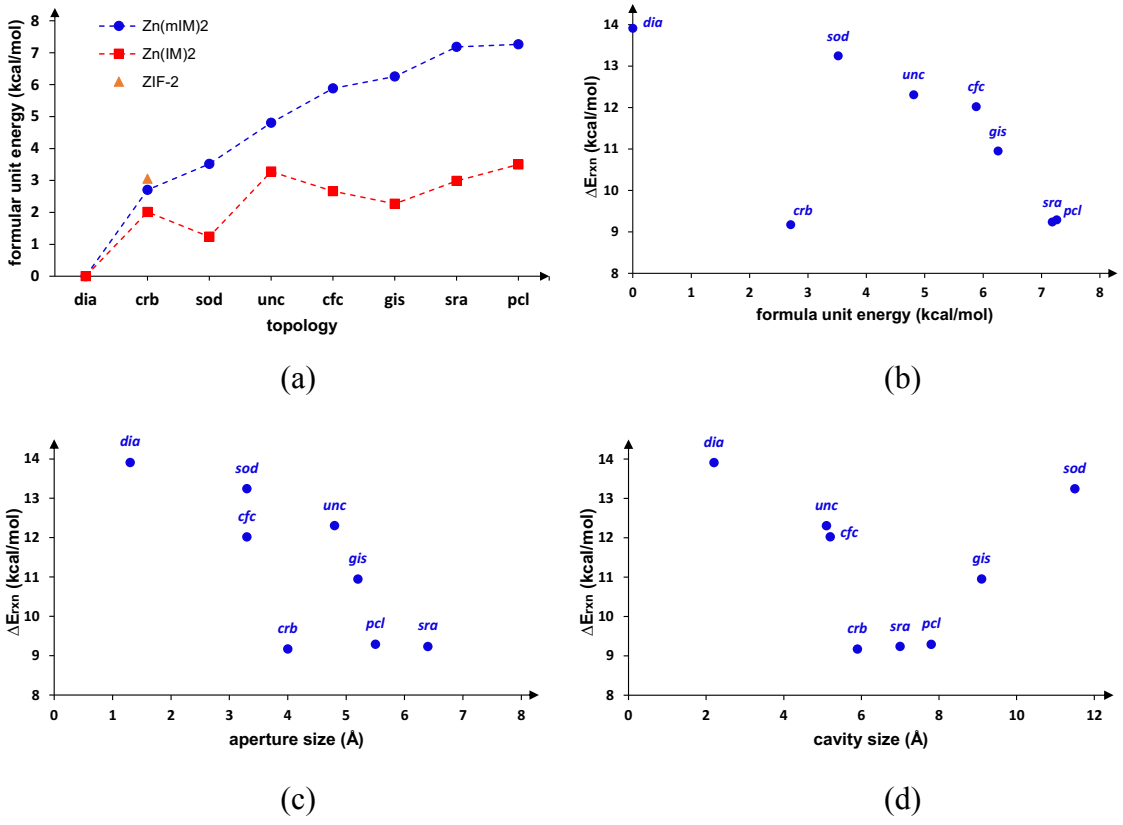

Figure B.1 (a) DFT calculated energies of a formula unit $Zn(IM)_2$/$Zn(mIM)_2$ related to that of *dia* topology, which is set to 0 for each set of polymorphs. ZIF-2 is labeled separately because it has cages of different shape from that of *crb* $Zn(IM)_2$. (b,c,d) Calculated reaction energy (ΔE_{rxn}) for the formation of a linker vacancy in $Zn(mIM)_2$ polymorphs vs. (b) the formula unit energy, (c) aperture size, and (d) cavity size. The topology for each data point is labeled.

B.4 Detailed energy profile for ZIF-8 LV formation with H_2O/H_2SO_X

Figure 4.5 shows comparison between energy profiles associated with LV formation reactions in ZIF-8 with H_2SO_3/H_2O and $H_2SO_4/H_2SO_3/H_2O$. To highlight the main steps affected by H_2SO_4 catalysis processes associated with the recovery of this acid, Figures B.2 and B.3 illustrate the catalytic and non-catalytic reactions. In these figures P_I corresponds to $ZIF_{DL}(HSO_x\text{--}HL)$, P_{II} corresponds to $ZIF_{LV}(HSO_x\text{--}H_2O)$, where x=3,4 depending which acid is involved in given defect formation and P_{III} correspond to $ZIF_{LV}(HSO_3{\bullet}H_2SO_4\text{--}H_2O)$.

H_2SO_4 does not need to be desorbed out of the system (in this case defective ZIF-8 framework), as this process is very endothermic (as it requires ~29 kcal/mol). This acid can remain physisorbed in the pores of the framework and catalyze further breaking of Zn-N bond(s). Thus, as indicated by a gray arrow in Figure B.2, one can consider thermodynamic cycle as starting from the interacting species (i.e., adsorbed H_2SO_4 in ZIF-8).

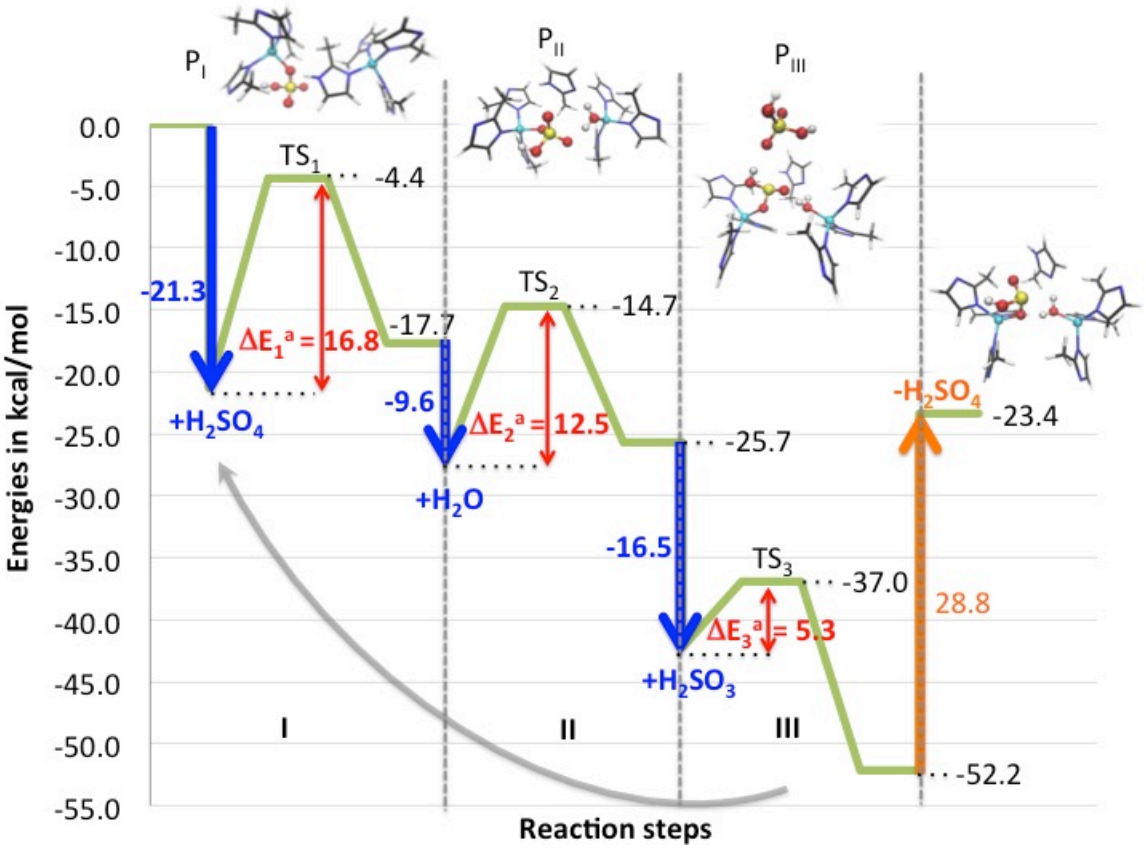

Figure B.2 The energy profile associated with a linker vacancy formation reaction in bulk ZIF-8 with H_2SO_3 catalyzed by H_2SO_4 in presence of water. Reference zero energy corresponds to the state of isolated ZIF-8 unit cell, H_2SO_3, H_2SO_4, and water molecules. Step I involves adsorption of a H_2SO_4 molecule from vacuum ($|\Delta E_{ads}|$ indicated in dark blue) into the pore, followed by formation of a dangling linker. Step II involves adsorption of a H_2O molecule, followed by formation of a linker vacancy. Step III is the adsorption of a H_2SO_3 molecule followed by the replacement of a H_2SO_4 molecule. This step can be treated as the last one in a thermodynamic cycle, where initial state and final state involves adsorbed H_2SO_4 in pristine and defective ZIF-8, respectively. This adsorbed H_2SO_4 may then participate in the same reactions for the next cycle, as indicated by the grey arrow. The H_2SO_4 desorption process (indicated by the orange arrow) and associated energy is necessary to show the full thermodynamic cycle as well as its catalytic character, as shown in Figure 4.5b, where step III and desorption are omitted and noted by purple asterisk. The energy barriers for step I, II, III are provided in red (noted as ΔE_1^a, ΔE_2^a, and ΔE_3^a, respectively), while the reaction energies are given in black. The values next to dotted lines provide transition state (TS_1, TS_2 and TS_3) energy levels for steps I, II, and III relative to reference energy, which is the energy level of interacting species for a given step. The structures P_I, P_{II}, and P_{III} shown at the top illustrate the products associated with steps I, II, and III, respectively. For clarity only the "active site" of the reaction is shown. H, C, N, O, S and Zn atoms are colored in white, black, blue, red, yellow and cyan, respectively.

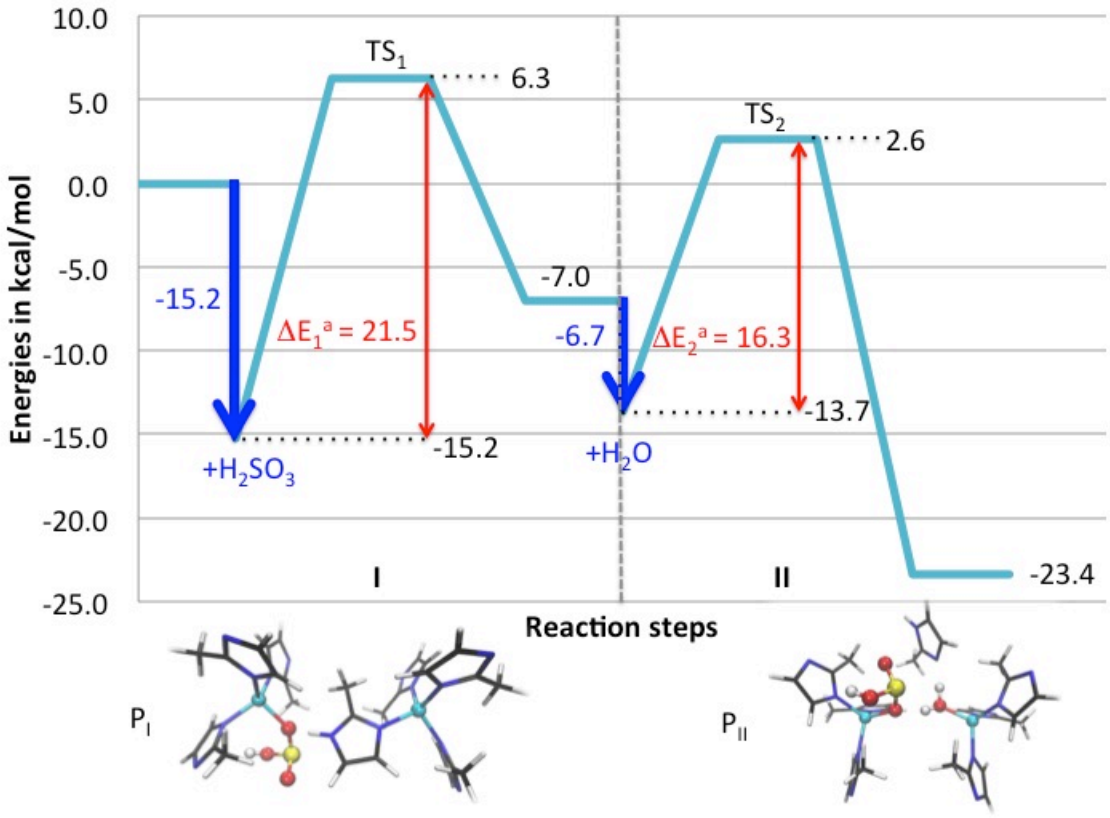

Figure B.3 The energy profile associated with a linker vacancy formation reaction in bulk ZIF-8 with H_2SO_3 in presence of water. Reference zero energy corresponds to the state of isolated ZIF-8 unit cell, H_2SO_3, and water molecules. Step I involves adsorption of a H_2SO_3 molecule ($|\Delta E_{ads}|$ indicated in dark blue) into the pore, followed by formation of a dangling linker. Step II involves adsorption of a H_2O molecule, followed by formation of a linker vacancy. The energy barriers for steps I and II are provided in red (denoted as ΔE_1^a and ΔE_2^a, respectively), while the reaction energies are given in black. The values next to dotted lines provide transition state (TS_1 and TS_2) energy levels for steps I and II relative to reference zero energy. The structures P_I and P_{II} shown at the bottom illustrate the products associated with steps I and II. For clarity only the "active site" of the reaction is shown. The color scheme for atoms is the same as in Figure B.2.

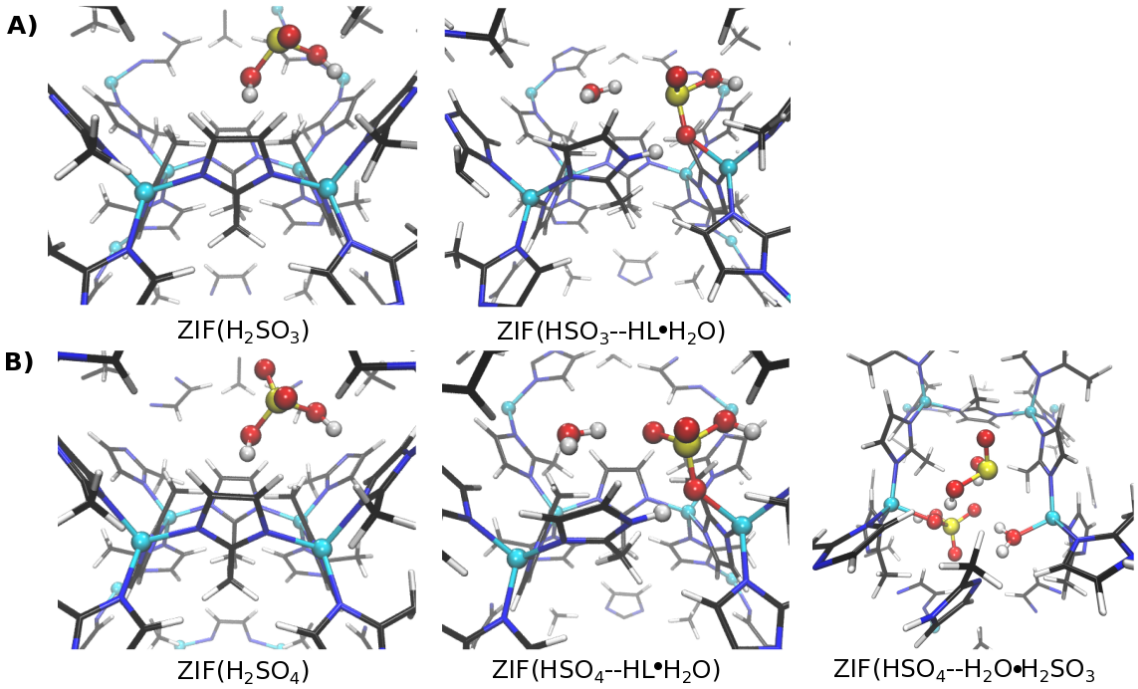

Figure B.4 Panel A) illustrates optimized structures of ZIF-8 bulk with physisorbed H_2SO_3 and H_2O in the pore of pristine and defective framework, respectively. Panel B) shows the same but for the H_2SO_4, water and H_2SO_3. In the case of the later ZIF-adsorbate system the sulfurous acid is physisorbed to framework with LV as point defect. For clarity the images were zoomed on the adsorption site. H, C, N, O, S and Zn atoms are colored in white, black, blue, red, yellow and cyan, respectively. ZIF(H_2SO_x) and ZIF(H_2SO_x--HL•H_2O) correspond to interacting reactants in DL and LV formation reaction, respectively, while ZIF(HSO_4--H_2O•H_2SO_3) in acid exchange.

B.5 Adsorption of water and acid gases to OMS in defective bulk ZIFs

Structural representations for unit cells of defective ZIF models (bulk and clean surfaces) with open metal sites (OMS) are illustrated in Figure B.5. The optimized geometrical configurations of adsorbed acid gases to the defective bulk ZIF-2 and ZIF-8 are shown in Figures B.6 and B.7, respectively. In addition, we studied the adsorption of these acid gases to defective SALEM-2 (which has the same topology of ZIF-8 but the organic ligands of ZIF-2). This was done to investigate steric effects on the strength of adsorption in a similar fashion as it was done for reactivity of ZIFs. Optimized SALEM-2-adsorbate structures are presented in Figure B.8.

In bulk ZIF-2 and ZIF-8 with a pair of OMS, molecules such as H_2O or H_2S may only bind to one of the OMS via either O or S, respectively. Acid gases with potential for multidentate binding (e.g., HNO_3, SO_2, and NO) can bridge between the two unsaturated Zn ions by forming Zn-O(N) bonds. Interestingly, when H_2SO_4 and HNO_3 formed this "bridging" motif (Figures B.6—B.8), their geometries resemble closely that before adsorption. We refer to this as molecular configuration and noted it by "m" at front of the chemical formula (e.g. mH_2SO_4) to distinguish it from a dissociative configuration, which H_2SO_4, HNO_3, H_2S, and H_2SO_3 could form, noted by "d".

In fact, the only stable structure for H_2SO_3 in both ZIFs was dH_2SO_3. In this case its OH group bonded to one of the OMS and its remaining fragment to the other OMS via O. H_2SO_4 and HNO_3 behave very similarly in case of dissociative adsorption. Table B.2 lists the adsorption energies (ΔE_{ads}) of all the studied acid-gas molecules on OMS in bulk ZIF-2 and ZIF-8. We can see that for the molecules that can dissociate upon adsorption, $|\Delta E_{ads}|$ for dissociative configuration is more thermodynamically favorable. This is

because a more stable defective ZIF-adsorbate species is formed due to stronger bonding between Zn and O of the aforementioned fragments.

The general trend is that defective bulk ZIF-2 binds stronger than ZIF-8. The only exception from this is $mHNO_3$. The possible explanation for this outlier is that ZIF-8 forms additional (stabilizing) hydrogen bonds (HB) while ZIF-2 does not. Indeed we also find these in defective SALEM-2, albeit this ZIF forms one less HB than ZIF-8. Adsorption energy values for SALEM-2 are usually found between those for ZIF-2 and ZIF-8. This general observation suggests that the topology and the linker size have an effect on adsorption. However, these effects are of a smaller magnitude than those noted for reaction energies. We attribute this to the presence of OMS, which eliminates to some extent steric effect. This conclusion is somewhat supported by the results obtained for adsorption to clean surfaces of ZIF-2 and ZIF-8 (Table B.3). Note that in this case other processes such as surface relaxation play a role as well.

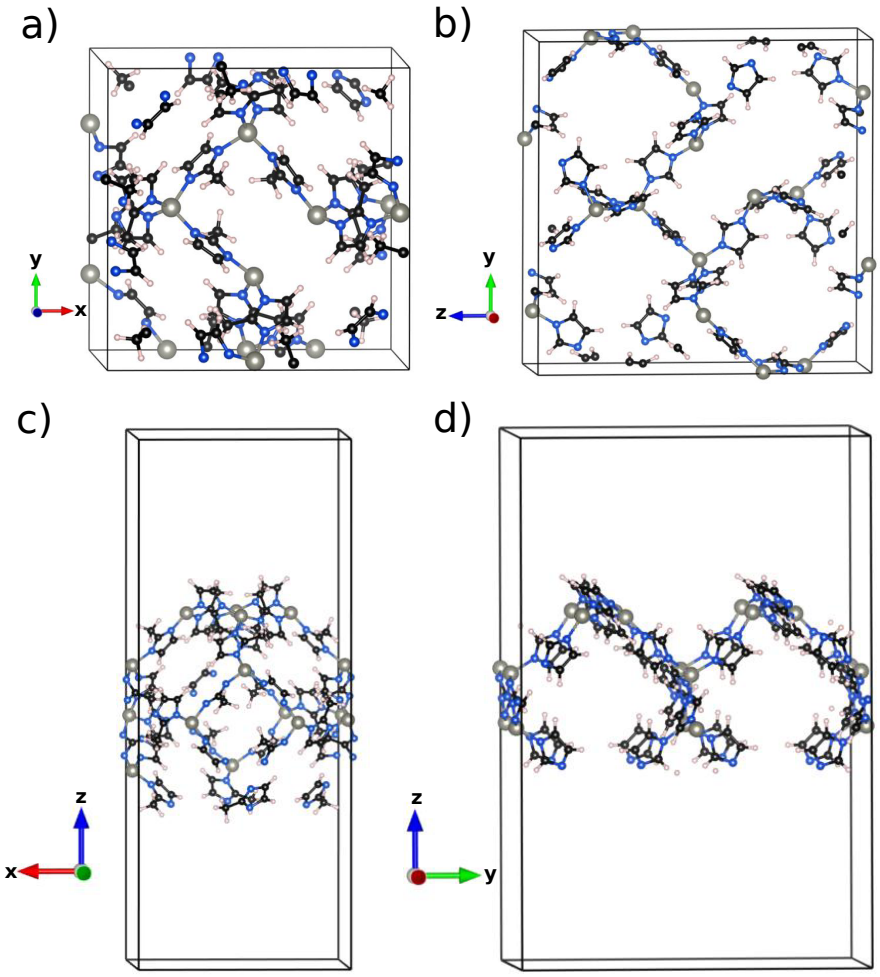

Figure B.5 Bulk (a and b) and surface slab (c and d) models of ZIF-8 (a and c) and ZIF-2 (b and d) with OMS. Solid lines indicate the simulation volume in each case. H/C/N/Zn atoms are shown in white/black/blue/grey, respectively.

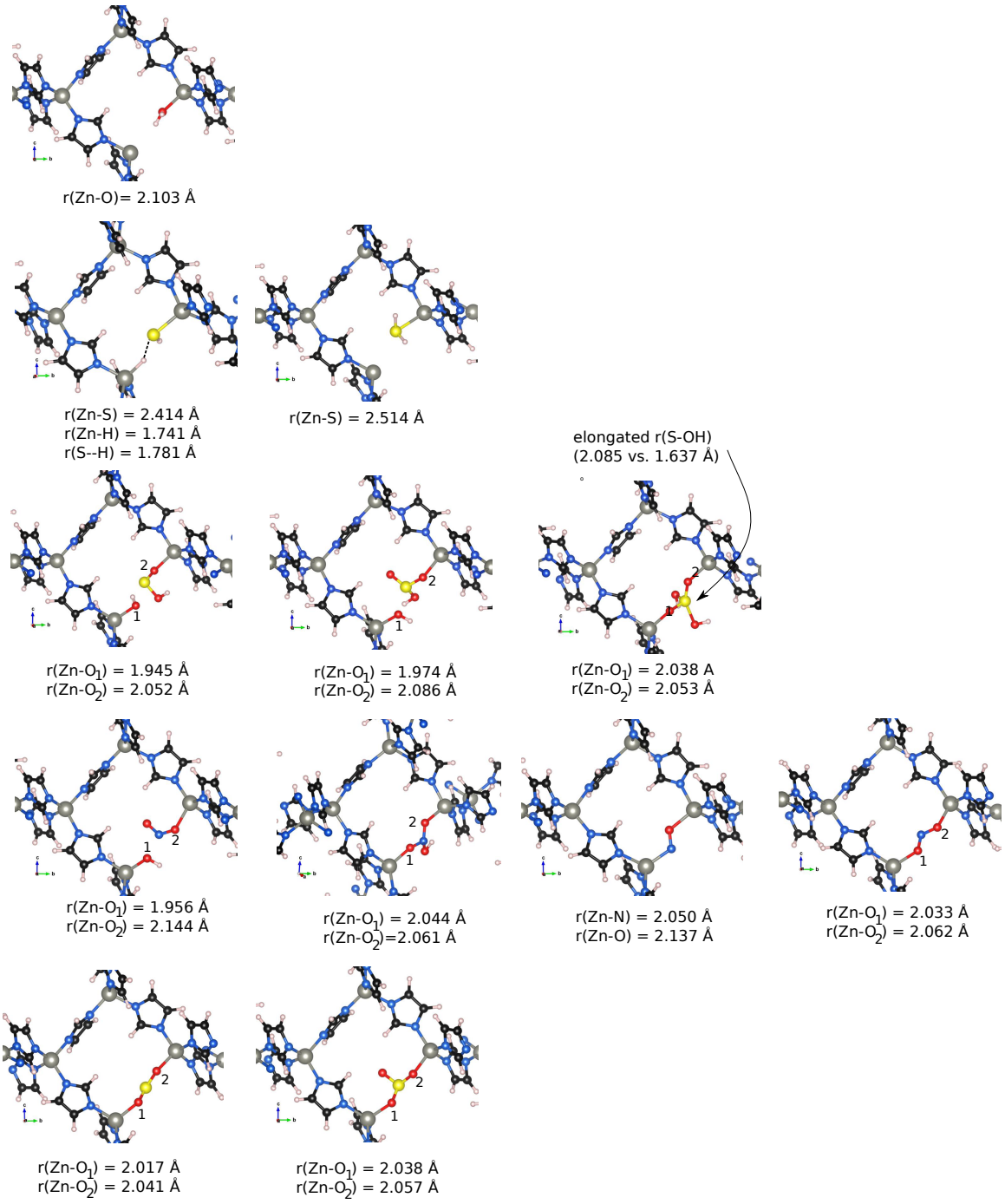

Figure B.6 Optimized structures of defective bulk ZIF-2 with chemisorbed H_2O (1st row), H_2S (2nd row) dissociative on the left hand site (l.h.s.) and molecular on right hand site (r.h.s), dH_2SO_3 on the l.h.s, dH_2SO_4 in the middle and mH_2SO_4 on the r.h.s (3rd row), $dHNO_3$ on the most l.h.s, $mHNO_3$ and NO in the middle and NO_2 on the most r.h.s (4th row), SO_2 on the l.h.s and SO_3 on the r.h.s (5th row). H/C/N/O/S/Zn atoms are shown in white/black/blue/red/yellow/grey, respectively.

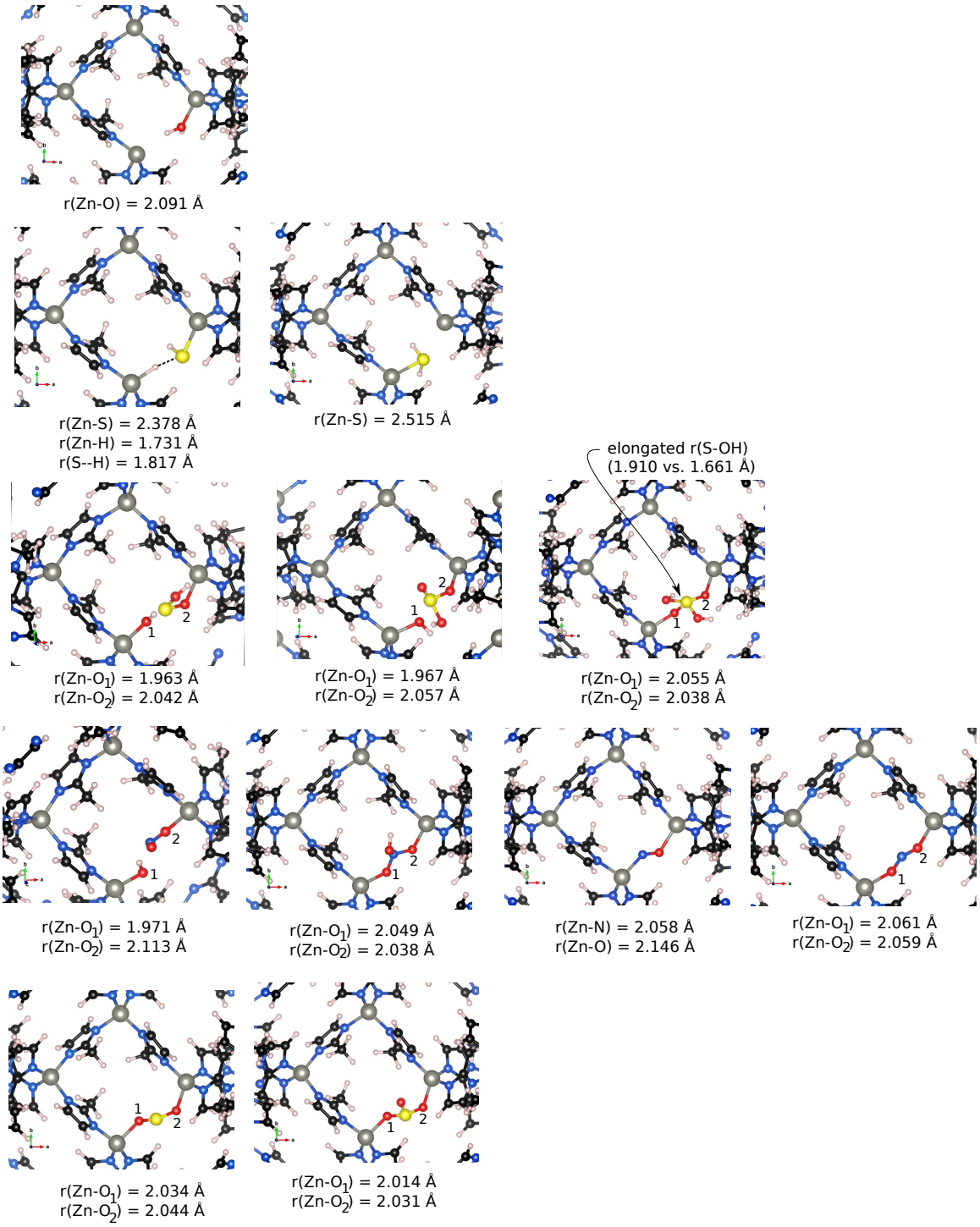

Figure B.7 Optimized structures of defective bulk ZIF-8 with chemisorbed H_2O (1st row), H_2S (2nd row) dissociative on the left hand site (l.h.s.) and molecular on right hand site (r.h.s), dH_2SO_3 on the l.h.s, dH_2SO_4 in the middle and mH_2SO_4 on the r.h.s (3rd row), $dHNO_3$ on the most l.h.s, $mHNO_3$ and NO in the middle and NO_2 on the most r.h.s (4th row), SO_2 on the l.h.s and SO_3 on the r.h.s (5th row). Color scheme is the same as in Figure B.6.

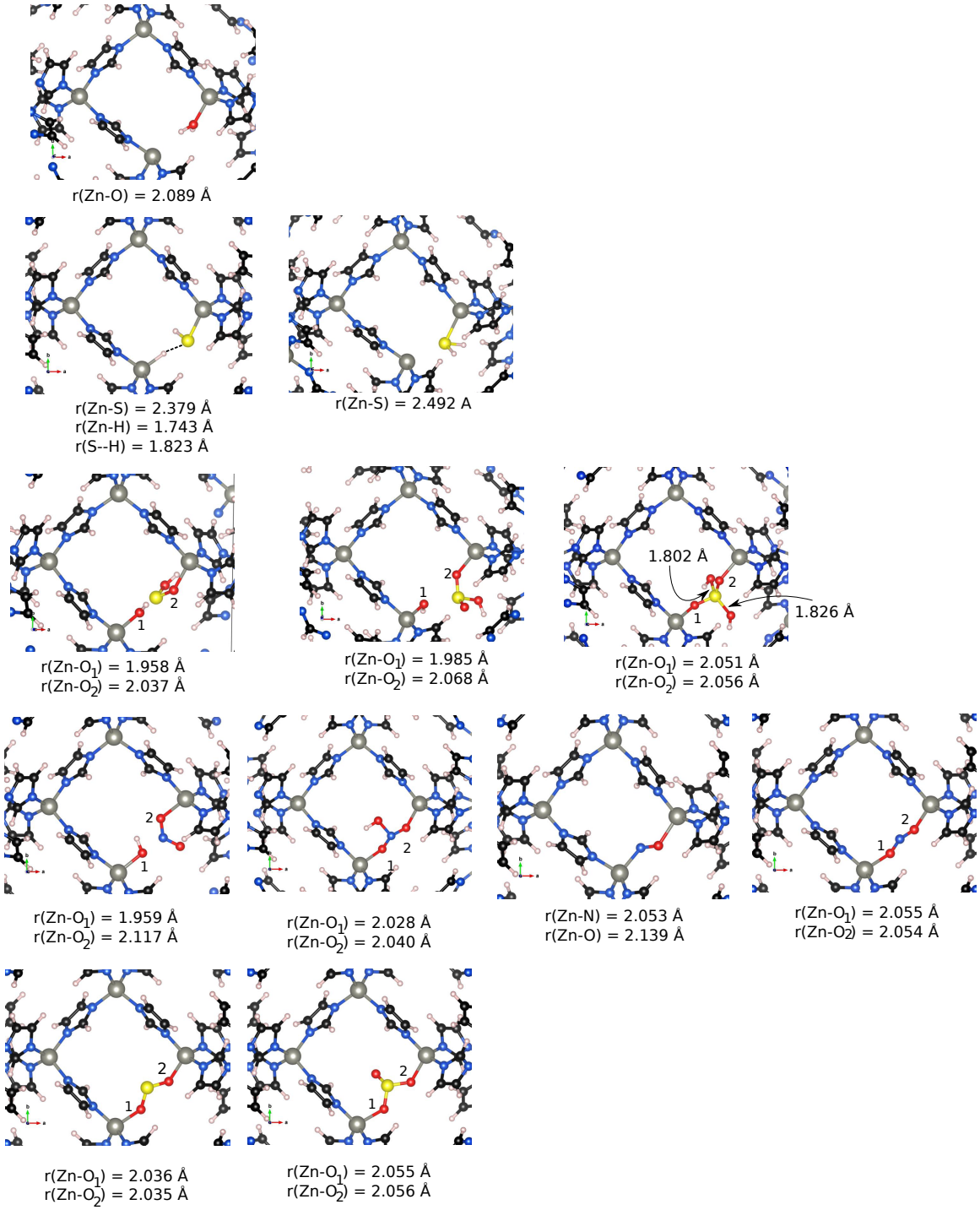

Figure B.8 Optimized structures of defective bulk SALEM-2 with chemisorbed H_2O (1st row), H_2S (2nd row) dissociative on the left hand site (l.h.s.) and molecular on right hand site (r.h.s), dH_2SO_3 on the l.h.s, dH_2SO_4 in the middle and mH_2SO_4 on the r.h.s (3rd row), $dHNO_3$ on the most l.h.s, $mHNO_3$ and NO in the middle and NO_2 on the most r.h.s (4th row), SO_2 on the l.h.s and SO_3 on the r.h.s (5th row). Color scheme is the same as in Figure B.6.

Table B.2 Adsorption energies (in kcal/mol) of molecules at OMS in bulk ZIFs (configurations in Figures B.6—B.8). Letters "m" denotes molecule and "d" denotes dissociative molecule.

Adsorbate	ZIF-2	ZIF-8	SALEM-2
H_2O	-27.0	-25.0	-26.0
mH_2S	-18.7	-17.2	-18.5
dH_2S	-34.1	-33.5	-33.0
SO_2	-73.6	-71.7	-73.0
SO_3	-87.7	-83.7	-85.8
NO	-53.6	-52.5	-53.6
NO_2	-100.1	-99.3	-100.3
dH_2SO_3	-55.2	-53.7	-54.8
mH_2SO_4	-53.1	-45.8	-51.6
dH_2SO_4	-61.7	-52.9	-57.6
$mHNO_3$	-57.1	-60.2	-59.1
$dHNO_3$	-71.0	-66.9	-68.8

Table B.3 Adsorption energies (in kcal/mol) of molecules at OMS of ZIF (001) surfaces

Adsorbate	ZIF-2	ZIF-8
H_2O	-14.5	-15.0
H_2S	-12.9	-13.5
H_2SO_3	-20.6	-15.5
H_2SO_4	-20.5	-29.1
SO_2	-44.6	-54.4
SO_3	-80.1	-85.2

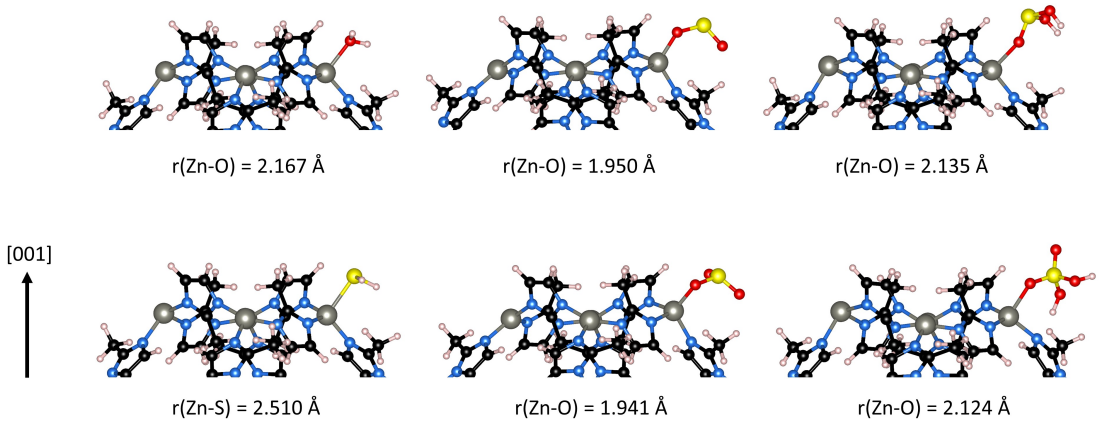

Figure B.9 Optimized structures of clean ZIF-8 surface with chemisorbed H_2O, SO_2, H_2SO_3, H_2S, SO_3, and H_2SO_4 at the OMS in top layer from left to right and from the 1st to 2nd row, respectively. Color scheme is the same as in Figure B.6.

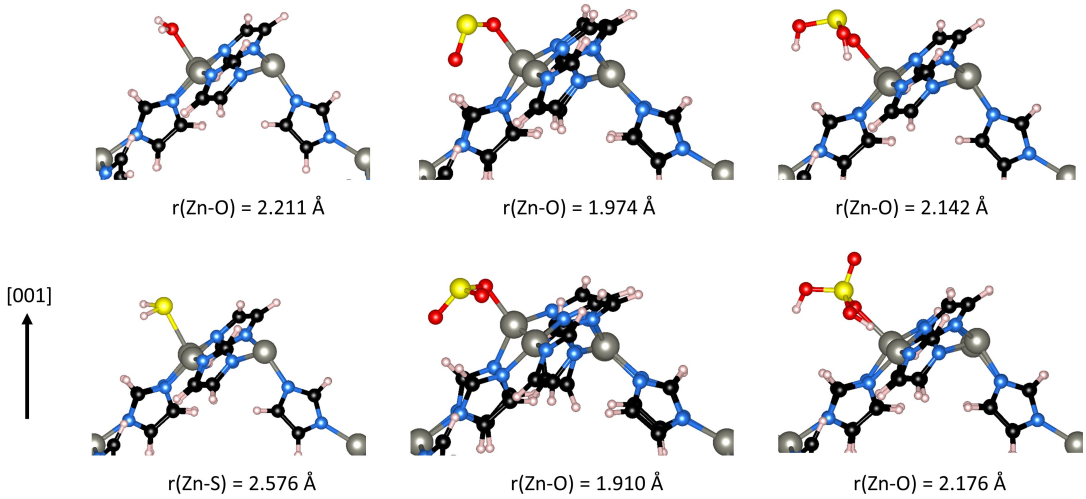

Figure B.10 Optimized structures of clean ZIF-2 surface with chemisorbed H_2O, SO_2, H_2SO_3, H_2S, SO_3, and H_2SO_4 at the OMS in top layer from left to right and from the 1st to 2nd row, respectively. Color scheme is the same as in Figure B.6.

B.6 Structures of ZIF surfaces reacting with H_2SO_x

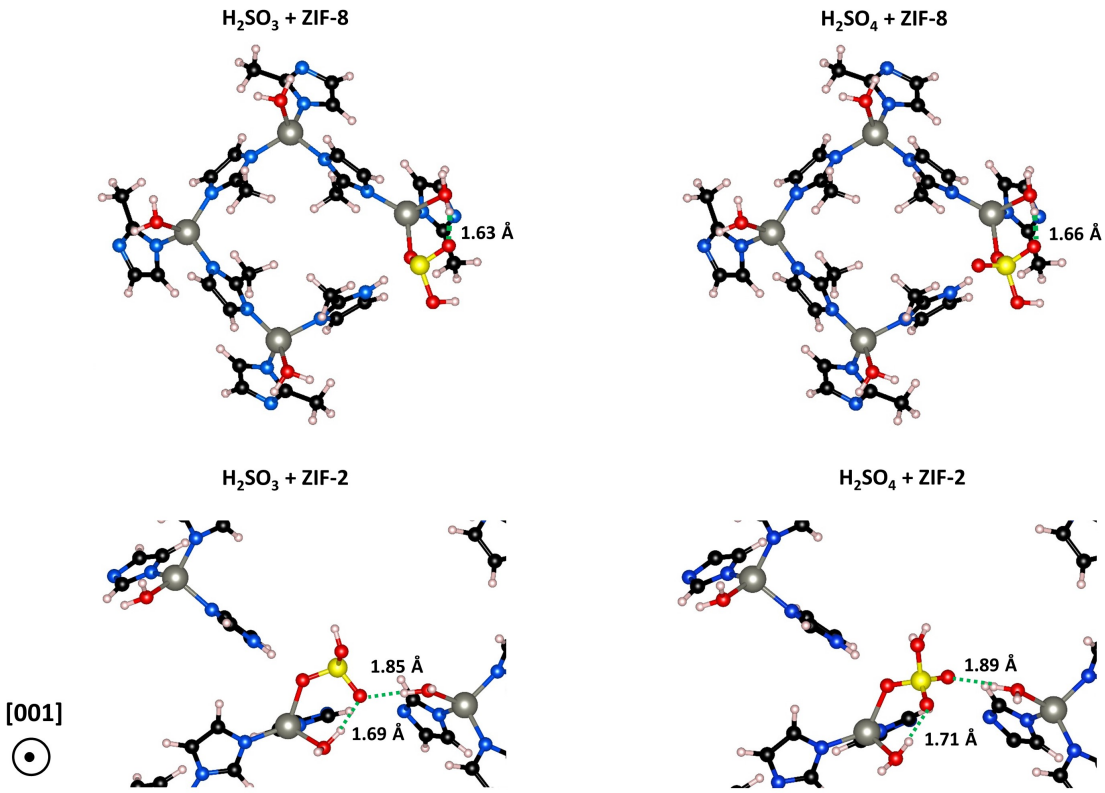

Figure B.11 Optimized structures of dangling linkers formed on (001) ZIF-8 (top) and ZIF-2 (bottom) hydrated surfaces induced by H_2SO_3 (left) and H_2SO_4 (right). The interacting oxygen atom of the H_2SO_x molecule and hydrogen atom(s) of terminating water molecule(s) are connected by the green dashed segments with their distances labeled. Color scheme is the same as in Figure B.6.

Table B.4 Reaction energy ($\Delta E_{rxn,DL}$ in Eq. 4.1) in kcal/mol for the formation of a dangling linker induced by H_2O, H_2S, H_2SO_3, H_2SO_4, SO_2, and SO_3 on clean ZIF (001) surfaces.

Reactant	ZIF-2	ZIF-8
H_2O	-4.5	-4.2
H_2S	-17.7	-17.1
H_2SO_3	-15.1	-16.5
H_2SO_4	-24.0	-23.9
SO_2	4.4	4.6
SO_3	-22.2	-18.6

B.7 References

(1) Perdew, J. P.; Ruzsinszky, A.; Tao, J. M.; Staroverov, V. N.; Scuseria, G. E.; Csonka, G. I., Prescription for the design and selection of density functional approximations: More constraint satisfaction with fewer fits. *J. Chem. Phys.* **2005,** *123* (6).

(2) Zhao, Y.; Gonzalez-Garcia, N.; Truhlar, D. G., Benchmark database of barrier heights for heavy atom transfer, nucleophilic substitution, association, and unimolecular reactions and its use to test theoretical methods. *J. Phys. Chem. A* **2005,** *109* (9), 2012-2018.

(3) Zhao, Y.; Truhlar, D. G., Density functionals with broad applicability in chemistry. *Acc. Chem. Res.* **2008,** *41* (2), 157-167.

(4) Svelle, S.; Tuma, C.; Rozanska, X.; Kerber, T.; Sauer, J., Quantum Chemical Modeling of Zeolite-Catalyzed Methylation Reactions: Toward Chemical Accuracy for Barriers. *J. Am. Chem. Soc.* **2009,** *131* (2), 816-825.

(5) Hartley, M. K.; Vine, S.; Walsh, E.; Avrantinis, S.; Daub, G. W.; Cave, R. J., Comparison of Relative Activation Energies Obtained by Density Functional Theory and the Random Phase Approximation for Several Claisen Rearrangements. *J. Phys. Chem. B* **2016,** *120* (8), 1486-1496.

(6) Gaillac, R.; Pullumbi, P.; Beyer, K. A.; Chapman, K. W.; Keen, D. A.; Bennett, T. D.; Coudert, F. X., Liquid metal-organic frameworks. *Nat. Mater.* **2017,** *16* (11), 1149-1154.

(7) Gaillac, R.; Pullumbi, P.; Coudert, F. X., Melting of Zeolitic Imidazolate Frameworks with Different Topologies: Insight from First-Principles Molecular Dynamics. *J. Phys. Chem. C* **2018,** *122* (12), 6730-6736.

(8) Willems, T. F.; Rycroft, C.; Kazi, M.; Meza, J. C.; Haranczyk, M., Algorithms and tools for high-throughput geometry-based analysis of crystalline porous materials. *Microporous Mesoporous Mater.* **2012,** *149* (1), 134-141.

(9) Martin, R. L.; Smit, B.; Haranczyk, M., Addressing Challenges of Identifying Geometrically Diverse Sets of Crystalline Porous Materials. *J. Chem. Inf. Model.* **2012,** *52* (2), 308-318.

(10) Pinheiro, M.; Martin, R. L.; Rycroft, C. H.; Jones, A.; Iglesia, E.; Haranczyk, M., Characterization and comparison of pore landscapes in crystalline porous materials. *J. Mol. Graphics Modell.* **2013,** *44*, 208-219.

APPENDIX C: SUPPORTING INFORMATION FOR CHAPTER 5

C.1 Force Field Parameters for Defective ZIF-8 Crystals

The flexible force field (FF) parameters and atomic charges for pristine ZIF-8 used in this study are adopted from Zhang *et al.*[1] Pristine ZIF-8 has seven types of atoms, which are Zn, N, C1, C2, C3, H1, and H2, as shown in Figure C.1a. For the defective structures dangling linker and linker vacancy, new atom types (O1, H3, H4, and N2 for dangling linker, O2, H5, H6 for linker vacancy) and associated bond, angle, and torsion types are added (Figure C.1).

The FF parameters for Zn-O bonds, O-H bonds, and N-Zn-O angles are from the MOF-FF developed by Bureekaew *et al.*,[2] where the FF expressions for bond stretching and bending adopt MM3 approaches that have four- and six-order polynomial forms, respectively. Due to that the polynomial terms higher than quadratic terms have weak contributions, here we use the form of harmonic bond stretching and bending as well as the force constants from MOF-FF to keep consistence with the FF parameters used in pristine ZIF-8. H-O-H angles adopt FF parameters of SPC/Fw water model.[3] N-H bonds, C-N-H angles, and X-C-N-Y (X, Y can be C, H, and N) torsions adopt general AMBER FF (GAFF).[4-5] Zn-O-H angles are rigid and maintain their equilibrium angles. The equilibrium values for bond length and angles are from DFT optimized structures. Part of bonds, angles, and torsions on the defects have same components with that in pristine ZIF-8, so they are assigned the same FF parameters, as labeled in Table C.1.

UFF parameters are used for the van der Waals (VDW) parameters for all the new atom types in defective structures (Table C.2). The charges of these atoms are scaled from the DDEC charges calculated with DFT-D3 method. The charges are scaled to keep the defective ZIF-8 framework charge neutral while the seven atom types of pristine ZIF-8 retain their original charges.

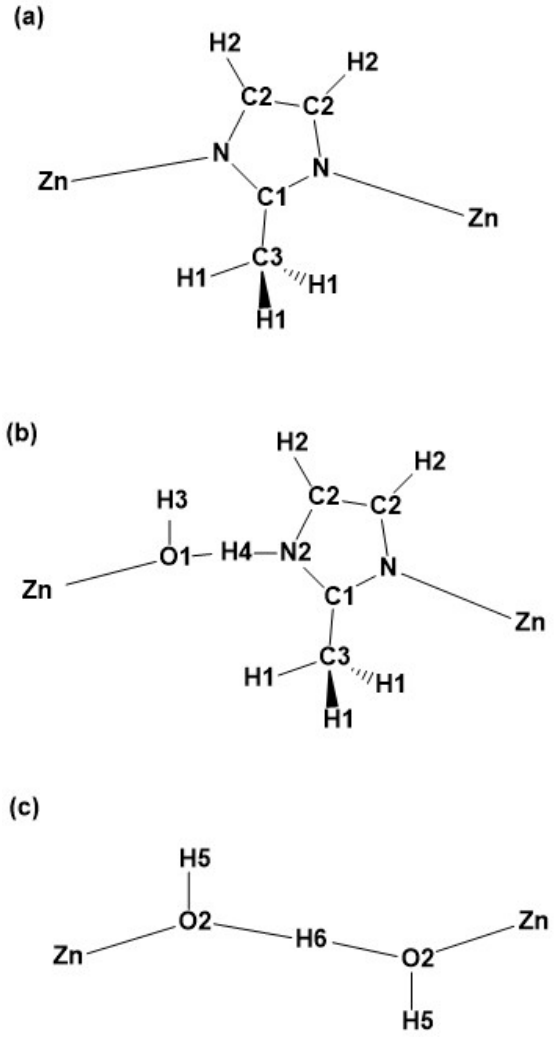

Figure C.1 Atom types of (a) defect-free ZIF-8 and defective ZIF-8 with (b) dangling linker and (c) linker vacancy.

Table C.1 Force field parameters* for defective structures in Figure C.1b and C.1c

Bond Stretching $U_{streching,Harmonic} = k_r(r - r_0)^2$ $U_{stretching,Morse} = D\left[1 - e^{-\alpha(r-r_0)}\right]^2$			
Zn-O1	Morse	D = 50.0 kcal/mol, α = 1.46 $Å^{-1}$, r_0 = 1.970 Å	Bureekaew *et al.*
Zn-O2	Morse	D = 50.0 kcal/mol, α = 1.46 $Å^{-1}$, r_0 = 2.000 Å	
O1-H3	Harmonic	k_r = 394.5 kcal/(mol·$Å^2$), r_0 = 0.970 Å	
O1-H4	Harmonic	k_r = 394.5 kcal/(mol·$Å^2$), r_0 = 1.380 Å	
O2-H5	Harmonic	k_r = 394.5 kcal/(mol·$Å^2$), r_0 = 0.971 Å	
O2-H6	Harmonic	k_r = 394.5 kcal/(mol·$Å^2$), r_0 = 1.208 Å	
N2-H4	Harmonic	k_r = 406.6 kcal/(mol·$Å^2$), r_0 = 1.13 Å	GAFF
N2-C1	Harmonic	k_r = 488.0 kcal/(mol·$Å^2$), r_0 = 1.339 Å	Same as N-C1
N2-C2	Harmonic	k_r = 410.0 kcal/(mol·$Å^2$), r_0 = 1.371 Å	Same as N-C2
Bond Bending $U_{bending} = k_\theta(\theta - \theta_0)^2$			
N-Zn-O1	Harmonic	k_θ = 6.3 kcal/(mol·rad^2), θ_0 = 107.2	Bureekaew *et al.*
N-Zn-O2	Harmonic	k_θ = 6.3 kcal/(mol·rad^2), θ_0 = 109.2	
H3-O1-H4	Harmonic	k_θ = 38.0 kcal/(mol·rad^2), θ_0 = 115.7	Wu *et al.*
H5-O2-H6	Harmonic	k_θ = 38.0 kcal/(mol·rad^2), θ_0 = 107.5	
C1-N2-H4	Harmonic	k_θ = 47.2 kcal/(mol·rad^2), θ_0 = 123.6	GAFF
C2-N2-H4	Harmonic	k_θ = 47.2 kcal/(mol·rad^2), θ_0 = 127.5	
C1-N2-C2	Harmonic	k_θ = 70.0 kcal/(mol·rad^2), θ_0 = 105.2	Same as C1-N-C2
N2-C2-H2	Harmonic	k_θ = 50.0 kcal/(mol·rad^2), θ_0 = 125.7	Same as N-C2-H2
N2-C2-C2	Harmonic	k_θ = 70.0 kcal/(mol·rad^2), θ_0 = 108.7	Same as N-C2-C2
N2-C1-C3	Harmonic	k_θ = 70.0 kcal/(mol·rad^2), θ_0 = 123.9	Same as N-C1-C3
N2-C1-N	Harmonic	k_θ = 70.0 kcal/(mol·rad^2), θ_0 = 112.2	Same as N-C1-N
Proper Torsions $U_{charmm} = K[1 + \cos(n\phi - d)]$			
C3-C1-N2-H4	charmm	K=6.8 kcal/mol, n=2, d=180	GAFF
H2-C2-N2-H4	charmm	K=6.8 kcal/mol, n=2, d=180	
C2-C2-N2-H4	charmm	K=6.8 kcal/mol, n=2, d=180	
N-C1-N2-H4	charmm	K=6.8 kcal/mol, n=2, d=180	
N2-C2-C2-H2	charmm	K=4.0 kcal/mol, n=2, d=180	Same as N-C2-C2-H2
N2-C2-C2-N	charmm	K=4.0 kcal/mol, n=2, d=180	Same as N-C2-C2-N
N2-C1-N-Zn	charmm	K=0.1 kcal/mol, n=2, d=180	Same as N-C1-N-Zn
N2-C1-N-C2	charmm	K=4.8 kcal/mol, n=2, d=180	Same as N-C1-N-C2
N-C1-N2-C2	charmm	K=4.8 kcal/mol, n=2, d=180	Same as N-C1-N-C2
Improper Torsions			
C3-N2-C1-N	charmm	K=1.1 kcal/mol, n=2, d=180	same as C3-N-C1-N
C2-H2-C2-N2	charmm	K=1.1 kcal/mol, n=2, d=180	Same as C2-H2-C2-N

*equilibrium bond lengths (r_0) and angles (θ_0) are optimized by DFT calculations

Table C.2 Lennard-Jones potential parameters and atomic charges of atoms of defective structures in Figures C.1b and C.1c

Atom	σ (Å)	ε (kcal/mol)	q (e)
O1	3.118	0.0600	-0.540
O2	3.118	0.0600	-0.598
H3	2.571	0.0440	+0.243
H4	2.571	0.0440	+0.197
H5	2.571	0.0440	+0.275
H6	2.571	0.0440	+0.301
N2	3.261	0.0373	-0.180

C.2 Window Size Distributions for Defective ZIF-8

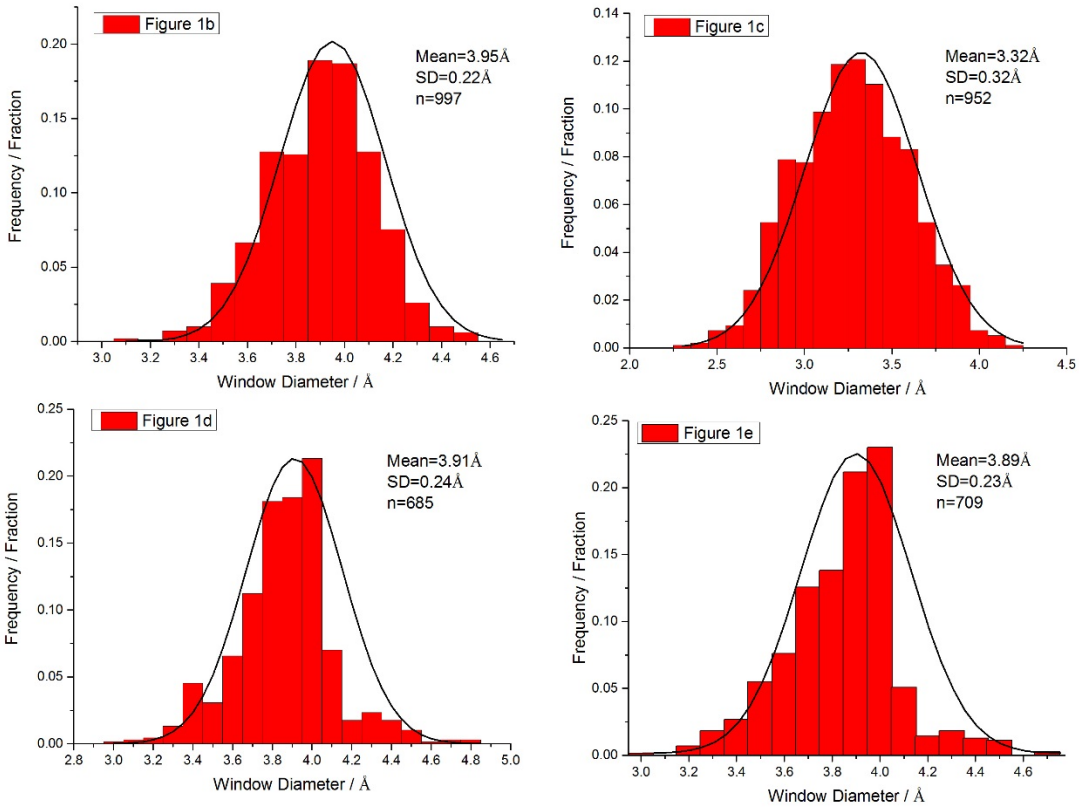

Figure C.2 Defective ZIF-8 window size distribution at 35 ^{o}C for configurations without adsorbates contained. The configurations of defective windows are shown in Figure 5.1 of Chapter 5.

C.3 Force Field Parameters for Adsorbates

Table C.3 Lennard-Jones potential parameters, and atomic charges for acid-gas adsorbates

Adsorbate	LJ Sites	σ (Å)	ε (kcal/mol)	q (e)
CH_4 [6]	CH_4	3.730	0.2941	0.0
C_2H_6 [6]	2×CH_3	3.750	0.1947	0.0
C_3H_8 [6]	2×CH_3	3.750	0.1947	0.0
	CH_2	3.950	0.0914	0.0
n-C_4H_{10} [6]	2×CH_3	3.750	0.1947	0.0
	2×CH_2	3.950	0.0914	0.0
iso-C_4H_{10} [6]	2×CH_3	3.750	0.1947	0.0
	CH	4.680	0.0199	0.0
CO_2 [7]	C	2.757	0.0559	+0.6512
	2 × O	3.033	0.1600	-0.3256
H_2O [3]	O	3.165	0.1554	-0.8476
	2 × H	-	0.0	+0.4238
H_2S [8]	S	3.720	0.4610	-0.3800
	2 × H	-	0.0	+0.1900
SO_2 [9]	S	3.390	0.1467	+0.5900
	2 × O	3.050	0.1570	-0.2950
NO_2 [10]	N	3.240	0.1001	+0.1460
	2 × O	2.930	0.1242	-0.0730
NO [10]	N	3.014	0.1580	+0.0288
	O	2.875	0.1926	-0.0288

Table C.4 Bond stretching and bending force field parameters of acid-gas adsorbates

Adsorbate	Bond Stretching $U_{streching} = k_r(r - r_0)^2$		Bond Bending $U_{bending} = k_\theta(\theta - \theta_0)^2$	
	k_r [kcal/(mol·Å^2)]	r_0 [Å]	k_θ [kcal/(mol·rad^2)]	θ_0 [degree]
H_2O [3]	∞	1.000	∞	109.5
H_2S [8]	∞	1.340	32.6	92.5
SO_2 [9]	∞	1.432	55.0	119.3
NO_2 [10]	∞	1.200	∞	134.3
NO [10]	∞	1.150	-	-

C.4 Free Energy Barriers, Dynamical Correction Factors, and Self-Diffusion Coefficients of Investigated Adsorbates in Pristine and Defective ZIF-8

Table C.5 Free energy barriers (in kJ/mol) for a single adsorbate molecule hopping through different types of windows at 35 ^{o}C. The window types are shown in Figure 5.1.

Adsorbate	(a) pristine	(b) dangling linker	(c) dangling linker	(d) vacancy	(e) vacancy
CH_4	24.87	13.08	20.34	10.91	24.41
C_2H_6	31.72	17.51	24.76	14.13	30.61
C_3H_8	42.38	22.58	30.67	18.05	39.45
n-C_4H_{10}	43.32	22.41	30.23	18.00	40.12
iso-C_4H_{10}	70.04	44.88	50.75	34.46	65.14
H_2O	13.56	9.73	12.20	7.16	13.63
CO_2	19.92	14.76	16.57	11.47	17.01
H_2S	25.88	13.63	19.20	9.93	25.31
SO_2	24.35	16.16	19.44	12.60	24.24
NO	17.00	10.09	13.82	7.83	14.71
NO_2	18.89	11.81	17.03	9.78	18.42

Table C.6 Transmission coefficients for adsorbates hopping through different types of windows at 35 ^{o}C

Adsorbate	(a) pristine	(b) dangling linker	(c) dangling linker	(d) vacancy	(e) vacancy
CH_4	0.6356	0.7953	0.6294	0.8638	0.6882
C_2H_6	0.7921	0.8022	0.7474	0.8329	0.7297
C_3H_8	0.3816	0.6727	0.5393	0.7911	0.4557
n-C_4H_{10}	0.5656	0.6290	0.5515	0.7106	0.6099
iso- C_4H_{10}	0.0478	0.1428	0.1399	0.5743	0.1091
H_2O	0.8447	0.9032	0.7448	0.7569	0.8910
CO_2	0.7070	0.8819	0.7607	0.8772	0.8338
H_2S	0.7975	0.9484	0.5811	0.8735	0.8021
SO_2	0.6145	0.9158	0.6151	0.8668	0.7261
NO	0.8954	0.9263	0.9468	0.8764	0.9673
NO_2	0.7283	0.8583	0.8228	0.9175	0.9182

Table C.7 Hopping rates (in s^{-1}) of adsorbates hopping through different types of windows at 35 ^{o}C

Adsorbate	(a) pristine	(b) dangling linker	(c) dangling linker	(d) vacancy	(e) vacancy
CH_4	9.53E+06	1.04E+09	6.24E+07	2.86E+09	1.15E+07
C_2H_6	6.72E+05	1.71E+08	8.48E+06	6.76E+08	8.70E+05
C_3H_8	4.39E+03	1.61E+07	4.99E+05	1.16E+08	1.43E+04
n-C_4H_{10}	3.47E+03	1.37E+07	5.51E+05	9.82E+07	1.43E+04
iso- C_4H_{10}	9.35E-03	7.16E+02	8.11E+01	1.21E+05	1.75E-01
H_2O	8.64E+08	3.96E+09	1.32E+09	9.27E+09	1.04E+09
CO_2	6.42E+07	4.02E+08	2.37E+08	1.57E+09	1.61E+08
H_2S	5.88E+06	8.12E+08	5.23E+07	2.99E+09	7.32E+06
SO_2	4.26E+06	2.47E+08	3.21E+07	8.14E+08	7.37E+06
NO	2.08E+08	3.15E+09	7.18E+08	6.18E+09	5.05E+08
NO_2	6.89E+07	1.22E+09	1.54E+08	2.63E+09	9.55E+07

C.5 The Influence of Free 2-Methylimidazole Molecule on Diffusion

The position of the adsorbed 2-methylimidazole molecule in ZIF-8 is illustrated in Figure C.3. Because the molecule sits at one side of the defective window, the symmetry of the neighboring cages is broken, resulting in asymmetric free energy profiles (Figure C.4). The asymmetric free energy profile indicates different energy barriers for an adsorbate approaching TS from either cage. The difference in the energy barrier from both cages yields 1 and 3 orders of magnitudes difference in self-diffusion coefficient for H_2S and isobutane, respectively (Table C.8).

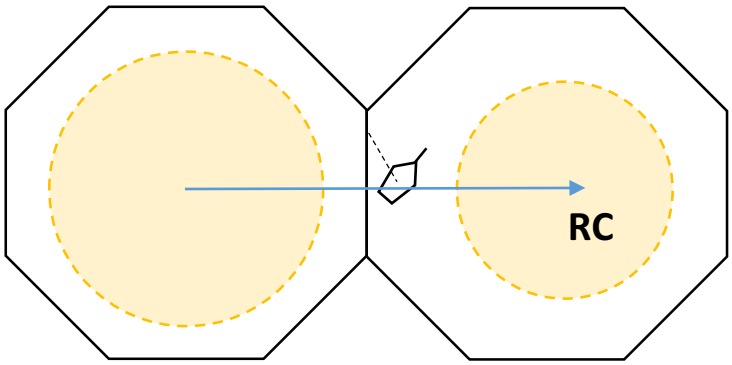

Figure C.3 Illustration of two cages in ZIF-8, between which a 2-methylimidazole (HmIM) molecule is adsorbed by the connecting window. The adsorbed HmIM causes asymmetric cages with one having larger void space than the other, as the yellow spheres show. The calculated free energy profile of an adsorbate is mapped on the 1-d reaction coordinate (RC) labeled by blue arrow.

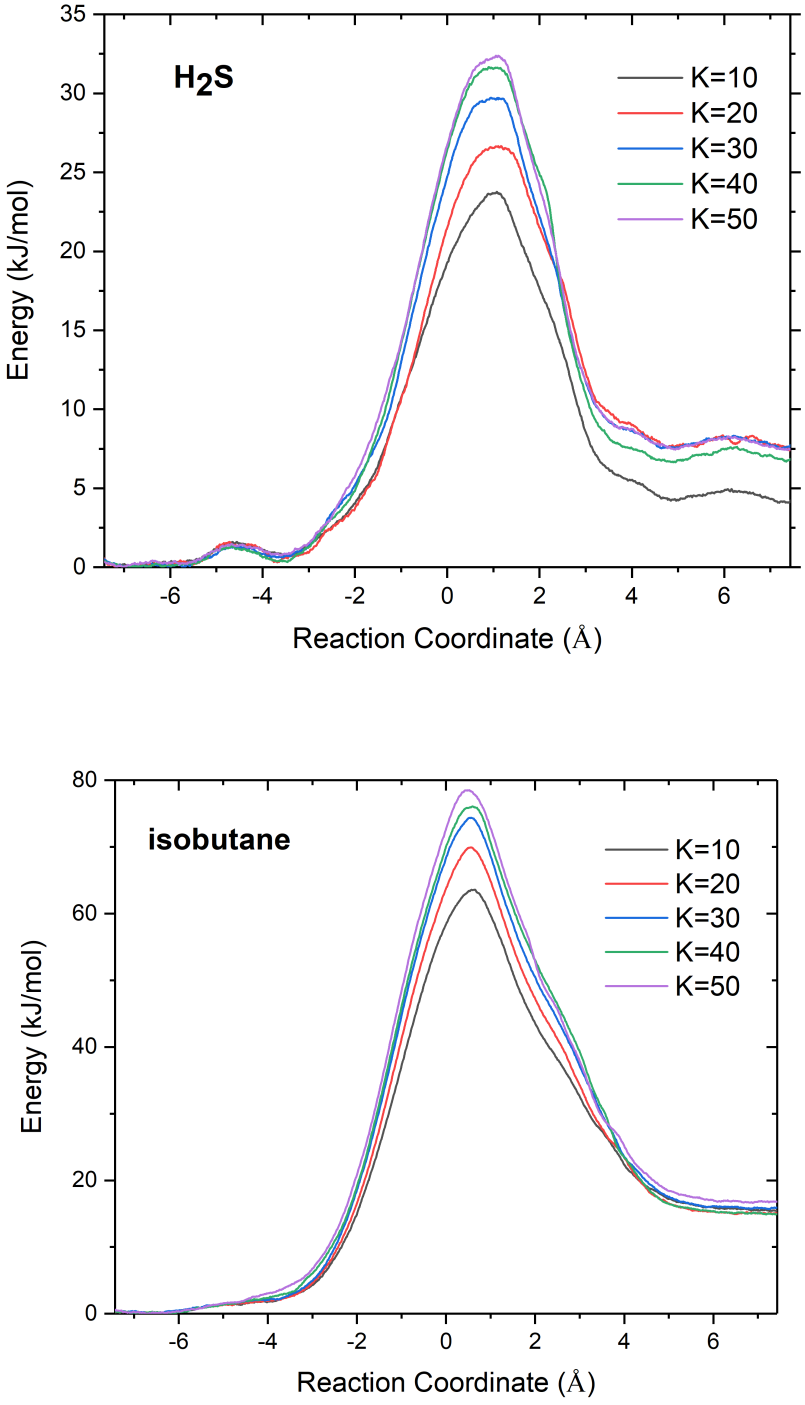

Figure C.4 Free energy profiles of H_2S and isobutane diffusing through a window having a linker vacancy that adsorbs a 2-methylimidazole molecule at 35 ^{o}C.

Table C.8 Free energy barrier (in kJ/mol) and hopping rates (in s^{-1}) for H_2S and isobutane diffusing through a window having a linker vacancy that adsorbs a 2-methylimidazole (HmIM) molecule by starting from its left (-7.43 Å in Figure C.4) and right (+7.43 Å in Figure C.4) side as a function of the spring constant K (in kcal/mol·Å^2) applied on the HmIM molecule.

K	$E_{barrier, left}$	$E_{barrier, right}$	HR_{left}	HR_{right}	TC
		H_2S			
10	23.77	19.63	8.51E+06	4.93E+07	0.6533
20	26.67	19.35	3.33E+06	7.60E+07	0.8258
30	29.72	22.24	9.75E+05	2.10E+07	0.7765
40	31.66	25.02	3.70E+05	5.81E+06	0.6427
50	32.40	24.98	3.99E+05	8.02E+06	0.8565
		iso-C_4H_{10}			
10	63.60	48.20	8.34E-01	4.56E+02	0.2809
20	69.93	55.00	8.40E-02	3.59E+01	0.3293
30	74.38	58.68	1.69E-02	9.57	0.3593
40	76.08	61.19	6.42E-03	2.67	0.2664
50	78.51	61.89	3.43E-03	2.66	0.3454

C.6 Free Energy Profiles of Water Hopping Through Two Successive Windows

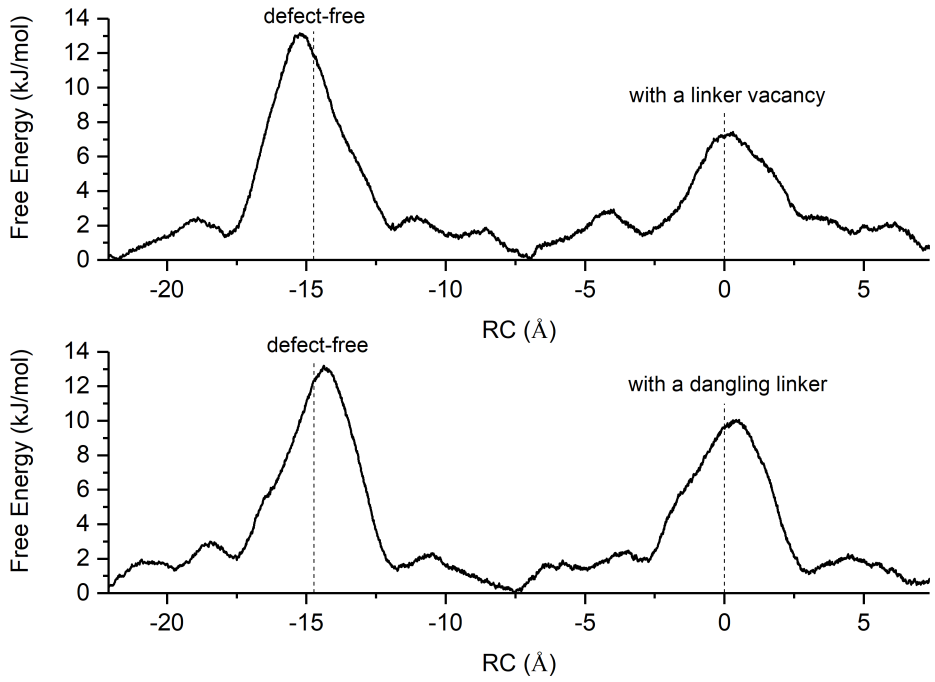

Figure C.5 Free energy profiles of water along the [111]-oriented reaction coordinate passing through a defect-free 6MR window and a defective 6MR window. The configurations of the defective windows in top and bottom panels are shown in Figures 5.1d and 5.1b, respectively. Vertical dashed lines label the positions of window centers projected on the reaction coordinate.

C.7 Density functional theory calculations

Density functional theory (DFT) calculations were performed using the Vienna Ab-initio Simulation Package (VASP) with a plane-wave basis set and the projector-augmented-wave method.[11-15] The PBE exchange-correlation functional with generalized gradient approximation and a basis set cutoff energy of 600 eV were used.[16] To include dispersion corrections, the DFT-D3 method was utilized in all calculations.[17] The Brillouin zone was sampled at the Gamma point. The energy-minimization calculations of all ZIF structures converged when the interionic forces were less than 0.03 eV/ Å.

C.8 References

(1) Zhang, L. L.; Hu, Z. Q.; Jiang, J. W., Sorption-Induced Structural Transition of Zeolitic Imidazolate Framework-8: A Hybrid Molecular Simulation Study. *J. Am. Chem. Soc.* **2013,** *135* (9), 3722-3728.

(2) Bureekaew, S.; Amirjalayer, S.; Tafipolsky, M.; Spickermann, C.; Roy, T. K.; Schmid, R., MOF-FF - A flexible first-principles derived force field for metal-organic frameworks. *Phys. Status Solidi B* **2013,** *250* (6), 1128-1141.

(3) Wu, Y. J.; Tepper, H. L.; Voth, G. A., Flexible simple point-charge water model with improved liquid-state properties. *J. Chem. Phys.* **2006,** *124* (2).

(4) Wang, J. M.; Wolf, R. M.; Caldwell, J. W.; Kollman, P. A.; Case, D. A., Development and testing of a general amber force field. *J. Comput. Chem.* **2004,** *25* (9), 1157-1174.

(5) Wang, J. M.; Wang, W.; Kollman, P. A.; Case, D. A., Automatic atom type and bond type perception in molecular mechanical calculations. *J. Mol. Graphics Modell.* **2006,** *25* (2), 247-260.

(6) Martin, M. G.; Siepmann, J. I., Transferable potentials for phase equilibria. 1. United-atom description of *n*-alkanes. *J. Phys. Chem. B* **1998,** *102* (14), 2569-2577.

(7) Harris, J. G.; Yung, K. H., Carbon Dioxides Liquid-Vapor Coexistence Curve and Critical Properties as Predicted by a Simple Molecular-Model. *J. Phys. Chem.* **1995,** *99* (31), 12021-12024.

(8) Kamath, G.; Lubna, N.; Potoff, J. J., Effect of partial charge parametrization on the fluid phase behavior of hydrogen sulfide. *J. Chem. Phys.* **2005,** *123* (12).

(9) Ketko, M. H.; Kamath, G.; Potoff, J. J., Development of an Optimized Intermolecular Potential for Sulfur Dioxide. *J. Phys. Chem. B* **2011,** *115* (17), 4949-4954.

(10) Sun, W. Z.; Lin, L. C.; Peng, X.; Smit, B., Computational screening of porous metal-organic frameworks and zeolites for the removal of SO_2 and NO_x from flue gases. *AIChE J.* **2014,** *60* (6), 2314-2323.

(11) Kresse, G.; Hafner, J., Abinitio Molecular Dynamics for Liquid Metals. *Phys. Rev. B* **1993,** *47* (1), 558-561.

(12) Kresse, G.; Hafner, J., Ab Initio Molecular-Dynamics Simulation of the Liquid-Metal-Amorphous-Semiconductor Transition in Germanium. *Phys. Rev. B* **1994,** *49* (20), 14251-14269.

(13) Kresse, G.; Furthmuller, J., Efficient iterative schemes for *ab initio* total-energy calculations using a plane-wave basis set. *Phys. Rev. B* **1996,** *54* (16), 11169-11186.

(14) Kresse, G.; Furthmuller, J., Efficiency of *ab-initio* total energy calculations for metals and semiconductors using a plane-wave basis set. *Comput. Mater. Sci.* **1996,** *6* (1), 15-50.

(15) Blöchl, P. E., Projector Augmented-Wave Method. *Phys. Rev. B* **1994,** *50* (24), 17953-17979.

(16) Perdew, J. P.; Burke, K.; Ernzerhof, M., Generalized gradient approximation made simple. *Phys. Rev. Lett.* **1996,** *77* (18), 3865-3868.

(17) Grimme, S.; Antony, J.; Ehrlich, S.; Krieg, H., A consistent and accurate ab initio parametrization of density functional dispersion correction (DFT-D) for the 94 elements H-Pu. *J. Chem. Phys.* **2010,** *132* (15), 154104.